Check for updates

Interfaces of graphitic carbon nitride-based composite photocatalysts

Anquan Zhu, [ID] Lulu Qiao, [ID] Pengfei Tan and Jun Pan [ID] *

Graphitic carbon nitride (g-C$_3$N$_4$), a layered conjugated organic polymer with suitable bandgap values of ~2.7 eV, has been a welcomed nanostructure for photocatalytic applications in energy conversion and environmental purification. Some drawbacks of the pure g-C$_3$N$_4$ restrict the enhancement of photocatalytic performances, such as the limited solar-light harvesting ability, low surface area and rapid recombination rate of photoexcited electron–hole pairs. Interface engineering is considered as an effective strategy for addressing these issues by combining the superiorities of multi-components, as well as forming various kinds of interfaces. Broadly speaking, this enables the boosting of the light-response range, accelerate the transfer and separation of charge carriers, and inhibit the recombination of photoinduced electron–hole pairs. Unlike previous reviews, we herein summarize the interfaces-related topics of g-C$_3$N$_4$-based composite photocatalysts, including the methods to controllably devise and fabricate interfaces, the techniques to identify interfaces as well as the types and functions of the as-determined interface. Also, the relevant problems and ongoing challenges to design and understand interfaces of g-C$_3$N$_4$-based composite photocatalysts are put forward and highlighted. It is anticipated that this review could open a fresh pathway to further achievements of g-C$_3$N$_4$-based photocatalysts through better understanding and exploitation of interfaces.

1. Introduction

The sharp contradiction between the ever-increasing demand for fossil fuels and their limited natural reserves, as well as-induced environmental pollution, has been a nerve-wracking problem worldwide and has been the focus of intensive attention. With the capacity for directly converting solar energy to chemical energy fuels and eliminating gas/organic pollutants without secondary pollution, semiconductor photocatalysis technology has attracted considerable scientific and industrial interest.[1–3] Through vigorous development for almost half a century, it has been applied to photocatalytic water splitting,[4–6] photocatalytic carbon dioxide reduction,[7–9] photodegradation of organic pollutants[10–12] and bacterial

State Key Laboratory for Powder Metallurgy, Central South University, Changsha 410083, P. R. China. E-mail: jun.pan@csu.edu.cn

Anquan Zhu received his B.S. degree (2015) in Powder Metallurgy and M.S. degree in Materials Science and Engineering (2018) from Central South University, China, under the supervision of Prof. Jun Pan. After working as a research assistant for about two years, he is now pursuing his Ph.D. at City University of Hong Kong. His research interests are focused on the interface engineering design of nanostructures for applications in catalysis and batteries, as well as the identification of the structure–property relationship of catalysts.

Anquan Zhu

Lulu Qiao obtained her B.S. degree (2016) in Powder Metallurgy from Central South University, China, then she received her M.S. degree in Materials Science and Engineering (2019) from the same university, under the supervision of Prof. Jun Pan. Currently, she is working as an engineer. Her research interest is focused on the electrode design of batteries.
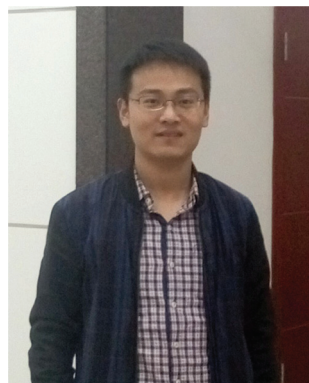
Lulu Qiao

4754 | *Inorg. Chem. Front.*, 2020, **7**, 4754–4793

This journal is © the Partner Organisations 2020

disinfection.[13,14] TiO_2 represents the pioneering attempt to implement semiconductors as photocatalysts for water splitting, which was done by Fujishima and co-workers in 1972,[15] but it is only active under ultraviolet light irradiation. Four years later, Carey *et al.*[16] employed nanoscale TiO_2 dispersed in solution to degrade mixed organic pollutants with the assistance of ultraviolet light. In 1979, Inoue *et al.*[17] synthesized a series of nanostructures including WO_3, TiO_2, ZnO, CdS, GaP, and SiC for the photocatalytic reduction of carbon dioxide. Since then, various kinds of nanostructures have been demonstrated as high-performance photocatalysts but the trouble is that most of them are only active under ultraviolet light irradiation, showing broaden bandgaps (>3 eV). Hence, it is still a challenge to devise and create novel photocatalysts with natural abundance, high activity and stability.[18]

It has been determined that the practical photocatalytic reaction involves three parts, namely, photon adsorption, the generation of electron–hole pairs, and surface catalytic reaction, which lead the way to the selection of optimal photocatalysts.[19,20] Graphitic carbon nitride is known as a metal-free layered semiconductor, possessing numerous excellent electronics, optics, thermodynamics, and physicochemical properties, which make g-C_3N_4-related nanostructures a promising class of candidates for energy and catalysis applications.[18,21,22] With a narrow bandgap of around 2.7 eV,[23] g-C_3N_4 could adsorb and make use of more energy from solar light. The broadened light-adsorption ability enables it to be promising in photocatalysis. Although g-C_3N_4 was discovered long ago, it was firstly reported by Wang *et al.*[24] for photocatalytic H_2 evolution in 2009. After that, scientific researchers turned their focus from inorganics to organics, especially for g-C_3N_4-related species. Researchers came to realize some drawbacks and shortcomings of pristine g-C_3N_4 based on experimental results, such as the low electrical conductivity and high recombination rate of photogenerated charge carriers.[1,3,25] A lot of strategies have been explored and improved upon for overcoming these disadvantages, including structural engineering,[26] surface modification,[27,28] elemental doping,[29–33] defect engineering,[34,35] interface engineering,[36–38] and so on. Based on the above-mentioned critical factors dominating photocatalytic reactions, all these methods have been established in structural and composite modifications of g-C_3N_4 to maximize the benefits of photocatalysis.

It should be noted that interface engineering has been acknowledged as a powerful strategy for constructing nanomaterials for high-performance electrochemical energy applications, such as electrocatalysis and batteries, for the sake of as-induced efficient interfacial electron transfer.[39,40] Herein, coupling g-C_3N_4 with other nanostructures to form interfaces could easily be put into practice because of its strippable layer structure and modifiable surface groups.[41] After the generation of interfaces by introducing additional phases, the advantages, including boosted visible-light adsorption ability,[9,42,43] accelerated charge carrier transfer and separation,[44–47] inhibited recombination of photoexcited electron–hole pairs,[5,48,49] and favorable stability, could be fulfilled in as-obtained g-C_3N_4-based nanocomposite photocatalysts. Over the past five years, data statistics have shown evidence that the publication numbers of g-C_3N_4 photocatalysts have progressively increased each year. Researchers have indicated that interfaces have a similar tendency, indicating that investigations of the interface of g-C_3N_4-based composite photocatalysts are meaningful, and continue to be a hot spot. For example, Shaojun Guo and co-workers[50] developed amorphous $FeCoPO_x$ nanowires-g-C_3N_4 heterostructures with Fe–N bonds, and demonstrated that the strong interfacial interactions are responsible for efficient electron transfer between the two phases, thus resulting in enhanced photocatalytic H_2 generation activity. By using a combined method of surface modification, electrostatic assembly and ion-exchange strategies, Xiaofei Yang *et al.*[51] obtained

Pengfei Tan received his B.S. degree (2014) in Powder Metallurgy and Ph.D. degree in Materials Science and Engineering (2019) from Central South University, China, under the supervision of Prof. Jun Pan. Currently, he works as a lecturer at Central South University. His research interests include the design and preparation of photocatalysts with high performance and investigation of their catalytic mechanisms.

Pengfei Tan

Jun Pan received his B.S. and M.S. degrees in Metallurgical Engineering from Central South University, China. In 2010, he successfully completed his Ph.D. degree in Inorganic Chemistry from Universität zu Köln, Germany. He worked as a research fellow at the Nanyang Technological University with Prof. Qihua Xiong for one year, then he went to Central South University and was appointed as a full professor in Materials Science and Engineering. His main research interests are the controllable synthesis of nanostructures, and their applications in the fields of environment and energy (including photocatalysis, electrocatalysis and batteries).

Jun Pan

This journal is © the Partner Organisations 2020

Inorg. Chem. Front., 2020, **7**, 4754–4793 | **4755**

the Ag_3PO_4–g-C_3N_4 heterojunction, and attributed the much-enhanced photocatalytic water oxidation performance to the interfacial interactions-induced high-efficiency photoexcited electron–hole separation and charge carrier transfer. Importantly, they highlighted the positive role of interfaces in outstanding catalytic properties in g-C_3N_4-based photocatalysts. A well-designed $W_{18}O_{49}$–g-C_3N_4 heterojunction displayed improved light-harvesting ability, collectively boosting the catalytic performance even though $W_{18}O_{49}$ is photocatalytically inert.[52] All of the above statements make us believe that interface engineering is an extremely hopeful way to produce high-performance photocatalysts and it deserves our massive investments in future research.

There are abundant reviews on the design and synthesis principles, characterization techniques, various properties, functionalization strategies, classifications, versatile applications, theoretical calculations, *etc.*, of g-C_3N_4-related photocatalysts.[2,20,25,53–62] There is no doubt that the reviews contribute a lot to g-C_3N_4-based photocatalysts for application in energy conversion and environmental repair. However, few of them have concentrated on the interfaces formed by g-C_3N_4 and other phases, even though interface engineering has proved its indelible merits to developing g-C_3N_4-based photocatalysts that can satisfy more rigorous energy and environmental issues in the future. After looking through previous reports, we found that some problems exist among the huge accomplishments (Fig. 1) that urgently need to be addressed. These problems involve the synthesis, characterization and charge carrier behaviors of g-C_3N_4-based composite catalysts with intimate interface contact. Herein, we present a comprehensive and updated review of the interfaces of g-C_3N_4-based composite photocatalysts, and we are confident that they have the potential to promote their future development. In this review, we summarize the recent progress on the synthetic strategies, characterization techniques and practical functions

of formed interfaces of g-C_3N_4-based composite photocatalysts. The ongoing challenges and key issues that we face need to be addressed for g-C_3N_4-based composite photocatalysts prepared by interface engineering and will be discussed.

2. Approaches to constructing interfaces of g-C₃N₄-based composite photocatalysts

In the current research, the construction of g-C_3N_4-based composite systems is recommended and highlighted as a practical and effective strategy for developing high-performance photocatalysts for the sake of some meritorious advantages. In general, these advantages can be summarized as altering or modifying the optical properties and electronic structures of g-C_3N_4, resulting in enhanced catalytic performance. The engineering of composite catalysts is usually accompanied by the formation of interfaces. These interfaces have been intensively investigated and it has been proposed that they are closely related to the optical properties, electronic structures and photo-generated carriers transfer states of the composite photocatalysts; *i.e.*, the interfaces play significant roles in the performances of the as-developed composite photocatalysts. However, the formation and existence of interfaces intimately depend on the original synthetic approaches. Therefore, it is necessary to classify and analyze the various preparation methods of g-C_3N_4-based composite photocatalysts. To better demonstrate the design of photocatalyst systems involved in interface engineering, we classify herein the primary preparation methods according to the environments where the interfaces are generated.

2.1. Solid-based strategies

To date, almost all the known methods for fabricate g-C_3N_4 are related to the direct thermal condensation of nitrogen-containing organic precursors (Fig. 2a) under a given solid condition, with one or mixtures of the following: melamine,[63–67] cyanamide,[68] dicyandiamide,[69–72] urea[73–76] and thiourea,[48,77,78] where the reactive temperature ranges from 450 °C to 650 °C.[41] During the thermal polymerization process, parts of the carbon and nitrogen elements are retained in the matrixes and exist as carbon nitride, while other parts are emitted in the form of ammonia, carbon oxides, hydrone, and so on. Presently the as-obtained g-C_3N_4 materials cannot be regarded as "ideal" two-dimensional graphitic network structures, even though they generally display commendable performances in photocatalytic applications. These kinds of "flawed" g-C_3N_4 nanomaterials have low crystallinity and various surface physicochemical structures and components.[55,79] Accordingly, they are much easier to modify and they enhance catalytic properties by forming interface contacts with other types of photocatalysts. In view of the original solid-state synthetic route of pure g-C_3N_4, solid-based strategies including mechanical mixing/grinding/ball-milling and calcination (Fig. 2b) are

Fig. 1 Annual number of publications observed on searching the themes "g-C₃N₄ photocatalyst" and "g-C₃N₄ photocatalyst + interfaces" over the past five years. (Data from Web of Science, date of search: August 10th, 2020.)

4756 | *Inorg. Chem. Front.*, 2020, **7**, 4754–4793

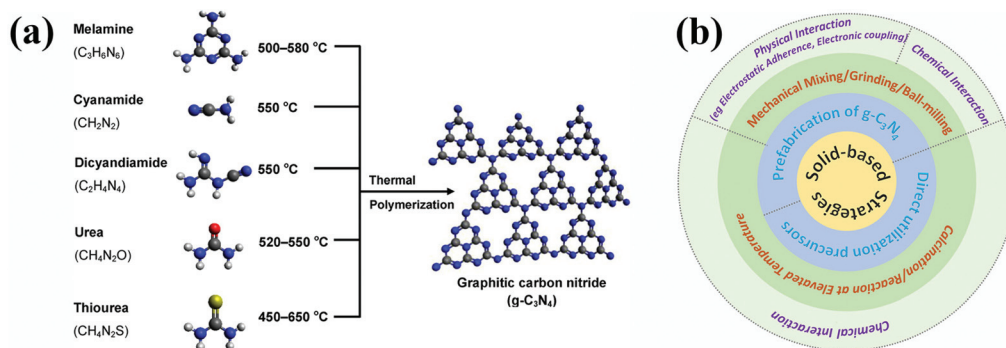This journal is © the Partner Organisations 2020

Fig. 2 (a) Graphical illustration of the general preparation conditions for g-C$_3$N$_4$ from various organic precursors, where the blue, grey, white, red and yellow balls represent N, C, H, O, S atoms, respectively. Reproduced from ref. 41 with permission from the American Chemical Society, Copyright 2016. (b) Synthetic strategies for g-C$_3$N$_4$ composite photocatalysts with interface contacts based on solid-state conditions.

reasonably suggested as feasible and effective methods for creating g-C$_3$N$_4$ composites with interface contacts.

2.1.1. Mechanical mixing/grinding/ball-milling. Mechanical mixing/grinding/ball-milling have been demonstrated as ecological and economical methods for developing novel materials in a variety of fields such as organic chemistry, supramolecular chemistry, organometallics, polymers, inorganic chemistry and nanoparticles.[81] These technologies are not only economical and simple to handle, but they are also capable of uniformly dispersing nanoparticles into organic matrixes, where the physical/chemical interactions (including electrostatic adherence, electronic coupling and chemical bonding) can be generated in the composite systems.[82] Therefore, they have been commonly employed in the synthesis of heterostructured g-C$_3$N$_4$-based composite photocatalysts. Recently, a facile self-assembly strategy involving the physical mixing of phosphorene and g-C$_3$N$_4$ (denoted as P–g-CN) in an ethanol solution was successfully used to engineer a new-style, metal-free two-dimensional/two-dimensional phosphorene/g-C$_3$N$_4$ van der Waals heterojunction.[80] In Fig. 3a, the TEM image of the P–g-CN heterojunction reveals that the two-dimensional sheet-like g-C$_3$N$_4$ is stuck on the top surface of phosphorene. Combined with the corresponding X-ray photoelectron spectroscopy (XPS), X-ray absorption near edge structure (XANES) analysis, and density functional theory (DFT) cal-

culations, the net electron accumulation and depletion states around the interfaces of phosphorene and g-C$_3$N$_4$ (Fig. 3b) demonstrate that the interface electronic coupling between the van der Waals forces connecting the two phases is responsible for the excellent photocatalytic H$_2$ evolution performance. In addition to phosphorene,[80] black phosphorus,[83] fullerene[84] and metal–organic frames (MOFs),[85] some inorganic nanostructures containing bismuth-based compounds,[66,86–89] metal oxides,[90–94] metal phosphides,[47,95] metal carbides,[96] and chromium-doped SrTiO$_3$ [97] were also introduced for the construction of g-C$_3$N$_4$-based composite photocatalysts by mechanical mixing methods.

Nearly all of the as-developed g-C$_3$N$_4$-based composite photocatalysts exhibited enhanced catalytic activity as compared to pure g-C$_3$N$_4$. More significantly, these strategies are highly promising because they can easily be put into practice on a commercial scale, which is beneficial for dealing with the ever-increasing global energy and environmental issues. However, the problem is that the interfaces produced by these mechanical methods are usually in a state of low interacting forces and are relatively vulnerable; as a result, they show inferior durability in photocatalytic stability tests. As shown in Fig. 4, various g-C$_3$N$_4$-based composite photocatalysts that are obtained from mechanical methods, unfortunately, show an obvious activity loss (generally more than 20% after four cycles). The authors suggest that this phenomenon arises from the gradual fall-off of the second modifying component from g-C$_3$N$_4$, which further triggers the recession of photocatalytic activity.[47,93,95,96] Based on these facts, we have reasons to believe that the interface contacts with simple physical interactions among multi-phases of g-C$_3$N$_4$-based composites, just like most of the cases, may not meet the requirement of long-time operation, even if they play vital roles in improving the catalytic activity of composite photocatalysts. As such, simple mechanical methods have their advantages in creating interface linking over g-C$_3$N$_4$-based composite catalysts. The current urgent issue that needs to be solved is finding a way to strengthen the interactions at the interfaces to ensure acceptable durability in long-term photocatalytic applications.
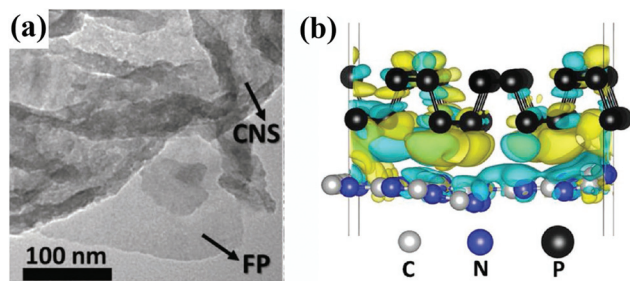

Fig. 3 (a) TEM image of the as-fabricated P–g-CN heterojunction. (b) Side-view differential charge density map of phosphorene and g-C$_3$N$_4$. Reproduced from ref. 80 with permission from Wiley-VCH, Copyright 2018.

This journal is © the Partner Organisations 2020

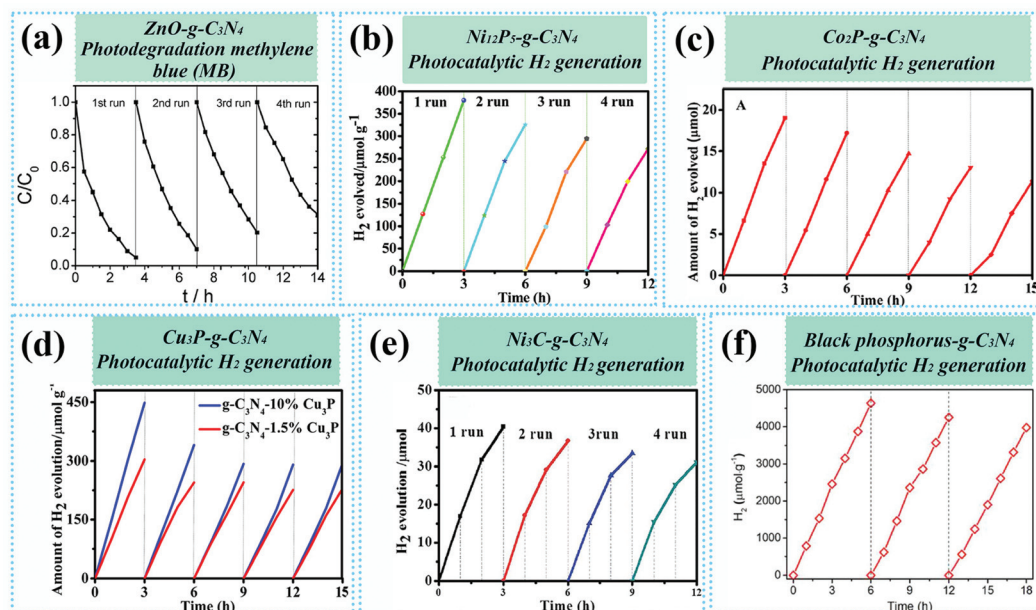*Inorg. Chem. Front.*, 2020, **7**, 4754–4793 | **4757**

Fig. 4 (a) Stability measurements of the photodegradation of MB by the ZnO−g-C₃N₄ composite catalyst. Reproduced from ref. 90 with permission from the Royal Society of Chemistry, Copyright 2014. Cycling stability tests of photocatalytic H₂ generation over Ni₁₂P₅−g-C₃N₄ (b),[93] Co₂P−g-C₃N₄ (c),[47] Cu₃P−g-C₃N₄ (d),[95] Ni₃C−g-C₃N₄ (e),[96] and P−g-C₃N₄ (f)[83] composite catalysts. Reproduced from ref. 93 with permission from the Royal Society of Chemistry, Copyright 2017; reproduced from ref. 47 and 95 with permission from the American Chemical Society, Copyright 2017 and 2018, respectively; reproduced from ref. 96 with permission from the Royal Society of Chemistry, Copyright 2018; reproduced from ref. 83 with permission from Wiley-VCH, Copyright 2019.

2.1.2. Calcination/reaction at elevated temperatures. Unlike mechanical energy to drive interface formation, heat treatment/calcination methods are sufficient to supply energy to produce and strengthen interfacial bonding. Moreover, diverse types of interfaces with various nanostructures could be generated by controlling the reactive conditions, such as the reaction temperature, the heating rate, the calcination preservation period, the reactive atmosphere, and so on. For example, oxygen-containing inorganic compound–g-C₃N₄ composites are commonly processed in air, which could easily be prepared by mixing precursors/g-C₃N₄ with other reagents used for preparing a second phase combined with a heat-treatment process. In particular, Quan Gu *et al.*[98] successfully developed a NiO-modified g-C₃N₄ composite (NiO–g-C₃N₄) by annealing a prefabricated Ni(OH)₂-decorated g-C₃N₄ intermediate hybrid at a series of reaction temperature settings (from 100 °C to 500 °C, at 100 °C intervals, Fig. 5a) for three hours in air, where amorphous or crystalline NiO attached to g-C₃N₄ could be controlled by the temperature settings above or below 300 °C. In contrast, phosphide–g-C₃N₄, carbon-based species–g-C₃N₄ and sulfide–g-C₃N₄ composites tend to be produced in a N₂/argon/vacuum atmosphere. A universal strategy for obtaining transition metal phosphide (TMP)–g-C₃N₄ composite photocatalysts was highlighted by Genqiang Zhang's group.[75] Prior to calcination under the conditions of 300 °C, 2 h (heating rate of 2 °C min⁻¹) and Ar gas, the precursor materials related to the metal-glycolate-coated g-C₃N₄ are prepared in a liquid environment, then the TMP–g-C₃N₄ compo-

sites are obtained. In Fig. 5c, to synthesize interconnected carbon nanofibers–g-C₃N₄-composite,[99] the freeze-dried hydro-thermally-treated dicyandiamide (HTD) blended with pyrrole was subjected to heating at 600 °C for 4 h (heating rate of 1 °C min⁻¹) in Ar flow. MoS₂ is known for its two-dimensional layer structure and extensive applications in physics, chemistry, energy and environmental science. A characteristic MoS₂–g-C₃N₄ van der Waals layer heterojunction[70] was formed by annealing the mixture of dicyandiamide, molybdate and sulfate at 550 °C for 2 h, saturated with Ar atmosphere (heating rate of 2 °C min⁻¹). Metal carbides are relatively stub-born and generally require high-temperature conditions to oxidize, even when exposed in air. As a consequence, metal carbide–g-C₃N₄ composite photocatalysts can be harvested in either air or protective atmospheres (N₂, Ar and vacuum). Taking the Ti₃C₂–g-C₃N₄ composite catalyst as an example, X-ray photoelectron spectroscopy (XPS) revealed that the as-obtained Ti₃C₂–g-C₃N₄–N₂ and Ti₃C₂–g-C₃N₄–air samples possess similar elemental components and relative concentrations.[100] That means that both N₂ and air atmospheres are suitable for the fabrication of metal carbide–g-C₃N₄ composites at relatively low reaction temperatures.

In a real fabrication process, more beneficial possibilities related to interfaces could be offered by involving solid–liquid–gas phase reactions triggered by heat treatment. Generally speaking, there are two routes for synthesizing g-C₃N₄ composite photocatalysts with interface contacts, which could be illustrated as precursor-oriented and g-C₃N₄-oriented methods,
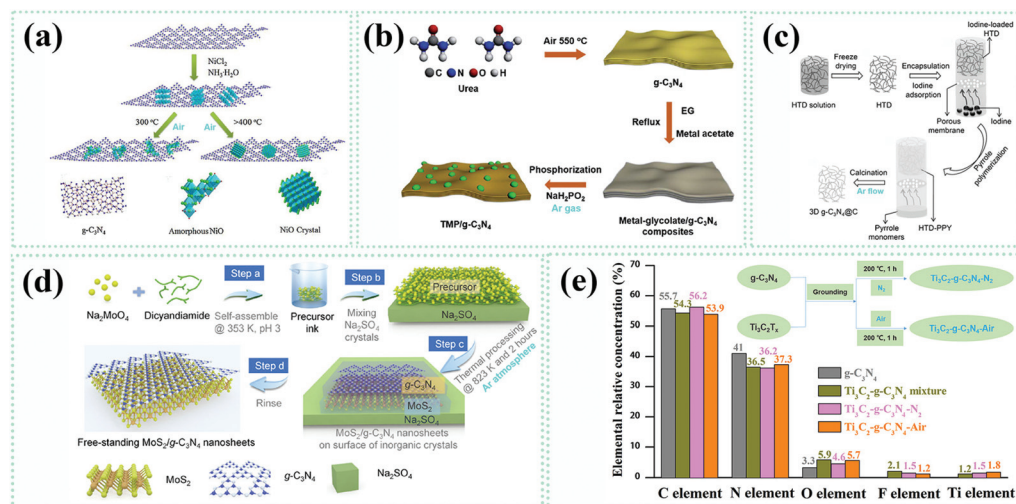
Fig. 5 (a) Illustration of NiO−g-C$_3$N$_4$ composite catalyst synthesis. Reproduced from ref. 98 with permission from Elsevier, Copyright 2018. (b) Synthetic route to transition metal phosphide (TMP)−g-C$_3$N$_4$ composite catalysts. Reproduced from ref. 75 with permission from the Royal Society of Chemistry, Copyright 2019. (c) The fabrication method for carbon nanofibers−g-C$_3$N$_4$. Reproduced from ref. 99 with permission from Wiley-VCH, Copyright 2016. (d) Schematic illustration of the fabrication of MoS$_2$−g-C$_3$N$_4$ heterojunction catalysts. Reproduced from ref. 70 with permission from Elsevier, Copyright 2016. (e) Relative elemental concentrations of C, N, O, F and Ti in g-C$_3$N$_4$, the g-C$_3$N$_4$ and Ti$_3$C$_2$ mixture, Ti$_3$C$_2$−g-C$_3$N$_4$−N$_2$ and Ti$_3$C$_2$−g-C$_3$N$_4$−N$_2$ samples; the inset shows the corresponding synthetic routes of two Ti$_3$C$_2$−g-C$_3$N$_4$ samples.[100]

respectively. Herein, the precursor-oriented method means directly using the precursors to synthesize g-C$_3$N$_4$ to fabricate g-C$_3$N$_4$-based composites, while the g-C$_3$N$_4$-oriented method signifies that the g-C$_3$N$_4$-based composites are obtained from prefabricated g-C$_3$N$_4$ instead of its precursors. Table 1 summarizes typical g-C$_3$N$_4$-based composite photocatalysts based on the two methods mentioned above in synthetic processes. From these incomplete data, it is hard and unconvincing to point out the precise proportions for preparation methods, which are based on heat treatments, employed to synthesize g-C$_3$N$_4$-based composite photocatalysts. Nevertheless, we do find that the strategy involving the liquid-phase mixing of reactants is dominant for both the precursor-oriented and g-C$_3$N$_4$-oriented methods. This might result from a better and more homogeneous contact among various reactants achieved in liquid, far surpassing blending them in the solid-state.

2.2. Liquid-based methods

To more rationally exploit and design liquid-based methods to prepare g-C$_3$N$_4$-based composite photocatalysts, the facts concerning the physicochemical properties of g-C$_3$N$_4$ have to be figured out in advance. Similar to graphene, g-C$_3$N$_4$ also has a typical stacked two-dimensional layer structure (Fig. 6a). It has been demonstrated that g-C$_3$N$_4$ possesses two kinds of condensation states, s-triazine units (Fig. 6b) and tri-s-triazine/heptazine subunits (Fig. 6c, the tri-ring of C$_6$N$_7$).[21] The latter form of g-C$_3$N$_4$ is interconnected with planar tertiary amino groups, therefore giving rise to more periodic vacancies throughout the lattice. The detailed lattice constants and crystal structures were experimentally probed by the XRD technique. In the measured XRD pattern (Fig. 6d),[20,24] the peak located at 13.0° was assigned to the (100) lattice plane, which reflects a dis-

tance of 0.681 nm for the in-plane structural packing motif caused by two-dimensional layer structure blending. The peak at 27.4° was indexed to the (002) plane, indicating a two-dimensional sheet-like structure with a layer stacked distance of 0.326 nm. Incomplete polycondensation would reserve a small fraction of hydrogen and nitrogen atoms participating in surface functionalities, including of surface defects, basic surface functional groups, electron-rich properties and H-bonding motifs (Fig. 6e).[21] These surface functional groups of g-C$_3$N$_4$ (such as –NH$_2$, –NH–, =N– and C–N groups) are facile for capturing metallic ions and organic molecules through electrostatic interactions and chemical adsorption, which means that the surface of g-C$_3$N$_4$ can be modified by introducing oxygen-containing functional groups and form chemical bonds with other atoms, thus providing a favorable dispersion in aqueous solution.[112] Commonly reported in previous work, the functional chemical groups and bonding, such as –C$_6$N$_7$, C=N–C, N–(C)$_3$, N=C–N$_2$, C–NH–C, N–H bonding, have been proved by Fourier transform infrared (FT-IR) spectroscopy and X-ray photoelectron spectroscopy (XPS) measurements.

Many surface functional groups contribute to the varied possibilities of superficial charge of g-C$_3$N$_4$ when dispersed in different solutions with different pH values. The surface charges of g-C$_3$N$_4$ could be detected by the isoelectric point (IEP) and the zeta potential techniques. In the experimental test, the zeta potential values (Fig. 7) of g-C$_3$N$_4$ dispersed solution with diverse pH values showed a big difference.[113] The IPEs of g-C$_3$N$_4$ derived from urea (UCN), melamine (MCN) and thiourea (TCN) were investigated to be 5.1, 5.0 and 4.4, respectively. Consequently, the dispersed solutions (pH = 7) with UCN, MCN and TCN display the zeta potential values of

This journal is © the Partner Organisations 2020

Inorg. Chem. Front., 2020, **7**, 4754–4793 | **4759**

Table 1 Some previous reports on synthesizing g-C$_3$N$_4$–based composite photocatalysts by using the calcination method

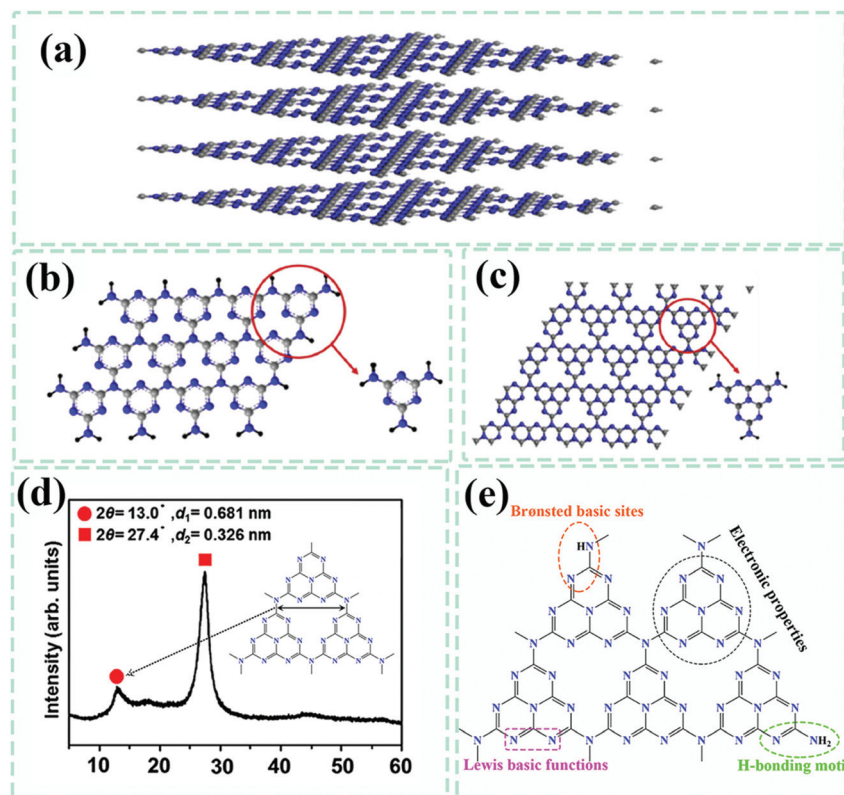| Synthetic methods	Composites	Pretreatments of reactant	Reaction conditions	Ref.
Precursor-oriented	Solid-phase mixing			
	WO$_3$–Bi$_2$O$_3$–g-C$_3$N$_4$	Grinding the mixture of melamine, W-source and Bi-source	520 °C–2 h + 540 °C–2 h	65
	C-doped TiO$_2$–g-C$_3$N$_4$	Grinding the mixture of urea and TiC	10 °C min^{-1}, 500 °C–2 h, air	101
	NaNbO$_3$–g-C$_3$N$_4$	Grinding the mixture of melamine and NaNbO$_3$	20 °C min^{-1}, 520 °C–4 h, air	102
	Sr$_2$Ta$_2$O$_7$–g-C$_3$N$_4$	Grinding the mixture of thiourea and Sr$_2$Ta$_2$O$_7$	5 °C min^{-1}, 400 °C–1 h, air	78
	Ti$_3$C$_2$–g-C$_3$N$_4$	Grinding the mixture of thiourea and Ti$_3$C$_2$	500 °C–2 h, air	48
	Liquid-phase mixing			
	WO$_3$–g-C$_3$N$_4$	Melamine and WO$_3$ dispersed to ethanol, stirring, drying	550 °C–2 h, air	103
	CoO–g-C$_3$N$_4$	Melamine and Co-source dissolved into deionized water, stirring, drying	4 °C min^{-1}, 500 °C–3 h, N$_2$	104
	Fe$_2$O$_3$–g-C$_3$N$_4$	Melamine and Fe$_2$O$_3$ dispersed deionized water, stirring, drying	2 °C min^{-1}, 550 °C–4 h, air	105
	MoS$_2$–g-C$_3$N$_4$	Mixing dicyandiamide and Mo-sources in acid solution, self-assembling, then adding the S-source, grinding, drying	2 °C min^{-1}, 550 °C–2 h, Ar	70
	Ti$_2$C–g-C$_3$N$_4$	Adding melamine and Ti$_2$C into ethanol, stirring, drying	5 °C min^{-1}, 550 °C–4 h	106
	Carbon dots–g-C$_3$N$_4$	Adding urea and carbon dots into water, keeping in liquid nitrogen, drying	5 °C min^{-1}, 550 °C–3 h	107
	Carbon fibers–g-C$_3$N$_4$	Mixing hydrothermally treated dicyandiamide with pyrrole	1 °C min^{-1}, 600 °C–4 h, Ar	99
	Gas-phase mixing			
	TiO$_2$–g-C$_3$N$_4$	Depositing melamine onto TiO$_2$ arrays through a chemical vapor deposition process	5 °C min^{-1}, 550 °C–4 h, air	108
g-C$_3$N$_4$-oriented	Solid-phase mixing			
	SrTiO$_3$–g-C$_3$N$_4$	Mixing g-C$_3$N$_4$ and SrTiO$_3$ powder, and grinding	520 °C–2 h, air	38
	Ni$_2$P–g-C$_3$N$_4$	Mixing Ni(OH)$_2$@g-C$_3$N$_4$ with P-source and grinding	2 °C min^{-1}, 300 °C–2 h, Ar	44
	Ni$_2$P–g-C$_3$N$_4$	Grinding the mixture of g-C$_3$N$_4$, Ni-source and P-source	2 °C min^{-1}, 400 °C–2 h, Ar	49
	Ti$_3$C$_2$T$_x$–g-C$_3$N$_4$	Mixing g-C$_3$N$_4$ and Ti$_3$C$_2$T$_x$ powder	200 °C–1 h, N$_2$	100
	Liquid-phase mixing			
	TiO$_2$–g-C$_3$N$_4$	Mixing g-C$_3$N$_4$ and TBTO in ethanol, stirring, adding water to hydrolyze, drying	15 °C min^{-1}, 300 °C–4 h, N$_2$	109
	SnO$_2$–g-C$_3$N$_4$	Mixing g-C$_3$N$_4$ with SnO$_2$ in water and ethanol, stirring and drying	2 °C min^{-1}, 500 °C–2 h	72
	CeO$_2$–g-C$_3$N$_4$	Heating the mixture of g-C$_3$N$_4$ ramification, L-cysteine, PVP and Ce-source, stirring and refluxing, washing and drying	5 °C min^{-1}, 550 °C–2 h, N$_2$	68
	Co$_3$O$_4$–g-C$_3$N$_4$	Ultrasonically mixing and stirring g-C$_3$N$_4$, CoCl$_2$·6H$_2$O and NH$_4$HCO$_3$, washing and drying	300 °C–2 h, air	74
	CdS–MoS$_2$–g-C$_3$N$_4$	Mixing g-C$_3$N$_4$, MoS$_2$ powder, Cd-source and S-source, reacting, washing and drying	150 °C–2 h, N$_2$	110
	CoP–g-C$_3$N$_4$	G-C$_3$N$_4$ and Co-source added in ethylene glycol, ultrasonication, stirring, heating, refluxing, washing	2 °C min^{-1}, 300 °C–2 h, Ar	75
	MoP–g-C$_3$N$_4$	The mixture of g-C$_3$N$_4$ and MoP sonicated and stirred, then drying	350 °C–2 h, Ar	111

Fig. 6 (a) Illustrations of the two-dimensional layer structure of g-C_3N_4, (b) s-triazine, and (c) tri-s-triazine as the main building blocks of g-C_3N_4. Reproduced from ref. 21 with permission from Elsevier, Copyright 2017. (d) XRD pattern of g-C_3N_4. Reproduced from ref. 24 with permission from Nature Publishing Group, Copyright 2009. (e) Multiple surface physicochemical properties of g-C_3N_4.[25]
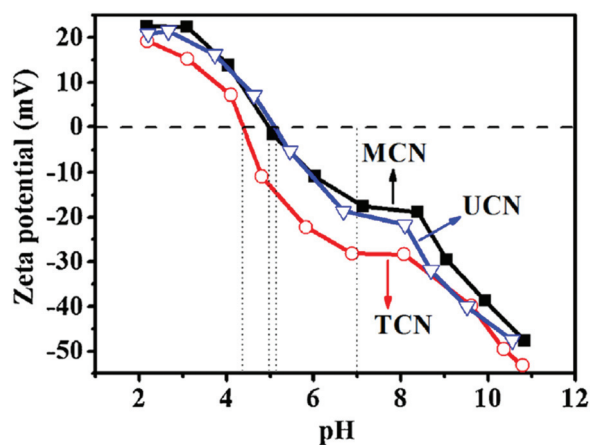

Fig. 7 Measured zeta potential values of g-C_3N_4 suspensions prepared from urea (UCN), melamine (MCN) and thiourea (TCN) with varied pH values. Reproduced from ref. 113 with permission from Elsevier, Copyright 2015.

−30.7 mV, −17.0 mV and −19.9 mV. The researchers could effectively control the surface charges by simply regulating the pH values of g-C_3N_4 dispersion, which lays a solid foundation for exactly constructing g-C_3N_4-based composite photocatalysts with interface contacts in liquid.

2.2.1. Liquid-phase reduction/co-precipitation/self-assembly. Distinguished from solid-based strategies, g-C_3N_4-based composite photocatalysts prepared by liquid-based methods use prefabricated g-C_3N_4 firsthand. To date, generally, nanostructures coupled with g-C_3N_4 in liquid can be divided into roughly three categories, namely, nonmetals, noble metals, other metals and metallic-based compounds. Recently, integrating black phosphorus species (BP) with g-C_3N_4 in liquid has been a hot research focus due to the significantly upgraded performances of the as-developed BP–g-C_3N_4 composites for photocatalytic H_2 evolution and molecular oxygen activation.[114–117] For these BP–g-C_3N_4 composites, the authors propose and demonstrate that the interactions between BP and g-C_3N_4 are P–N/P–C bonds or van der Waals forces,[118–121] which could be formed in the liquid synthesis process. Dongling Ma *et al.*[119] successfully developed a two-dimensional-two-dimensional (2D–2D) BP nanosheets–g-C_3N_4 nanosheet hybrid photocatalyst by mixing the two components in isopropyl alcohol under the protection of N_2 gas. Such 2D–2D allocation linked to P–N bonds enabled the largest interfacial contact between BP and g-C_3N_4 sheets along with the highly efficient and stable photocatalytic activity induced by effective charge transfer and separation through the chemical bonds. Moreover, Shengzhong Liu *et al.*[121] adopted a liquid-phase high-vacuum stirring method to load BP quantum dots

This journal is © the Partner Organisations 2020

Inorg. Chem. Front., 2020, **7**, 4754–4793 | **4761**

(BPQDs) onto g-C_3N_4 nanosheets for photocatalytic H_2 generation. They confirmed that the van der Waals forces exist at the interfaces of BPQDs and g-C_3N_4, which are responsible for the accelerated photo-induced carrier migration, further leading to enhanced catalytic performances.

According to the above-mentioned fact, the surface of g-C_3N_4 is negatively charged in its suspension with a pH value greater than that of IEPs. Noble metallic cations are capable of being attached to g-C_3N_4 through chemical adsorption. Thus, some noble metal-based species–g-C_3N_4 composites have been constructed *via in situ* chemical reduction,[122–125] photo-induced reduction[126,127] and co-precipitation strategies.[128–131] Lacking the required conditions in thermodynamics and kinetics, these noble metallic-based species generated from liquid reduction/co-precipitation methods are inclined to randomly exist as nanoparticle-like, with sizes ranging from several nanometers to dozens of nanometers. In a typical synthesis route (Fig. 8),[132] the first step is dispersing the as-prepared g-C_3N_4 in deionized water/organic solution, followed by chemically adsorbing noble metallic cations onto the surface of g-C_3N_4. Finally, chemical reduction reagents, reducing light sources, or co-precipitated anions are applied to the reaction mixture, bringing about the targeted noble metals–g-C_3N_4 composite photocatalysts.

A photo-induced reduction strategy was also applied to load transition metallic Co and Ni onto g-C_3N_4 through Co–N_x and Ni–N_x bonds, making for much improved photocatalytic H_2 evolution properties.[138,139] As for sulfides–g-C_3N_4 composites, carbides–g-C_3N_4 composites, phosphides–g-C_3N_4 composites and some non-precious metals and their oxides–g-C_3N_4 composites, they are commonly fabricated by a liquid self-assembly process from pre-prepared non-precious metallic compounds and g-C_3N_4, as shown in Fig. 9a and b. In this way, the interface interactions of these g-C_3N_4-based composites are relatively weak. On the other hand, *in situ* liquid-phase co-precipitation and liquid-phase self-assembly methods are preferred for synthesizing hydroxide–g-C_3N_4 composites (Fig. 9c), bismuth salts–g-C_3N_4 composites (Fig. 9d), and metal–organic

frames–g-C_3N_4 composites (Fig. 9e). Benefiting from the adjustable surface charges and chemical groups of g-C_3N_4 suspensions with different pH values in liquid, the interface engineering of g-C_3N_4-based composite photocatalysts could be efficiently implemented.

Sonication-assisted techniques (SAT) have been frequently applied for the liquid exfoliation of two-dimensional layer materials because they release numerous high-frequency vibrations as well as a huge amount of energy over the liquid system. Continuous sonication can destroy the van der Waals forces of interlayer stacking, resulting in a more uniform stepped-up dissolution or dispersion rate and guaranteeing a substantive contact among multiple components of reactants in comparison to simple electromagnetic stirring. SAT has been used to obtain single-/few-layer g-C_3N_4 nanosheets in liquid. As early as 2013, Pulickel M. Ajayan *et al.*[140] applied sonication treatment to the mixture of g-C_3N_4 bulk, isopropyl alcohol, *n*-methyl pyrrolidone, water, ethanol, or acetone for 10 h (Fig. 10a), eventually obtaining light-yellow exfoliated g-C_3N_4 nanosheets with a uniform thickness of about 2 nm. Objectively speaking, it is not amazing to find the utilization of SAT in most reports associated with manufacturing g-C_3N_4-based composites in liquid phases. Taking the metal sulfide–g-C_3N_4 composite shown in Fig. 10b as an example,[141] the CdS/Cu_7S_4 nanocomposite was fabricated in advance during an ion-exchange process between CdS and Cu^{2+}. It was then added to a dispersion made up of g-C_3N_4 and methanol, with ultrasound treatment for 24 h and the targeted CdS/Cu_7S_4/g-C_3N_4 composite photocatalyst was acquired. Protonated by HCl solution, a transformation of the g-C_3N_4 surface from negatively charged (−15.4 mV) to positive charged (14.0 mV) was accomplished.[142] In the meantime, ultrasonically delaminated graphene oxide (GO) nanosheets were found to be negatively charged with a zeta potential of −43.6 mV. Positively-charged g-C_3N_4 and negatively-charged GO realized spontaneous self-assembly in liquid through electrostatic adherence and π–π stacking interactions with the assistance of sonication. Recently, $CsPbBr_3$ perovskite quantum dots (QDs) inter-
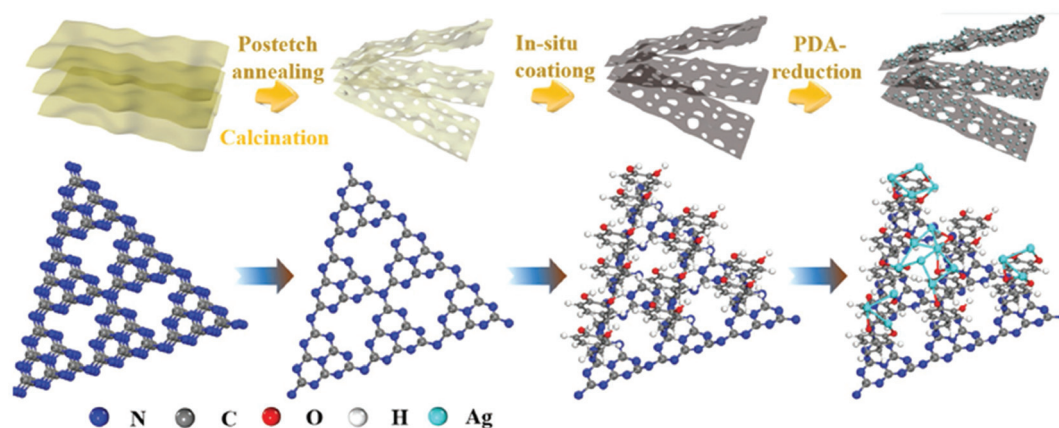

Fig. 8 Typical illustration of the synthesis of noble metals–g-C_3N_4 composite photocatalysts. Reproduced from ref. 132 with permission from Wiley-VCH, Copyright 2019.
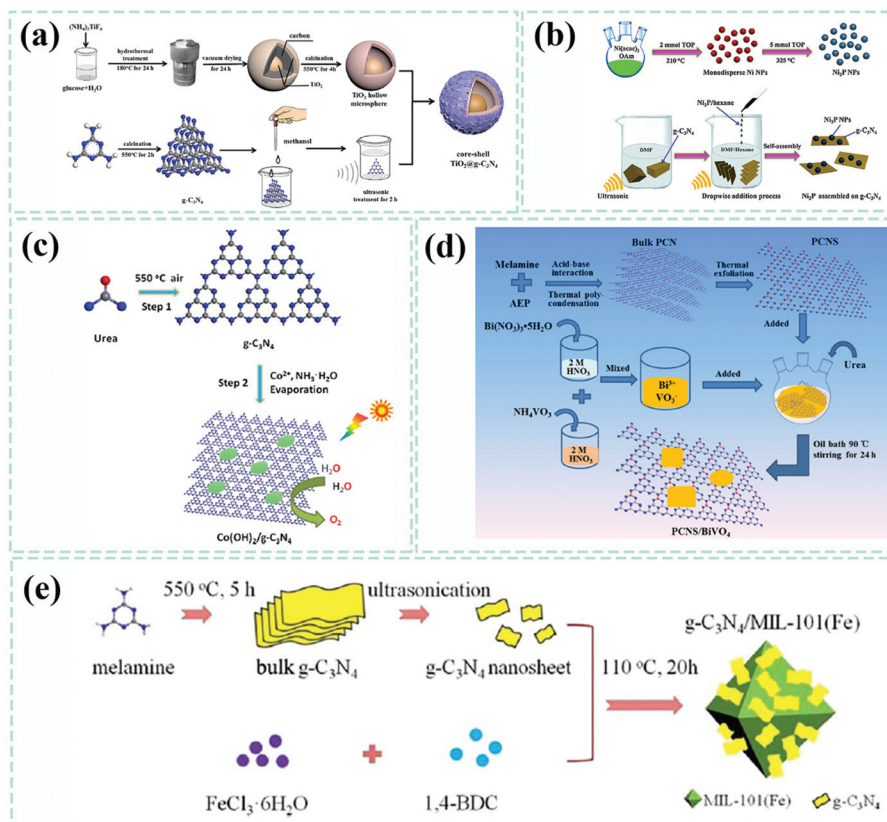
4762 | *Inorg. Chem. Front.*, 2020, **7**, 4754–4793

This journal is © the Partner Organisations 2020

Fig. 9 Typical illustration of the preparation of non-precious metals and their oxides–g-C$_3$N$_4$ composite (a) and phosphides–g-C$_3$N$_4$ composite (b) photocatalysts. (a) and (b) were reproduced from ref. 133 and 134 with permission from Elsevier, Copyright 2018. (c) A typical process for obtaining hydroxide–g-C$_3$N$_4$ composites. Reproduced from ref. 135 with permission from the American Chemical Society, Copyright 2015. (d) A representative synthesis diagram of bismuth salts–g-C$_3$N$_4$ composites. Reproduced from ref. 136 with permission from Elsevier, Copyright 2018. (e) Schematic illustration of the fabrication of MIL-101(Fe)–g-C$_3$N$_4$ composites. Reproduced from ref. 137 with permission from the Royal Society of Chemistry, Copyright 2018.
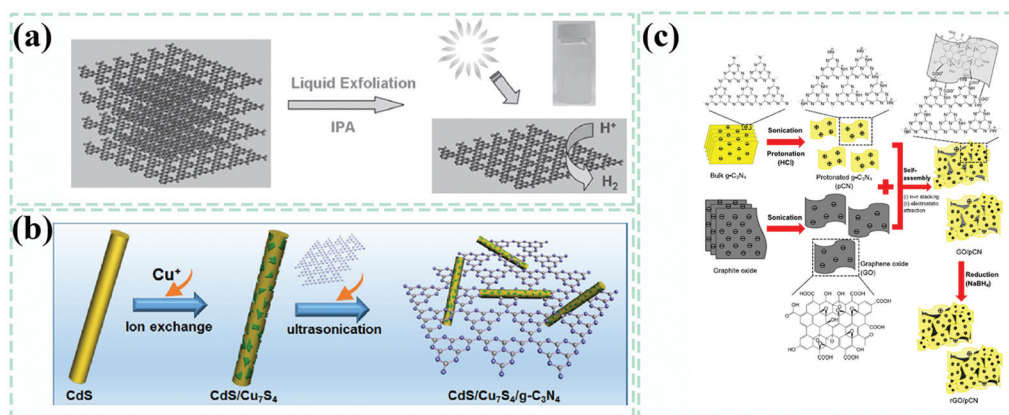

Fig. 10 (a) Graphical illustration of the synthesis of g-C$_3$N$_4$ nanosheets from bulk g-C$_3$N$_4$ in liquid. Reproduced from ref. 140 with permission from Wiley-VCH, Copyright 2013. (b) Illustration of the synthesis of the CdS/Cu$_7$S$_4$/g-C$_3$N$_4$ composite photocatalyst. Reproduced from ref. 141 with permission from the American Chemical Society, Copyright 2018. (c) Graphical diagram of the synthesis of the reduced graphene oxide (RGO)/g-C$_3$N$_4$ composite photocatalyst. Reproduced from ref. 142 with permission from Elsevier, Copyright 2018.

linked to g-C$_3$N$_4$ with N–Br chemical bonds were engineered by ultrasonication treatment and stirring of the mixture from CsPbBr$_3$ QDs and g-C$_3$N$_4$ powder in hexane.[143] The fact that the surface of g-C$_3$N$_4$ is rich in NH$_x$ groups makes it highly possible to form stable chemical bonds between CsPbBr$_3$ QDs and g-C$_3$N$_4$.

This journal is © the Partner Organisations 2020

Inorg. Chem. Front., 2020, **7**, 4754–4793 | **4763**

2.2.2. Hydro/solvothermal synthesis. Imitating the high temperature and pressure conditions of natural mineral formation, the hydro/solvothermal method has been developed into one of the most effective and practical experimental techniques for controllably synthesizing multi-dimensional nanostructures with well-developed regular structures and exposed lattice planes. It simultaneously tailors the contacting interface types among multiple components of prepared nanocomposites. Analogous to liquid-phase reduction/co-precipitation/self-assembly, the reactants, depicted in Table 2, are subjected to stirring, ultrasonic treatment, or both before proceeding to reactions to build interfaces, to homogeneously disperse g-C_3N_4 and other reactants and achieve subsequent reactions.

To maximize the availability of surface area for g-C_3N_4, bulk g-C_3N_4 is exfoliated into g-C_3N_4 nanosheets for further use. In liquid, the ions and groups can be easily attached to the surfaces of g-C_3N_4 through chemical adsorption and the electrostatic adherence effect. Protonation of the original g-C_3N_4 causes a transformation of the surface charges from negative to positive, thus making it possible to couple with a nanostructure dominated by negative surface charges instead of just positive surface charges.[159] Whether for facile liquid reduction/co-precipitation/self-assembly or hydro/solvothermal synthesis, the ions and groups that are fastened to the surface of g-C_3N_4 are just the prerequisites for forming interfaces and forming growth and nucleation sites. However, the difference is that the latter supplies suitable conditions for the nanostructures linked with g-C_3N_4 to be fully grown. In other words, they form different morphologies, expose various crystal faces and have controllable crystallinity, which are all considerably crucial for determining the photocatalytic activity of the as-obtained g-C_3N_4-based composites.[156] Tin disulfide spontaneously grows into a typical two-dimensional CdI_2-type layered structure if no limitation is introduced to the crystal nucleation process in the liquid system.[76] In a practical experiment, g-C_3N_4 decorated with zero-dimensional SnS_2 nanodots,[8,76] two-dimensional SnS_2 nano-sheets[165–167] and three-dimensional SnS_2 nano-flowers[168,169] have been fabricated by considering the selection of reactants, the choice of reaction solvents and the design of reaction routes. In one of our previous reports,[76] we firstly dispersed $SnCl_4 \cdot 5H_2O$ and g-C_3N_4 into 25 mL anhydrous ethanol with sonication assistance, then added thioacetamide as a sulfur-source to the mixture after achieving the surface adsorption of Sn^{4+} ions on the surface of g-C_3N_4. Finally, the whole mixture was subjected to a solvothermal reaction at low temperature (100 °C) for 10 h, obtaining the ultrafine SnS_2 dot/g-C_3N_4 sheet composite photocatalyst. Herein, two-dimensional g-C_3N_4 nanosheets not only offer abundant sites for the growth of SnS_2, but also provide a spatial confinement effect to stop it from developing freely as a layered structure. From a paper reported by Bin Dong *et al.*,[165] ultrathin hexagonal SnS_2 nanosheets were synthesized in advance and then mixed with exfoliated g-C_3N_4

Table 2 A summary of the synthetic conditions for various g-C_3N_4-based composites by using the hydro/solvothermal method

Samples		Precursor for preparing g-C_3N_4	Treatment methods of reactants	Synthetic methods (reaction solvents)	Reactive conditions	Ref.
Metal oxides/ hydroxides–g-C_3N_4	MnO_2–g-C_3N_4	Melamine	Ultrasonic treatment + stirring	Hydrothermal	160 °C, 6 h	112
	Fe_2O_3–g-C_3N_4	—	Ultrasonic treatment + stirring	Hydrothermal	150 °C, 4 h	144
	TiO_2–g-C_3N_4	Urea	Ultrasonic treatment	Solvothermal (triiodobenzoic acid)	180 °C, 5 h	145
	NiO–g-C_3N_4	Melamine	Ultrasonic treatment + stirring	Hydrothermal	125 °C, 10 h	146
	Fe_3O_4–g-C_3N_4	Melamine	Ultrasonic treatment	Solvothermal (ethanediol)	200 °C, 12 h	147
	$W_{18}O_{49}$–g-C_3N_4	Melamine	Ultrasonic treatment	Solvothermal (ethanol)	180 °C, 12 h	52
	$NiAl$–LDH–g-C_3N_4	Melamine	Ultrasonic treatment	Hydrothermal	120 °C, 24 h	148
Metal sulfides–g-C_3N_4	CdS–g-C_3N_4	Melamine	Ultrasonic treatment + stirring	Solvothermal (ethanol, water)	180 °C, 12 h	149
	SnS–g-C_3N_4	Cyanamide	Ultrasonic treatment	Solvothermal (ethylene glycol)	200 °C, 10 h	150
	MoS_2–g-C_3N_4	Urea	Ultrasonic treatment + stirring	Hydrothermal	210 °C, 24 h	151
	Co_xS–g-C_3N_4	Urea	Stirring	Solvothermal (ethanol)	120 °C, 5 h	152
	$Zn_{0.8}Cd_{0.2}S$–g-C_3N_4	Urea	Ultrasonic treatment + stirring	Hydrothermal	160 °C, 5 h	153
	$ZnIn_2S_4$–g-C_3N_4	Melamine	Ultrasonic treatment	Hydrothermal	160 °C, 1 h	154
Salt–g-C_3N_4	$K^+Ca_2Nb_3O_{10}^-$–g-C_3N_4	Urea	Ultrasonic treatment	Hydrothermal	140 °C, 12 h	155
	$LaCO_3OH$–g-C_3N_4	Melamine	Ultrasonic treatment	Hydrothermal	160 °C, 12 h	156
	Bi_2MoO_6–g-C_3N_4	Dicyandiamide (DCDA)	Ultrasonic treatment + stirring	Solvothermal (ethanol)	160 °C, 5 h	157
	$BiOCl$–g-C_3N_4	Urea	Stirring	Hydrothermal	160 °C, 6 h	158
	ZnV_2O_6–g-C_3N_4	Melamine	Stirring	Solvothermal (N,N-dimethyl formamide)	200 °C, 24 h	159
	$Bi_2O_2CO_3$–g-C_3N_4	Melamine	Stirring	Hydrothermal	150 °C, 24 h	160
Organic species–g-C_3N_4	Carbon spheres–g-C_3N_4	Melamine	Ultrasonic treatment	Hydrothermal	150 °C, 12 h	161
	Graphdiyne–g-C_3N_4	Urea	Ultrasonic treatment	Hydrothermal	50 °C, 10 h	162
	Graphene quantum dots–g-C_3N_4	Melamine	Stirring	Hydrothermal	150 °C, 4 h	163
	PCN-222(Zr-MOF)–g-C_3N_4	Urea	Ultrasonic treatment	Solvothermal (N,N-dimethyl formamide)	120 °C, 48 h	164

4764 | *Inorg. Chem. Front.*, 2020, **7**, 4754–4793

This journal is © the Partner Organisations 2020

nanosheets in liquid. The mixture was hydrothermally treated at 140 °C for 6 h to strengthen the interface interaction and obtain a SnS$_2$ nanosheets–g-C$_3$N$_4$ nanosheets 2D–2D composite. When the reaction temperature increased to 160 °C, the SnS$_2$ nanostructures presented a flower-like morphology composed of numerous thin SnS$_2$ nanosheets, which came from a self-assembly process. In this experiment,[169] SnCl$_2$ and thioacetamide serve as the Sn-source and sulfur-source, respectively. In detail, SnCl$_2$ was dissolved in acetic acid and then transferred into 55 mL of ethanol with 1.5 g thioacetamide, followed by mixing 20 mL of ethanol containing 400 mg of uniformly dispersed g-C$_3$N$_4$ sheets. The whole reactive precursor mixture was sealed in a Teflon-lined autoclave and maintained at 160 °C for 10 h. SnS$_2$ nanostructures with different microstructures will have differentiated peculiarities of interface contact (point-contact, line-contact or face-contact) with the g-C$_3$N$_4$, in addition to the distinctions of light-harvesting ability and surface-exposed active sites caused by the microstructure differentiation, which all have a great influence on the photocatalytic activity of SnS$_2$–g-C$_3$N$_4$ composites. Other nanostructures conform to this rule as well when forming nanocomposites with g-C$_3$N$_4$. The corresponding types and functions of interface contacts will be discussed and analyzed in section 4: "Types and functions of interfaces".

In summary, both solid-state and liquid-phase based strategies have been developed to construct g-C$_3$N$_4$-based composite photocatalysts with diverse interface contacts. Mechanical mixing/grinding/ball-milling methods are easy to operate and are promising for large-scale applications, finite interface contact, irregular spatial distribution and relatively weak interactions among g-C$_3$N$_4$ and other counterparts in composite systems. The undesired stability is commonly seen from g-C$_3$N$_4$-based composite photocatalysts prepared by this method, reflecting the feeble interactions at the interfaces of various components. Combined with mechanical mixing and heat treatment, the as-obtained g-C$_3$N$_4$-based composite photocatalysts have a stronger interface interaction as compared with mechanical mixing/grinding/ball-milling methods owing to the additional powerful thermal energy; however, the distribution of other components might not be as homogeneous as those composites fabricated in liquid. Whatever the synthetic methods are in liquid, the liquid phase reduction/co-precipitation/self-assembly or hydro/solvothermal, g-C$_3$N$_4$, instead of its precursors, is directly adopted to construct g-C$_3$N$_4$-based composites. Based on the deep realization about the surface physicochemical properties of g-C$_3$N$_4$, it is attainable to modify surface groups and alter surface charges by using facile chemical routes to facilitate the uniform dispersion of g-C$_3$N$_4$ and establish sites to form interface linking.

Chemical bonds and electrostatic adherence are usual interactions at the interfaces of g-C$_3$N$_4$-based composite photocatalysts, which could have a great effect on the interface charge transfer and separation, leading to different catalytic activities for composite photocatalysts with the same components and different interface contacts prepared by diverse methods. A facile heat treatment method was utilized to engineer SnS$_2$–g-C$_3$N$_4$ composite photocatalysts.[170] By using prefabricated SnS$_2$ nanostructures with different morphologies, the area and type of interfacial contact of synthesized SnS$_2$–g-C$_3$N$_4$ composites can be regulated. A more straightforward contact could be realized for distributing SnS$_2$ nanoparticles on g-C$_3$N$_4$ nanosheets than SnS$_2$ nanosheets and nanoflowers, and could contribute to a more efficient charge transfer and separation. In another research effort,[171] Liming Huang *et al.* successfully fabricated TiO$_2$–g-C$_3$N$_4$ 2D–2D composites by using three different methods, co-calcination, solvothermal reaction and charge-induced aggregation. It was demonstrated that the TiO$_2$–g-C$_3$N$_4$ photocatalyst synthesized by solvothermal reaction possessed the highest H$_2$ evolution rate of 587 μmol g^{-1} h^{-1}, which was ascribed to a more boosted migration and separation of photoinduced carriers for the formation of covalent Ti–O–N bonds than electrostatic interactions at the interfaces. For loading CdS on g-C$_3$N$_4$, Zaicheng Sun *et al.*[172] employed two methods of photodeposition and chemical-deposition (hydrothermal reaction) to manufacture two different kinds of CdS–g-C$_3$N$_4$ composite photocatalysts (denoted as p-CSCN and c-CSCN, respectively.). They found that the energy level diagrams and charge transfer routes of the as-obtained p-CSCN and c-CSCN catalysts varied. Different charge transfer mechanisms of p-CSCN (type II) and c-CSCN (*Z*-scheme) catalysts were suggested. It was proposed that the original photodeposition reaction caused a preferred electron flow direction from g-C$_3$N$_4$ to CdS at the interfaces. Enlightened by the above reports, synthetic methods devoted to endowing a better, stronger and more effective contact at the interface are highly preferred and regarded as promising fields to explore.

3.   Techniques for identifying the interfaces

Although the construction of relative composites photocatalysts has broadened the applications of g-C$_3$N$_4$ in a variety of scientific fields and has vastly pushed them into an unprecedented stage for photocatalysis, the present recognitions about the interfaces existing in g-C$_3$N$_4$-based composites are still limited. The majority of researchers have claimed the crucial role of formed interfaces, to differentiate from the simple physical mixing, in giving rise to upgraded photocatalytic activity and stability. Nevertheless, they were not able to elaborate on one of the most essential factors, namely the interfaces, which are determined by the methods for the spatial contact of the various components. The precise interactions at the interfaces matter a lot, being closely related to the light adsorption range, and the transfer and separation states of photo-generated carriers, which, in turn, determine the photocatalytic performances of composites catalysts. In this section, we give an overview of the current progress on characterization techniques for identifying the interfaces of g-C$_3$N$_4$-based materials and the theoretical calculations based

on the interfaces revealed by these techniques. Their advantages and disadvantages are also discussed in detail.

3.1. Characterization of the phase compositions at the interfaces and their spatial distributions

Known as a powerful tool, the X-ray diffraction (XRD) technique has been extensively using to identify phase components of composite materials. As mentioned above, two characteristic peaks at about 13° and 27.4° were detected by XRD, which were indexed to the inter-planar structural packing and interlayer-stacking structure of g-C_3N_4, respectively.[24] For g-C_3N_4-based composites, the distributed location and possible interactions between g-C_3N_4 and other components in the composite system can be inferred from the variations in peak intensity and peak location associated with g-C_3N_4 preliminarily.[101,125,175–177] On the whole, Fig. 11a shows that these characteristic peaks are always present in pure g-C_3N_4 or its composites, indicative of a relatively good structure reservation of g-C_3N_4. Compared with pure g-C_3N_4, the (002) diffraction peak of g-C_3N_4 in the carbon quantum dots–g-C_3N_4 composite (CCN) shifts to a lower angle of 27.07° from the original angle (27.35°),[173] which implies that the interactions formed somehow between the two phases, as well as the increased interlayer distance, were possibly caused by the implantation of carbon quantum dots into the interlayers of g-C_3N_4. However, the (002) peak of g-C_3N_4 moved to

increased diffraction angle values with the introduction and gradual enhancement of Ag (Fig. 11b), resulting in a decreased interlayer distance. It was proposed by the authors from this phenomenon that Ag nanoparticles exist on both the surfaces and interlayers of g-C_3N_4, adjusting the interlayer distance. Here, we consider that it is possible for the squeeze effect of loaded Ag nanoparticles at the surfaces to push g-C_3N_4 layers approaching each other. In research from Yanli Zhao's group (Fig. 11c),[174] the as-developed TiO$_2$ nanotubes-perforated g-C_3N_4 composite (named PGCN/TNTs) showed an almost disappeared (100) peak of g-C_3N_4, which was attributed to a decreased ordering degree of the in-plane structure of g-C_3N_4. Specifically, the in-plane holes could be formed from the interaction of alkaline ions with the in-plane trigonal nitrogen atoms. All these changes are related to the peak position and intensity of g-C_3N_4 and also appear on the C_{60}–g-C_3N_4 composite.[84] As shown in Fig. 11d, the diffraction peak intensities of both the (100) and (002) planes for C_{60}–g-C_3N_4 have been decreased in comparison to those of pure g-C_3N_4. The weakened effect of the former peak is more obvious, proving that the in-plane lattice structure of g-C_3N_4 in C_{60}–g-C_3N_4 has changed after the combination of C_{60}. As suggested by Honggang Fu et al.,[72] importing Au nanoparticles into the in-plane structures of g-C_3N_4 may change the intensity of the (100) plane, which could be suitable for other metal-based species. Hence, the XRD technique could be used to analyze
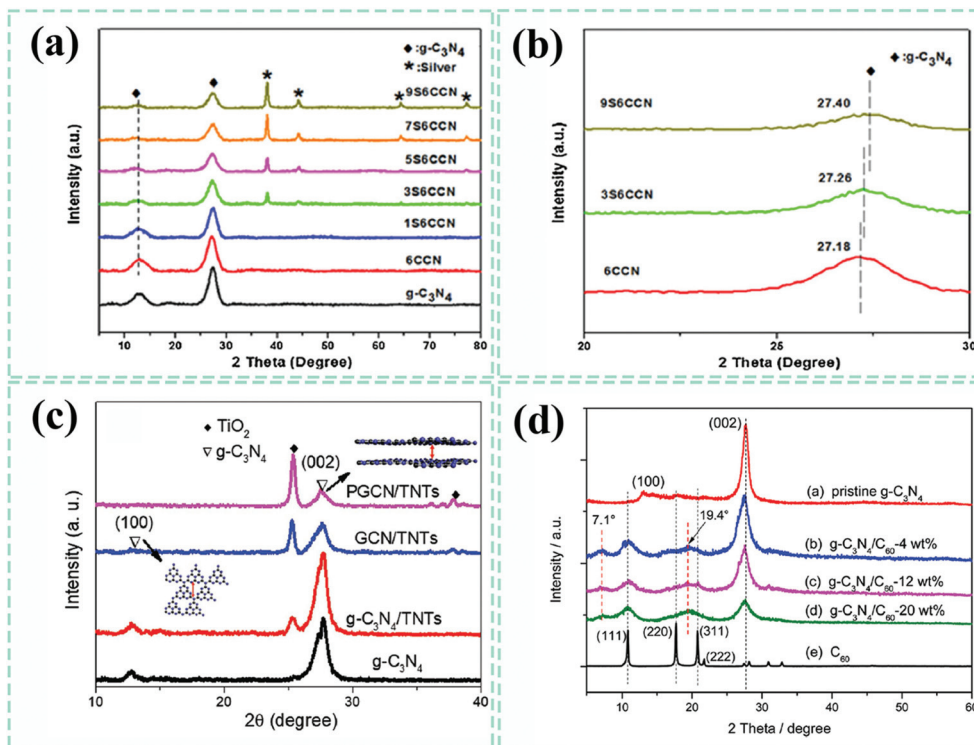

Fig. 11 XRD patterns (a) and enlarged views (b) of pure g-C_3N_4, carbon quantum dots–g-C_3N_4 (CCN) and Ag–carbon quantum dots–g-C_3N_4 (S6CCN) composites. Reproduced from ref. 173 with permission from Elsevier, Copyright 2017. (c) XRD patterns of pure g-C_3N_4 and TiO$_2$ nanotubes–g-C_3N_4 composites. Reproduced from ref. 174 with permission from Wiley-VCH, Copyright 2018. (d) XRD patterns of pure g-C_3N_4, C_{60} and C_{60}–g-C_3N_4 composites. Reproduced from ref. 84 with permission from the Royal Society of Chemistry, Copyright 2017.

4766 | *Inorg. Chem. Front.*, 2020, **7**, 4754–4793

This journal is © the Partner Organisations 2020

the structural variations at the interfaces of g-C$_3$N$_4$ and reflect a roughly spatial distribution state of various components in composites.

The detailed structural allocation of various components in g-C$_3$N$_4$-based composites can be further probed visually by scanning electron microscopy (SEM) and transmission electron microscopy (TEM) techniques. As an effective technique to investigate the morphologies and microstructures of materials, SEM is capable of disclosing the macroscopic and tri-dimensional structures of the as-synthesized materials. To reveal more exact structural features at the interfaces requires more sophisticated instruments that could even observe the atomic configuration patterns at the interfaces, such as spherical aberration-corrected transmission electron microscopy.

Taking the intrinsic 2D structure of g-C$_3$N$_4$ into consideration, the interfaces made up of g-C$_3$N$_4$ and other components can generally be divided into three parts: 0D–2D determined point-contact, 1D–2D determined line-contact and 2D–2D determined face-contact (shown in Fig. 12a).[165] Their typical views are exhibited in Fig. 12b, c and d, respectively, with the Co$_3$O$_4$–g-C$_3$N$_4$ composite,[74] W$_{18}$O$_{49}$–g-C$_3$N$_4$ composite[178] and graphene–g-C$_3$N$_4$ composite[179] as the corresponding representatives. Different interface contact types may display differential interface charge behaviors because of discriminating contact areas and structures. As for 2D–2D contacting composite photocatalysts, two main kinds of interfaces could be formed (Fig. 12e), namely, the intraplane interface and the interplane interface.[39] It is easy to understand that the contact areas of the intraplane and the interplane interfaces also have a big difference. Heping Zeng et al.[180] employed high-resolution TEM measurements to visualize the lattice atoms at the interface of the carbon ring and g-C$_3$N$_4$, which could be deemed as the intra-plane interface. Benefiting from accelerated photogenerated carrier separation, the as-fabricated carbon ring–g-C$_3$N$_4$ composite catalyst gives a much boosted photocatalytic H$_2$ evolution activity. Recently, a metal-free black phosphorus nanosheets/g-C$_3$N$_4$ nanosheets composite photocatalyst was developed.[119] The typical 2D–2D configuration with an inter-planar interface was sufficiently demonstrated by a legible TEM image and its corresponding STEM-EDX mapping with mixing elements, which also showed excellent photocatalytic H$_2$ evolution performance. Through SEM and TEM measurements, we are capable of recognizing the morphologies and microstructures of various components in composite photocatalysts, further laying a solid base for classifying the specific interface contact types.

By browsing the previous reports, we found that almost all the works provided high-resolution TEM images to uncover the spatial distribution state of different components, but only a few could offer atomic-scale resolution information about the interfaces, which we believe is very significant for figuring out the relationship between interfacial features and catalytic performances. It should be noted that the contact types of interfaces and chemical bonds at the interfaces are responsible for interface charge behaviors and photocatalytic mechanisms, subsequently resulting in the final catalytic performances.
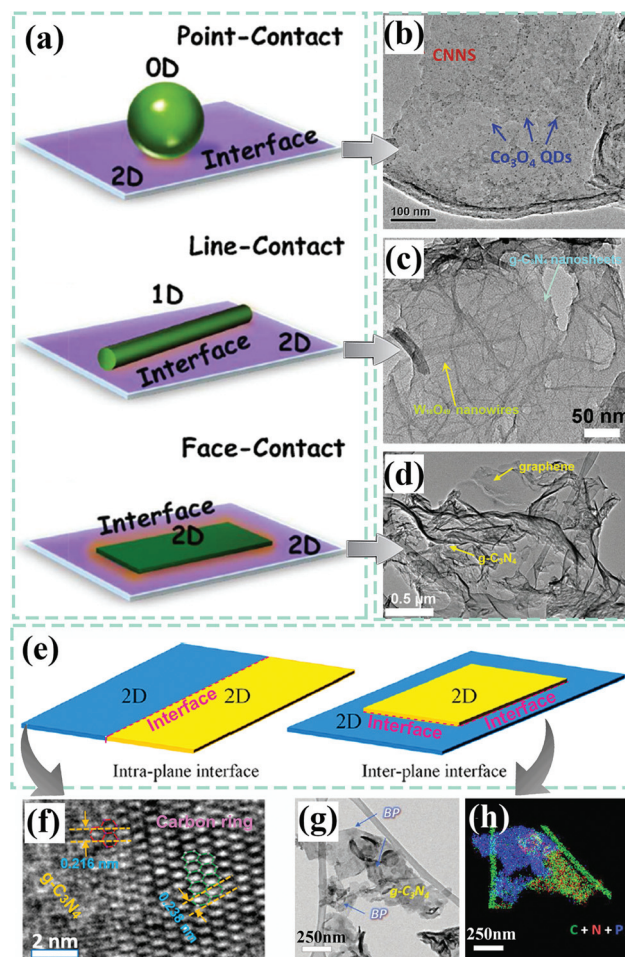

Fig. 12 (a) Graphical illustration of point-contact, line-contact and face-contact interfaces. Reproduced from ref. 165 with permission from Elsevier, Copyright 2015. Typical TEM images of (b) Co$_3$O$_4$–g-C$_3$N$_4$ composite (point-contact), (c) W$_{18}$O$_{49}$–g-C$_3$N$_4$ composite (line-contact), and (d) graphene–g-C$_3$N$_4$ composite (face-contact). (b) Reproduced from ref. 74 with permission from Wiley-VCH, Copyright 2018. (c) Reproduced from ref. 178 with permission from Elsevier, Copyright 2019; (d) reproduced from ref. 179 with permission from the Royal Society of Chemistry, Copyright 2015. (e) Schematic diagram of the intraplane and interplane interface models for 2D–2D composites. Reproduced from ref. 39 with permission from the American Chemical Society, Copyright 2018. (f) High-resolution (HR) TEM image of the carbon ring-g-C$_3$N$_4$ composite. Reproduced from ref. 180 with permission from the American Chemical Society, Copyright 2018. TEM image (g) and STEM-EDX mapping (h) of the black phosphorus–g-C$_3$N$_4$ composite. Reproduced from ref. 119 with permission from Wiley-VCH, Copyright 2018.

Here, we selected two recently published reports to illustrate the importance of revealing the interface contact at the atomic scale. Recently, the authors (Fig. 13a and b) successfully synthesized the α-Fe$_2$O$_3$–g-C$_3$N$_4$ composite and used it as a photocatalyst for CO$_2$ reduction.[144] Compared with the descriptions where the interface is marked with black dotted lines and the two phases containing g-C$_3$N$_4$ and α-Fe$_2$O$_3$ are separated on the two sides of the interface, we found that adopting spherical aberration-corrected transmission electron microscopy

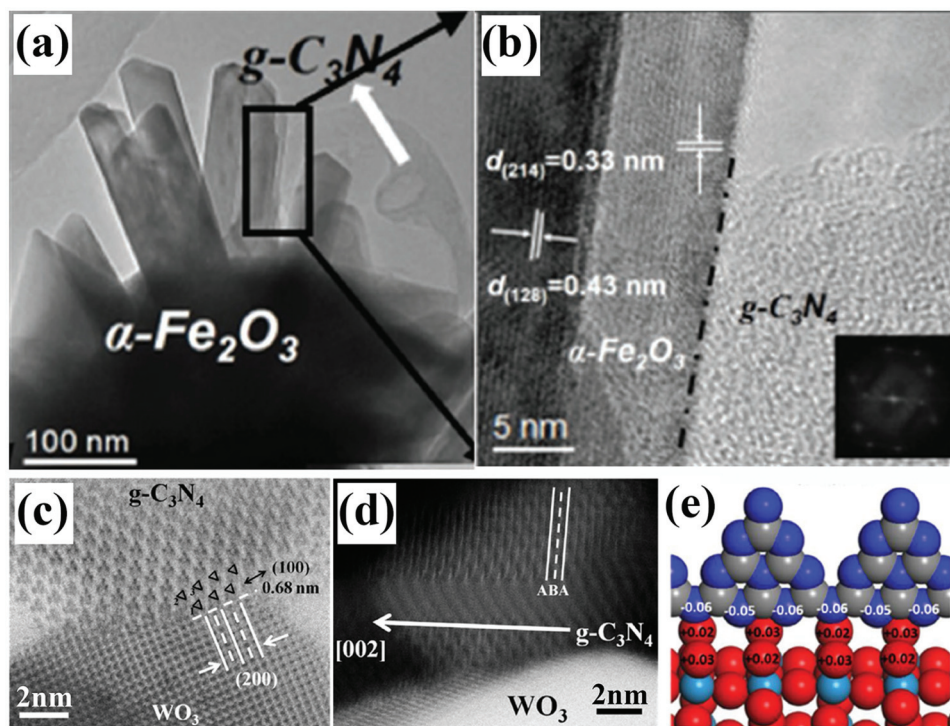**Fig. 13** TEM (a) and HRTEM (b) images of the α-Fe$_2$O$_3$–g-C$_3$N$_4$ composite. Reproduced from ref. 144 with permission from Wiley-VCH, Copyright 2018. Spherical aberration-corrected STEM images of the WO$_3$–g-C$_3$N$_4$ composite: in-plane (c) and interlayer (d) structure of g-C$_3$N$_4$; an ideal structural interface model of the WO$_3$–g-C$_3$N$_4$ composite (e). Reproduced from ref. 103 with permission from Elsevier, Copyright 2017.

allows us to see the interfacial atomic structures and is a better choice that pays more attention to the contact interface, like the face-contact for the 2D–2D configuration, which will supply more information for comprehending the interface carrier behaviors under light irradiation. A direct Z-scheme WO$_3$–g-C$_3$N$_4$ composite photocatalyst was constructed by Weilai Yu *et al.*[103] Based on the distinct characterization on the well-defined interface of g-C$_3$N$_4$ and WO$_3$, the authors were able to rationally design interface models of the WO$_3$–g-C$_3$N$_4$ composite photocatalyst. Combined with other characterizations and photocatalytic properties, the design and understanding of g-C$_3$N$_4$-based composite photocatalysts with interface contact could be provided some new and deep insights.

3.2. Characterization of chemical structures and interactions of the interfaces

Although the interface contact types and spatial distribution states of various components in g-C$_3$N$_4$-based composite photocatalysts have been ascertained, an in-depth understanding of the interface behaviors is needed and requires other detection techniques to reveal the types of interaction forces at the interfaces since the behaviors of photogenerated charge transfer and separation are closely connected with them. These details will be discussed later.

Fourier transform infrared spectroscopy (FTIR) is a crucial technique for probing surface chemical groups and atomic structures, and is commonly used for g-C$_3$N$_4$-based materials.[12] For pure g-C$_3$N$_4$, the peaks in the range of 3000 to

3500 cm^{-1} are generally assigned to N–H stretching vibrations and O–H stretching vibrations associated with adsorbed water.[37,142] A set of peaks between 1200 and 1650 cm^{-1} (area A) belong to the typical stretching vibrations of CN heterocycles,[165,181] while the characteristic peak at about 810 cm^{-1} (area B) is ascribed to the stretching vibration of the s-triazine ring units in g-C$_3$N$_4$.[145,164] All of the above peaks are peculiar to g-C$_3$N$_4$, as exhibited in Fig. 14a. After forming composites by introducing other components, we generally anticipate observing specific vibration peaks from various constituents if they do not overlap with each other. As seen in Fig. 14a, an extra peak for the MnO$_2$–g-C$_3$N$_4$ composite at 493 cm^{-1} corresponds to the stretching vibration of the Mn–O bond, as compared to pure g-C$_3$N$_4$, which could indicate the successful synthesis of the MnO$_2$–g-C$_3$N$_4$ composite.[181] The deficiency is that the interface interactions could not be determined from just the combined spectra. The characteristic peaks of CN heterocycles and the s-triazine ring units in g-C$_3$N$_4$-based composites will shift to higher or lower wavenumbers than those of pure g-C$_3$N$_4$, suggesting possible interface interactions and contact positions between the involved members, just as the Co$_3$O$_4$–g-C$_3$N$_4$ composite displayed in Fig. 14b.[74]

Despite all this, we still had no idea what the interactions were exactly. It is preferable to encounter a situation where some new vibration peaks are seen in the FTIR spectra. These kinds of interactions have much more concreteness and credibility. Besides the vibration peaks from pure graphene oxide (GO) and g-C$_3$N$_4$, the new peak at around 1075 cm^{-1} for the
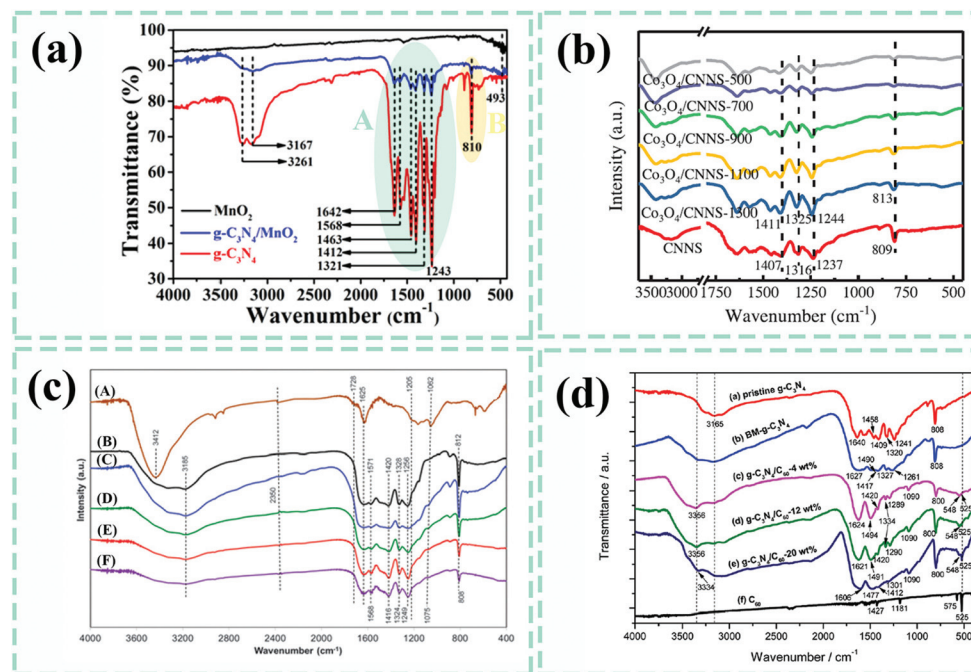
4768 | *Inorg. Chem. Front.*, 2020, **7**, 4754–4793

This journal is © the Partner Organisations 2020

Fig. 14 (a) Fourier transform infrared (FTIR) spectra of MnO_2, g-C_3N_4 and the g-C_3N_4/MnO_2 composite. Reproduced from ref. 181 with permission from the American Chemical Society, Copyright 2017. (b) FTIR spectra of g-C_3N_4 nanosheets (denoted as CNNS) and Co_3O_4–g-C_3N_4 nanosheets (denoted as Co_3O_4/CNNS-x) composites. Reproduced from ref. 74 with permission from Wiley-VCH, Copyright 2018. (c) FTIR spectra of (A) GO, (B) g-C_3N_4, (C–F) graphene–g-C_3N_4 composites. Reproduced from ref. 179 with permission from the Royal Society of Chemistry, Copyright 2015. (d) FTIR spectra of C_{60}, g-C_3N_4 and C_{60}–g-C_3N_4 composites. Reproduced from ref. 84 with permission from the Royal Society of Chemistry, Copyright 2017.

graphene–g-C_3N_4 composite marks the C–O–C bonds linking the two components.[179] Similarly, a new vibrational peak at 548 cm^{-1} in the FTIR spectra of C_{60}–g-C_3N_4 composites indicate the formation of some kind of chemical bond at the interface of C_{60} and g-C_3N_4.[84] With the help of the FTIR spectra, we can determine the possible positions where the interactions exist; CN heterocycles or s-triazine ring units. Of course, the newly-formed chemical bonds could be thought of as interface interactions, which could provide convincing evidence for confirming the precise interface interactions. However, we are not always able to obtain such information, so further concrete evidence is needed.

High-resolution X-ray photoelectron spectroscopy (XPS) is a powerful tool for investigating the interactions and surface chemical structures at the interface of composites.[76,118] For pristine g-C_3N_4, the C 1s high-resolution XPS generally shows two peaks at 284.6 ± 0.3 eV and 288.0 ± 0.4 eV, correlating to sp^2 C–C bonds and sp^2-hybridized aromatic N–C=N bonds, respectively.[39,98,133] With respect to the high-resolution XPS of N 1s, three peaks at 398.5 ± 0.3 eV, 399.6 ± 0.3 eV and 400.7 ± 0.3 eV could be observed, corresponding to C–N=C bonds in triazine rings, N–(C)$_3$ groups and surface C–N–H amino groups, respectively.[163,181,184] In view of the g-C_3N_4 species prepared by various methods, the surface chemical states related to C 1s and N 1s might exhibit a difference, which is easy to understand. After coupling with other components, the elemental de-convoluted peaks of composite photocatalysts

shift to another binding energy position as compared with the monomer, which implies possible electron migration through the interface interactions. In a report about black phosphorus quantum dots (BPQDs)–g-C_3N_4 composite photocatalysts,[120] the P 2p$_{3/2}$ and P 2p$_{1/2}$ doublets gave a negative shift of about 0.5 eV relative to those of BPQDs, while a tiny positive shift (~0.1 eV) for N–C=N groups (N 1s) of BPQDs–g-C_3N_4 was observed in comparison to that of pure g-C_3N_4. This demonstrated the existing electron transfer from g-C_3N_4 to BPQDs upon interface couplings. Similarly, Xuefeng Yu et al.[83] developed a black phosphorus nanosheets–g-C_3N_4 (BP/CN) composite and found that the divided peaks in N 1s for BP/CN exhibited a more negative binding energy as compared to those of pure g-C_3N_4. Furthermore, in the high-resolution XPS of P 2p, a new peak for BP/CN emerged at 133.4 eV, which was indexed to P–N bonding integrating black phosphorus and g-C_3N_4 at the interfaces. In order to confirm that the peak shift is caused by the formation of an interface, Tetsuro Majima et al.[182] compared the peak shift states of C 1s and N 1s by setting three relevant samples, pure g-C_3N_4, the mixture of g-C_3N_4 and MoS_2 (Mix-6.4%), and the MoS_2–g-C_3N_4 composite (MC-3.2%). They found that the high-resolution of C 1s and N 1s in MC-3.2% displayed a lower shifted binding energy of ~0.6 eV as compared to pure g-C_3N_4, while the Mix-6.4% sample showed no shift, which further confirmed the electron effect at the interface by constructing hetero-interfaces instead of physical mixing. Using calculation methods to better elucidate the

This journal is © the Partner Organisations 2020

Inorg. Chem. Front., 2020, **7**, 4754–4793 | **4769**

interface effect for photocatalysis, we aimed to determine the exact interactions and chemical bonds. Bin Dong *et al.*[165] employed the XPS technique to analyze the possible existing chemical interactions at the interface of the as-obtained 2D–2D SnS_2-g-C_3N_4 composite. C–S and Sn–N bonds were ascertained by comparing the high-resolution XPS of C 1s, S 2p, N 1s and Sn 3d in g-C_3N_4, SnS_2 and the SnS_2-g-C_3N_4 composite. Based on these results, they built the possible interface bonding configuration model of SnS_2 and g-C_3N_4, which we believe is significant for interface charge behaviors. For the CoP–g-C_3N_4 composite fabricated by Rong Xu *et al.*,[183] the formation of Co–N bonds at the interface of CoP and g-C_3N_4 was proven and highlighted (Fig. 15). Undoubtedly, the identification of interface interactions helps with understanding the photocatalytic mechanism and rationally designing g-C_3N_4-based composite photocatalysts. Nevertheless, the practical peak deconvolution process is random, making the XPS technique not convincing enough with sufficient proof. Some options combine various techniques, but we still require more precise characterization techniques.

Synchrotron radiation-based X-ray absorption spectroscopy (XAS), including X-ray absorption near edge structure (XANES) and extended X-ray absorption fine structure (EXAFS), has been widely applied to disclose the density of states, atomic coordination structure and environment of nanomaterials in various subjects and fields, especially for nanoscale materials for catalytic applications. To date, there have been quite a few reports related to g-C_3N_4-based composite photocatalysts that made use of this technique to provide further evidence of atomic structure information (Fig. 16).

For the previously reported hybrid black phosphorus quantum dots (BPQDs)–g-C_3N_4 composite (BPQDs/g-C_3N_4) and the phosphorene/g-C_3N_4 (1.8 PCN) composite,[80,120] the XANES N K-edge for the composites all shifted to a much higher photon energy position, while the P K-edge underwent a negative shift to a lower photon energy position, as compared with that of pristine g-C_3N_4, demonstrating the electron migration from g-C_3N_4 to phosphorus-species through the interface interactions. Rong Xu *et al.*[183] validated the formation of Co–N bonds at the interface of the CoP–g-C_3N_4 composite by using the Co K-edge XANES and EXAFS spectra. The Co absorption edge in the XANES spectrum of CoP/g-C_3N_4 exhibited an obvious positive shift to a higher energy position relative to that of CoP. In the fitted curves for the first peak of the corresponding EXAFS spectrum, the coordination number and bond distance for Co–P were 1.2 and 0.241 nm, while those of Co–N
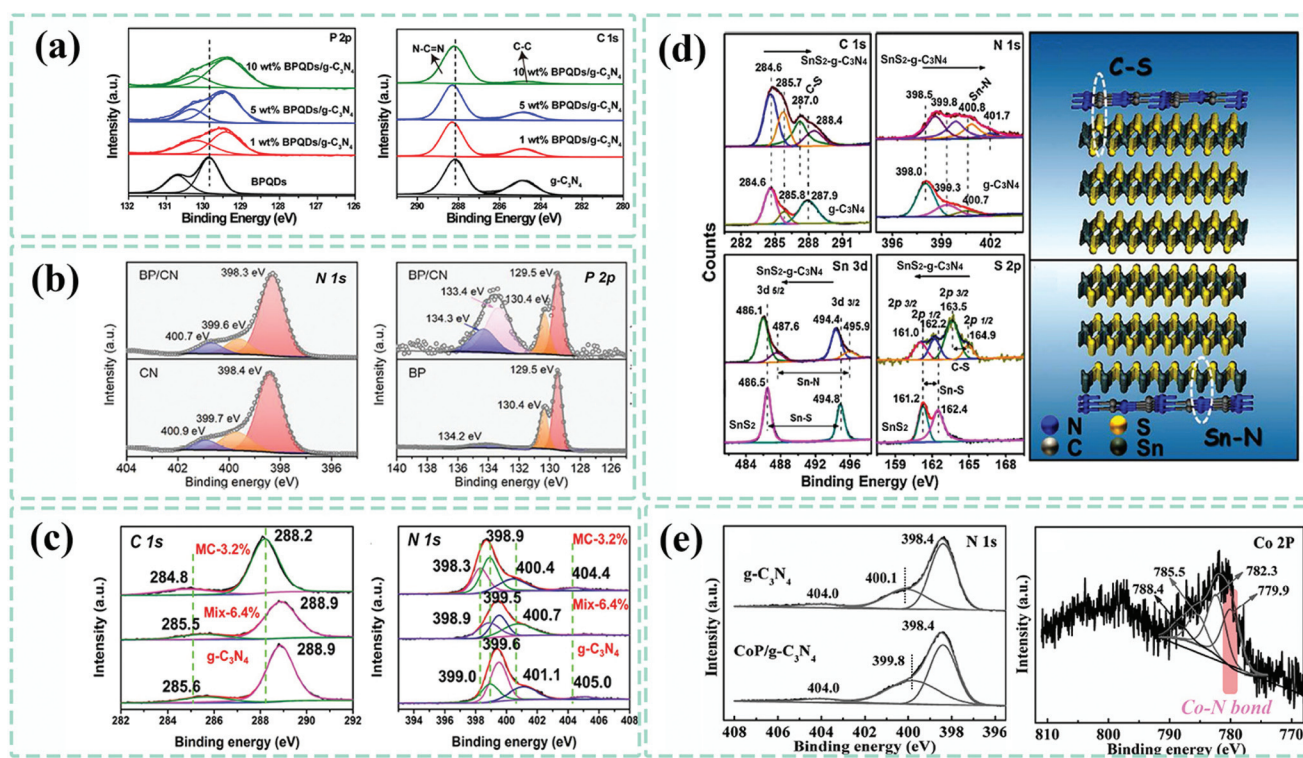

Fig. 15 (a) High-resolution X-ray photoelectron spectroscopy (XPS) of P 2p and C 1s for black phosphorus quantum dots (BPQDs), g-C_3N_4 and BPQDs–g-C_3N_4 composites. Reproduced from ref. 120 with permission from Elsevier, Copyright 2018. (b) High-resolution XPS of N 1s and P 2p for black phosphorus (BP) nanosheets, g-C_3N_4 (CN) and the BP–g-C_3N_4 (BPCN) composite. Reproduced from ref. 83 with permission from Wiley-VCH, Copyright 2018. (c) High-resolution XPS of C 1s and N 1s for pure g-C_3N_4, the mixture of g-C_3N_4 and MoS_2 (Mix-6.4%) and the MoS_2–g-C_3N_4 (MC-3.2%) composite. Reproduced from ref. 182 with permission from Wiley-VCH, Copyright 2018. (d) High-resolution XPS of C 1s, N 1s, Sn 3d and S 2p for g-C_3N_4, SnS_2 and the SnS_2–g-C_3N_4 composite, along with the schematic diagram of possible chemical bonds at the interfaces. Reproduced from ref. 165 with permission from Elsevier, Copyright 2015. (e) High-resolution XPS of N 1s and Co 2p for g-C_3N_4 and the CoP–g-C_3N_4 composite. Reproduced from ref. 183 with permission from Wiley-VCH, Copyright 2016.

4770 | *Inorg. Chem. Front.*, 2020, **7**, 4754–4793

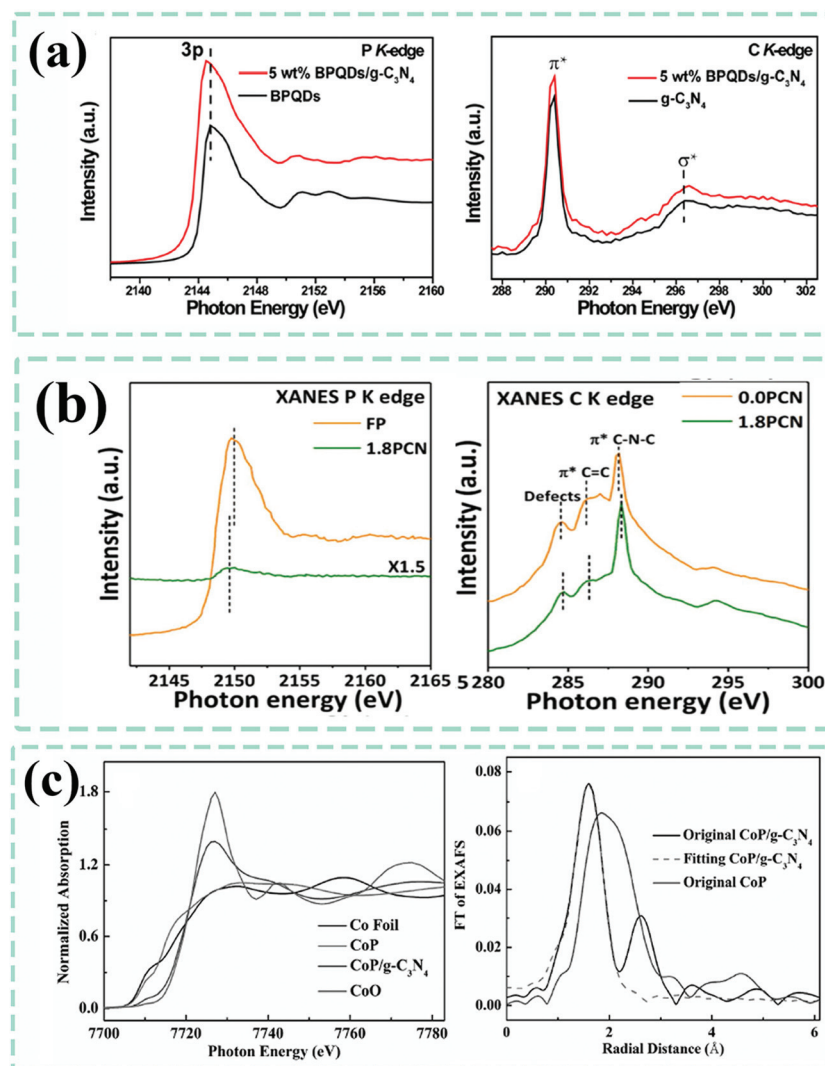This journal is © the Partner Organisations 2020

Fig. 16 (a) Synchrotron radiation-based X-ray absorption near edge structure (XANES) of the P K-edge and C K-edge for different samples. Reproduced from ref. 120 with permission from Elsevier, Copyright 2018. (b) XANES P K-edge and C K-edge of g-C_3N_4 (0.0 PCN) and phosphorene–g-C_3N_4 composite (1.8 PCN). Reproduced from ref. 80 with permission from Wiley-VCH, Copyright 2018. (c) XANES Co K-edge spectra and the corresponding Fourier transform (FT) of the extended X-ray absorption fine structure (EXAFS) spectra of various samples. Reproduced from ref. 183 with permission from Wiley-VCH, Copyright 2018.

were 4.2 and 0.206 nm, indicative of the presence of Co–N bonds at the interfaces. Therefore, synchrotron radiation-based techniques do assist a lot with the identification of the atomic chemical environment and have been widely and extensively applied in transition metallic-based single-atom catalysts. We believe that they will contribute significantly to recognizing the chemical structures at the interfaces of g-C_3N_4-based composites as well, suggesting that combining them with other techniques would be wise.

To better investigate the roles of interfaces, the elementary requirement is to gain an in-depth understanding of their modes of contact and the existing interactions (such as chemical bonds) of the g-C_3N_4-based composite photocatalysts. The XRD technique could determine the phase composition and roughly outline the spatial distribution of various components,

while the in-plane and interlayer structure variations of g-C_3N_4 substances could also be speculated. The morphology, microstructure and spatial distribution, particularly atomic arrangement and configuration at the interfaces, can be determined by using SEM and TEM-related techniques visibly and objectively. There are always some kinds of interactions working at the interfaces of these g-C_3N_4-based composites, or there will be no differences between the as-synthesized composites and simple mixtures. If chemical interactions exist, we should figure out what exactly they are and which chemical bonds the diverse components interconnect with. At this point, a combined utilization of various techniques including but not limited to FTIR spectra, XPS and synchrotron radiation-based XAS would contribute a lot to the affirmation of chemical bonds at the interfaces. However, in most cases, the authors

This journal is © the Partner Organisations 2020

Inorg. Chem. Front., 2020, **7**, 4754–4793 | **4771**

still cannot verify the type of chemical bonds instead of the charge migration direction demonstrated by the corresponding peak shifts and the peak intensity variations. We anticipate that more new and accurate techniques could be put into practice for identifying the interface interactions of g-C_3N_4-based photocatalysts.

4. Types and functions of the interfaces

In the development of methods to build interfaces or finding more precise and advanced characterization techniques to understand interfaces, the ultimate purpose lies in gaining in-depth insight into the role of interfaces allowing the customization for fabricating g-C_3N_4-based composite photocatalysts with varied and robust interface contacts, leading to satisfactory catalytic activity and stability to meet the requirement of large-scale commercial applications. In this section, we make basic classifications based on the interfaces formed from combined phases with g-C_3N_4 in a specific composite photocatalyst system. The contact area and type of existing interfaces maintain a close relationship with the phase components in g-C_3N_4-based composites and their modes of contact. Here, we discuss two divisions of interfaces, namely, two-phase interfaces and multi-phase interfaces. The functions of various interfaces in g-C_3N_4-based composites for photocatalysis are discussed and analyzed in detail.

4.1. Two-phase interfaces

Other nanostructures are usually integrated with g-C_3N_4 to produce two-phase interfaces that can maximize the advantages of the components involved in the composites. It is also relatively easy to determine the underlying roles of these interfaces but it is limited to realizing the real media used for accelerating the charge transfer and separation between two components. In the macroscopic view, the as-demonstrated functions of interfaces, such as boosting the light-harvesting capability, suppressing the recombination of photo-generated electron/hole pairs, and facilitating the migration and transfer of charge carriers, are attributed to the contacts and are responsible for the much enhanced photocatalytic performances. Unfortunately, in most cases, we still have no idea about these processes and how they are conducted, the kinds of chemical bonds at the interfaces, or the involved atoms from each component because they are actually microcosmic. To achieve the above-mentioned advantages, we need to determine the prerequisites such as the kinds of chemical bonds that exist at the interfaces and how they combine to form the interfaces. We believe that these issues should be most urgently solved and they have the potential to lead the way for future development related to high-performance g-C_3N_4-based composite photocatalysts. Therefore, we provide herein a comprehensive analysis of the as-developed g-C_3N_4-based composites with two-phase interfaces and propose possible interactions between g-C_3N_4 and another phase.

4.1.1. Noble-metallic species–g-C_3N_4 interfaces. Among the noble-metallic species–g-C_3N_4 composites, which are generally Au–g-C_3N_4,[185,186] Ag–g-C_3N_4,[132] Ag-based compounds–g-C_3N_4,[128,130] Pt–g-C_3N_4[187,188] and Pd–g-C_3N_4[189,190] composites, the exact interface interactions are only mentioned in a limited number of reports. However, we find that three synthetic methods, namely, chemical reduction,[123] photo-reduction,[126] and *in situ* co-precipitation,[130] are usually adopted to obtain the noble-metallic species–g-C_3N_4 composites. All of the methods involve the chemical adsorption of noble-metallic ions onto g-C_3N_4 substances prior to the formation of noble metal nanoparticles or their compounds. On this basis, we speculate that the real interfacial interactions of such g-C_3N_4-based composites are highly possible electron interactions.[189] Another proposed interaction at the interfaces is electrostatic adherence.[191] For example, Huiyu Liu el al.[189] employed an *in situ* reduction method to prepare the Pd–g-C_3N_4 composite with electronic interactions (Fig. 17a–c) by loading uniformly monodispersed Pd nanosheets with an average edge length of ∼25 nm. The intimate electronic interactions between g-C_3N_4 and Pd were confirmed by the Pd^0 peak shift of ∼0.3 eV. In contrast, the same kind of composite with electrostatic adherence interactions showed morphological incompatibility and interfaces with poor contact. Similarly, *in situ* chemical reduction and photo-reduction methods for other noble-metallic species–g-C_3N_4 composites likely possess strong electronic interactions. Most of the g-C_3N_4-supported noble-metallic species are nanoparticle-like, with a 0D structure (0D–2D interface). Still, the nanocrystal size, shape and loading amount of noble metallic species are completely different, which results in varied charge behaviors because of different interface contacts and light-harvesting abilities, further giving rise to distinguished photocatalytic performances. Jiaguo Yu *et al.*[192] successfully loaded Pt nanocrystals with different shapes onto g-C_3N_4 nanosheets (Fig. 17d–g) through electrostatic adherence interactions by controlling the pH of the dispersion solution to regulate the surface potential of Pt and g-C_3N_4. Among the as-developed Pt–g-C_3N_4 composites (cubic Pt/g-C_3N_4, octahedral Pt/g-C_3N_4 and spherical Pt/g-C_3N_4), spherical Pt/g-C_3N_4 showed the optimal photocatalytic H_2 evolution activity, in which we propose that varied interface contacts also influence their properties. Organic functional groups are highly likely attached to the periphery of the noble metal cluster during the synthetic period, which could serve as a bridge to link with surface functional groups of g-C_3N_4. In this way the photogenerated charges can achieve migration and transfer from one to the other, resulting in improved catalytic performance.

In addition to the interfaces triggering the effective migration and separation of photoinduced charges, the surface plasmon resonance (SPR) effect, influenced by noble metallic particle size, shape, surrounding environment, dielectric properties, and interparticle interactions, also plays an important role in broadening light absorption, adjusting, and altering the electron behaviors at the interfaces.[193] As a rule, noble-metallic particles have a much higher work func-
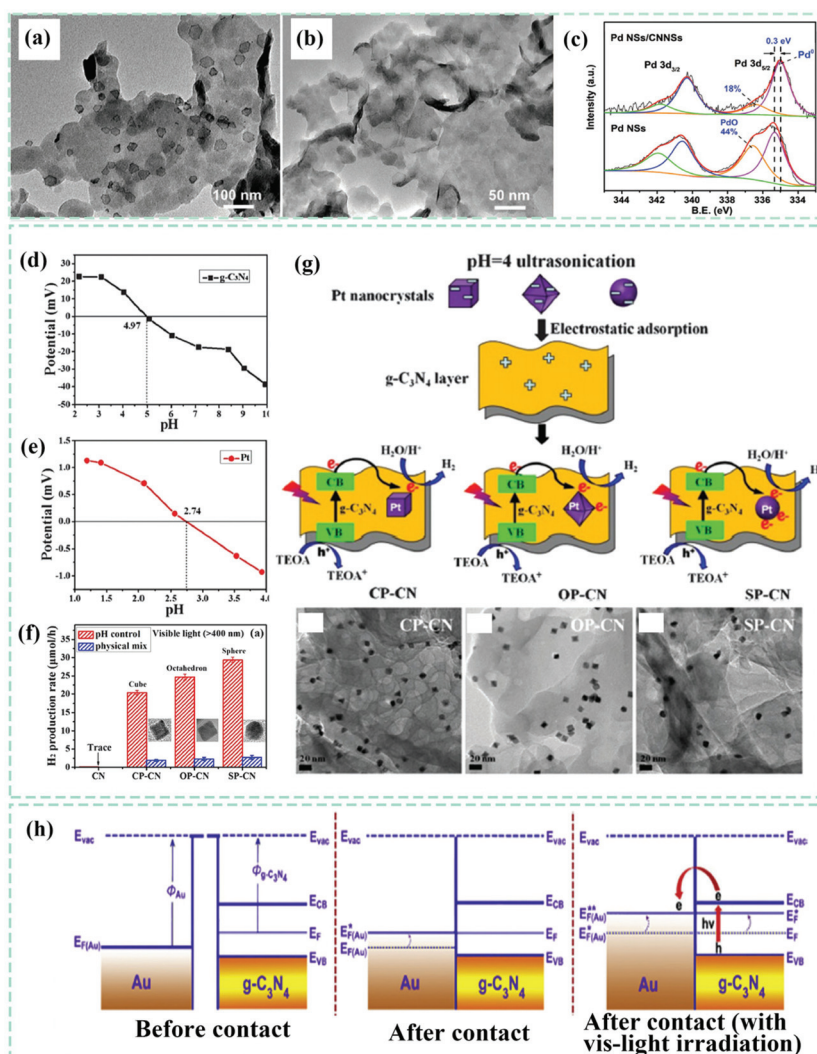
4772 | *Inorg. Chem. Front.*, 2020, **7**, 4754–4793

This journal is © the Partner Organisations 2020

Fig. 17 TEM images of (a) a Pd nanosheets–g-C_3N_4 composite prepared by the *in situ* growth strategy, (b) Pd nanosheets + g-C_3N_4 fabricated by electrostatic interactions, and (c) Pd 3d high-resolution XPS of Pd nanosheets and the Pd nanosheets–g-C_3N_4 composite. Reproduced from ref. 189 with permission from Wiley-VCH, Copyright 2018. (d) and (e) Zeta potentials of g-C_3N_4 and the Pt suspension with different pH values. (f) The synthetic route and TEM images of various Pt–g-C_3N_4 composites. (g) Photocatalytic H_2 evolution activity of various samples. Reproduced from ref. 192 with permission from the Royal Society of Chemistry, Copyright 2016. (h) The charge-transfer mechanism of the as-fabricated Au–g-C_3N_4 composite system: before contact, after contact and after contact with visible light irradiation. Reproduced from ref. 122 with permission from Elsevier, Copyright 2017.

tion (Φ) than that of g-C_3N_4. Once forming interfacial contact, the Fermi level of the noble-metallic particles and g-C_3N_4 will shift to achieve an equilibrium. Therefore, the photogenerated electrons from the conduction band (CB) of g-C_3N_4 transfer to the noble-metallic nanoparticles through the well-defined interfaces; *i.e.*, strong electronic interactions exist at the interfaces. In this way, the coupling of noble-metallic nanoparticles could increasingly accumulate electrons and then use them to participate in photocatalytic reactions. Just like the reported Au–g-C_3N_4 composite system (Fig. 17h),[122] Au nanoparticles were distributed on g-C_3N_4 as indicated above to achieve the goal of facilitating the separation of photoexcited electron–hole pairs from g-C_3N_4 and boosting the availability of charges.

4.1.2. Oxides/chalcogenides–g-C_3N_4 interfaces. To date, various kinds of oxides/chalcogenides–g-C_3N_4 interfaces have been realized by integrating g-C_3N_4 with other phases, including but not limited to TiO_2,[101,174,194] SnO_2,[184] MnO_2,[181] CeO_2,[7] NiO,[98] Co_xO_y,[74,104] Bi_2O_3,[195] W_xO_y,[52,103] Fe_xO_y,[105] $CuBi_2O_4$,[196] MoS_2,[71,182] NiS,[175] SnS_2,[76] CoS_x,[152] $ZnCdS$,[153] Cu_2WS_4[197] and $ZnIn_2S_4$.[154] Among these oxides/chalcogenides–g-C_3N_4 composites, it is proposed that all the interfaces possess the dominant ability to regulate photogenerated charge behavior. Still, only a few reports indicate the existence and confirm the type of chemical interaction. We highlight the significance of these works even though they seem not to be so precise and convincing to us at the present stage because of the restriction of characterization techniques. However, efforts were made to

provide an objective revelation about photoinduced charge behaviors at the interfaces. For example, C–O, O–N and C–S/ Sn–N bonds have been demonstrated in as-synthesized NiO–g-C_3N_4,[98] TiO_2–g-C_3N_4,[171] WO_3–g-C_3N_4[103] and SnS_2–g-C_3N_4 composites,[76,165] of which the authors emphasize the crucial role of these bonds in effective carrier migration and separation along with the acceptable stability of the corresponding composite catalysts.

4.1.3. Carbides/nitrides/borides/phosphides–g-C_3N_4 interfaces. Classified as co-catalysts, Ni_3C,[96] Ti_xC_y,[48,106,198] Ni_3N,[199,200] Ni_xB_y,[201] Ni_xP_y,[49,202] Co_xP_x,[183,203] Cu_xP,[95] MoP,[111] FeP,[46] NiCoP,[204] and so on, have been loaded onto g-C_3N_4 nanosheets to generate the corresponding composites. It is worth mentioning that Rong Xu et al.[183] confirmed the presence of Co–N bonds at the interfaces between g-C_3N_4 and CoP by using XPS and XANES measurements. They believe that these Co–N bonds could contribute many dual active sites to create synergistic effects, and also broaden the visible light harvesting range, match the band positions and improve the separation efficiency of charge carriers. All of these are appropriate for the NiB–g-C_3N_4 composite,[201] in which the existence of Ni–N bonds has been proved. In another CoP–g-C_3N_4 system,[75] the authors recommended the formation of P–N bonds that are interconnected with the two components, facilitating the migration and transfer of charge carriers. Currently, we are not able to decide which proposal is right because different synthetic routes could lead to diverse interfacial atomic contacts or chemical bonds. We anticipate that more advanced electron microscope and spectroscopy techniques could be adopted to uncover the interfacial atomic arrangement and bonding mode to better construct theoretical calculation models and understand the roles and interfaces.

4.1.4. Perovskites/halides–g-C_3N_4 interfaces. Perovskites, due to their specific physicochemical properties, have been extensively applied in the fields of electronics and energy science. Perovskite oxides,[38,69,97,205,206] perovskite halides[143] and perovskite oxyhalides[66] are three common species in the perovskite family, which are also applied in engineering g-C_3N_4-based composites, showing enhanced photocatalytic activity with interfacial effects similar to those mentioned above. Analogous to polymetallic oxides/sulfides, the surfaces of perovskites are composed of multiple exposed atoms, which means it is extremely hard to tailor and customize perovskites–g-C_3N_4 composites with specific interface interactions (chemical bonds). Taking the $CsPbBr_3$ perovskite as an example, Rong Xu et al.[143] determined that the generated N–Br bonds are beneficial for accelerating charge separation and prolonging the lifetime of the charge carriers in the as-obtained $CsPbBr_3$–g-C_3N_4 composite catalyst. Since the interactions at the interfaces in perovskite–g-C_3N_4 and halides–g-C_3N_4 composites are absent or not clear,[207–209] it is difficult to ascertain the interfacial bonding, which could be a challenge for subsequent investigations.

4.1.5. Salt compounds–g-C_3N_4 interfaces. Distinguished from perovskites and halides, we have defined other salt-based compounds–g-C_3N_4 composites as interfacial nanostructures. As a special class that exists stably in nature among salt-based compounds, Bi-salts, possessing the superiorities of natural abundance, suitable band structures, nontoxicity, specific crystal structures, high thermal and chemical stability,[67,158,160] have been combined with g-C_3N_4 to incubate a high-efficiency photocatalytic system, caused by the interfaces-induced effective transfer and separation of photogenerated charge-carriers.[88,210] For these research efforts, the chemical interactions at the interfaces remain a mystery. This problematic situation also exists for other salt-based species. As shown in Fig. 18a and b, Zhurui Shen et al.[131] used an in situ adsorption and ultrasound-assisted crystallization method to fabricate a $AgVO_3$ quantum dots–g-C_3N_4 composite for the photodegradation of organic dye, demonstrating the significantly improved photoexcited charge separation and interfacial charge transfer on the interfaces. In light of its original synthesis route, we guess that the interfacial interactions between $AgVO_3$ and g-C_3N_4 are most likely via the Ag (δ^+)–N (δ^-) bond, which actually makes a big difference in helpful photogenerated charge behaviors and will be verified in the future. In a well-designed ZnV_2O_4–g-C_3N_4 composite system, Muhammad Tahir et al.[159] introduced a special protonated layer onto the surface of g-C_3N_4 for comparing the photocatalytic behaviors of the ZnV_2O_4-protonated g-C_3N_4 and common ZnV_2O_4–g-C_3N_4 composites. As depicted in Fig. 18d and e, this protonated layer could act as an agent to trap photoexcited electrons, thus promoting the migration and separation of photogenerated charge carriers. It is reasonable to believe that a built-in interfacial electric field is formed through electrostatic interactions. Previous reports have indicated that crystal facet engineering enables the regulation of photoinduced carrier behaviors on different crystal facets. For $BiVO_4$, the excited electrons and holes tend to accumulate at the [010] and [110] facets under visible light irradiation. Inspired by this recognition, Guoqiang Tan et al.[37] developed a [010] $BiVO_4$–g-C_3N_4 composite (Fig. 18f) through the electrostatic adsorption of negatively charged $BiVO_4$ [010] facets and surficial protonated g-C_3N_4. Similarly, a built-in electric field (Fig. 18g) could drive photogenerated electrons to migrate along the interfacial contact. These achievements are convincing, and we would like to know more details about the interfaces, both visibly and invisibly. If these are atomic contacts and chemical bonds existing at the interfaces, they surely give priority to the influence on charge-carriers rather than electrostatic interactions.

4.1.6. Black phosphorus relatives/organics-related species– g-C_3N_4 interfaces. So far, black phosphorus relatives, carbon-based species and metal–organic frameworks have been deemed as three of the most popular nanostructures for coupling with g-C_3N_4. Unlike inorganic nanocrystals, they have huge potential to form covalent chemical bonds with the surface atoms of g-C_3N_4, which makes these kinds of interfaces much easier to design and fabricate.

Due to their earth-abundance, tunable and suitable thickness-dependent bandgap (0.3–2.0 eV), broad solar light-harvesting ability and high charge carrier mobility, there has been tremendous interest in loading black phosphorus relatives with varied dimensions and layers on g-C_3N_4.[115,117,121] Three
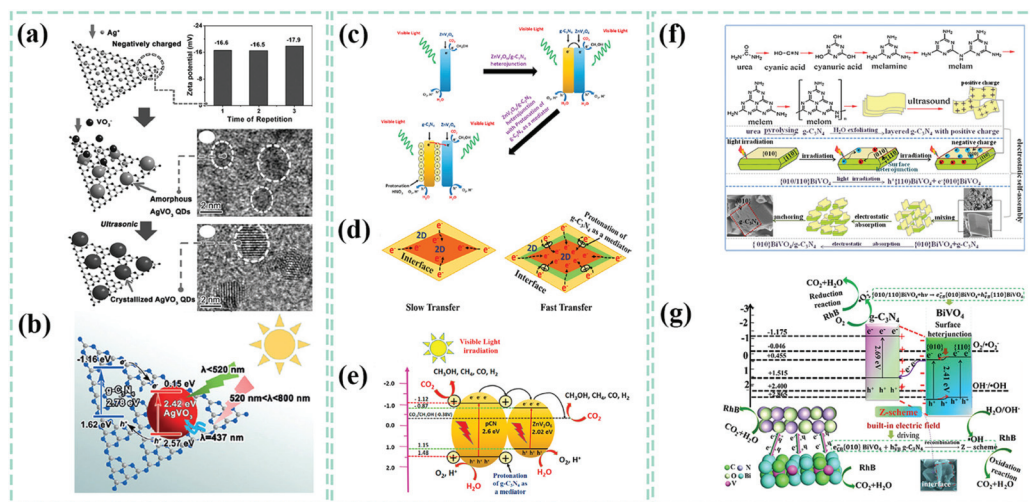
4774 | *Inorg. Chem. Front.*, 2020, **7**, 4754–4793

This journal is © the Partner Organisations 2020

Fig. 18 (a) Formation mechanism of the AgVO₃–g-C₃N₄ composite, zeta potential values of g-C₃N₄ and the corresponding HRTEM images of the AgVO₃–g-C₃N₄ composite. (b) The proposed catalytic mechanism of the AgVO₃–g-C₃N₄ composite. Reproduced from ref. 131 with permission from Wiley-VCH, Copyright 2017. (c) Possible mechanism of the photo-reduction of CO_2 over as-obtained ZnV_2O_6, ZnV_2O_6–g-C₃N₄ and ZnV_2O_6–pCN composites. (d) Graphical illustration of the charge transfer of contact interfaces for ZnV_2O_6–g-C₃N₄ and ZnV_2O_6–pCN composites. (e) Photocatalytic mechanism of the ZnV_2O_6–pCN composite catalyst. Reproduced from ref. 159 with permission from Elsevier, Copyright 2018. (f) Synthetic route for the [010] facets of the $BiVO_4$–g-C₃N₄ composite photocatalyst. (g) Possible photocatalytic mechanism over [010] $BiVO_4$–g-C₃N₄ under visible light irradiation. Reproduced from ref. 37 with permission from Elsevier, Copyright 2018.

sorts of interfacial interactions, corresponding to van der Waals forces,[80] C–P bonds[120,211] and N–P bonds,[83,114,118,212] are proposed based on phosphorene–g-C₃N₄, black phosphorus quantum dots (BPQDs)–g-C₃N₄ and black phosphorus nanosheets–g-C₃N₄ composites, respectively. As shown in Fig. 19a, Shizhang Qiao *et al.*[80] fabricated a few-layered phosphorene–g-C₃N₄ heterojunction by exfoliating bulk black phosphorus into two-dimensional phosphorene and then mixing it with two-dimensional g-C₃N₄ nanosheets *via* a grinding process. Thanks to the van der Waals interactions at the interfaces, the high separation and transfer capacity of photogenerated electron–hole pairs for g-C₃N₄ to phosphorene and the prohibited charge-carrier recombination could be achieved in the phosphorene–g-C₃N₄ heterojunction when used as a photocatalyst for H_2 evolution, showing a H_2-production rate of 571 μmol h⁻¹ g⁻¹. A facile sonication approach was applied by Gang Liu *et al.*[120] to synthesize the 0D–2D BPQDs–g-C₃N₄ hybrids, displaying much-enhanced photocatalytic activity of up to 271 μmol h⁻¹ g⁻¹. It was recommended that the interfacial contact through C–P bonds, revealed by FTIR, XPS and XANES spectra and leading to effective transfer and separation of charge-carriers, are the main reasons for this. Dongling Ma *et al.*[119] reported a 2D/2D black phosphorus–g-C₃N₄ heterostructure, in which they came up with another possible interfacial interaction, N–P bonds. They made this speculation depending on the high-resolution XPS spectra of N 1s and P 2p. In a photocatalytic H_2 evolution experiment, photo-excited electrons and holes of g-C₃N₄ were provided a chance to transfer to black phosphorus on the interfaces, promoting their efficient utilization. This was realized by N–P bonds serving as trap sites to capture electrons, as seen in Fig. 19c.

Carbon-based materials, intrinsically possessing good electrical conductivity and surface modifiability, have been extensively used as electron transfer media, acceptors and storage centers,[39] achieving the goals of accelerating the separation of photo-excited charge carriers on g-C₃N₄ and prolonging their lifetime. A range of carbon-species–g-C₃N₄ composites, including carbon spheres–g-C₃N₄,[161] graphene/graphene oxides (GO)/reduced graphene oxides (rGO)–g-C₃N₄,[142,163,179] carbon nanofibers–g-C₃N₄,[99] carbon nanotubes,[213] fullerene–g-C₃N₄,[84] carbon quantum dots–g-C₃N₄[107,214] and so on, have been created to give the excellent output of photocatalytic performances. Probing into the interfaces of these composites has illustrated the existing interactions, such as electrostatic interactions (van der Waals forces and hydrogen bonds) and covalent bonds. For example, Siang-Piao Chai *et al.*[142] changed the surface potential from negative to positive for g-C₃N₄ with a protonation modification, and then adopted an electrostatic and π–π stacking interaction between negatively charged GO and positively charged g-C₃N₄ to achieve the self-assembly process, followed by a surface reduction process to obtain the final rGO–g-C₃N₄ composite. As observed in Fig. 20b, the photo-excited electrons at the conduction band of g-C₃N₄ migrate to rGO through interfaces under visible light irradiation; *i.e.*, better charge transfer and separation of g-C₃N₄ can be realized by producing distinct and useful interfacial interactions. Through a LiOH assisted ball-milling process of g-C₃N₄ and C₆₀, Shangfeng Yang *et al.*[84] engineered a C₆₀–g-C₃N₄ composite with covalent N–C₆₀ bonds existing at the interfaces, which was confirmed by N 1s high-resolution spectra of pure g-C₃N₄ and the C₆₀–g-C₃N₄ composite. Compared with pure g-C₃N₄, a new peak at 399.5 eV for the N

This journal is © the Partner Organisations 2020
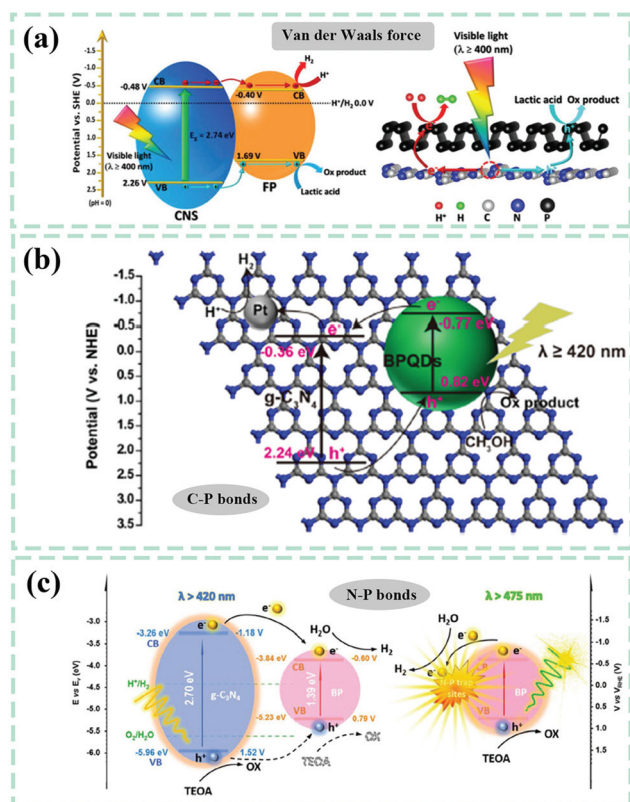
Inorg. Chem. Front., 2020, **7**, 4754–4793 | **4775**

Fig. 19 (a) The separation and transfer mechanism of photogenerated charge carriers over a phosphorene–g-C_3N_4 van der Waals heterojunction. Reproduced from ref. 80 with permission from Wiley-VCH, Copyright 2018. (b) Possible catalytic mechanism of the black phosphorus quantum dots (BPQDs)–g-C_3N_4 composite. Reproduced from ref. 120 with permission from Elsevier, Copyright 2018. (c) Proposed photocatalytic mechanism of the black phosphorus nanosheets–g-C_3N_4 composite. Reproduced from ref. 119 with permission from Wiley-VCH, Copyright 2019.

1s spectrum of the C_{60}–g-C_3N_4 composite (Fig. 20c) was assigned to N–C_{60} bonds connecting C_{60} and g-C_3N_4. In a photocatalytic H_2 evolution experiment, the authors added eosin Y (EY) to the C_{60}–g-C_3N_4 reaction system as a photosensitizer. When exposed to visible light, the excited electrons of EY would transfer to the conduction band of g-C_3N_4 and then reach C_{60} through the formed N–C_{60} bonds (Fig. 20d). The resulting effective charge transfer and separation reasonably endowed the C_{60}–g-C_3N_4 composite with a good photocatalytic activity of 266 μmol h^{-1} g^{-1}. Besides, some other chemical bonds interconnected g-C_3N_4 with carbon-based species, such as C–N–C,[99] C–O–C,[179,214] were also demonstrated, resulting in similar charge carrier behaviors for much improved catalytic properties.

In comparison to pristine g-C_3N_4, metal–organic frameworks–g-C_3N_4 composites produced broadened light adsorption ranges, effective photogenerated charge carrier charge and separation, giving rise to better catalytic performances.[137,164,215,216] However, based on the surface complexity and modification of metal–organic frameworks as well as g-C_3N_4, it is hard to determine the interfacial interactions between the two phases. To date, we have not found any clear proposal about the interfacial interactions of metal–organic frameworks–g-C_3N_4 composites. Whether there are electrostatic interactions or chemical bonds, we hope it will be figured out with the advancement of characterization techniques.

4.2. Multi-phase interfaces

When some drawbacks related to the band structures and charge carrier behaviors in constructing two-phase interfaces can be further optimized and fixed, researchers will find a way to implement it by introducing other phases for building multi-phase interfaces. The most complicated interface system

Fig. 20 (a) Zeta potential values of GO, g-C_3N_4 and protonated g-C_3N_4 (pCN); (b) photocatalytic mechanism of charge-carrier transfer and separation over rGO–pCN composite. Reproduced from ref. 142 with permission from Elsevier, Copyright 2015. (c) N 1s high-resolution spectra of pristine g-C_3N_4 and the C_{60}–g-C_3N_4 composite. (d) The proposed catalytic mechanism for the C_{60}–g-C_3N_4 composite photocatalyst. Reproduced from ref. 84 with permission from the Royal Society of Chemistry, Copyright 2017.

involving with g-C$_3$N$_4$-based composites contains four kinds of phase components. By making use of permutation and combination theory, we can understand the multiple possibilities of the ultimately formed interfaces. In this case, it is an extremely tough job to controllably synthesize the four-phase g-C$_3$N$_4$ composites with specific and well-defined interface systems. We are for the idea that the photocatalytic performances of g-C$_3$N$_4$-based composites are completely different, even if they

have the same components but diverse combined interface patterns, as the differences in the interfacial combination would bring about divergent photo-excited charge carrier behaviors. Therefore, herein, we mainly concentrate on the generated interfaces of g-C$_3$N$_4$-based composites from three phases.

For three-phase interfaces, the possible interfacial combinations are listed in Fig. 21. As shown in Fig. 21a, taking any given phase as a bridge to link with the other two components,
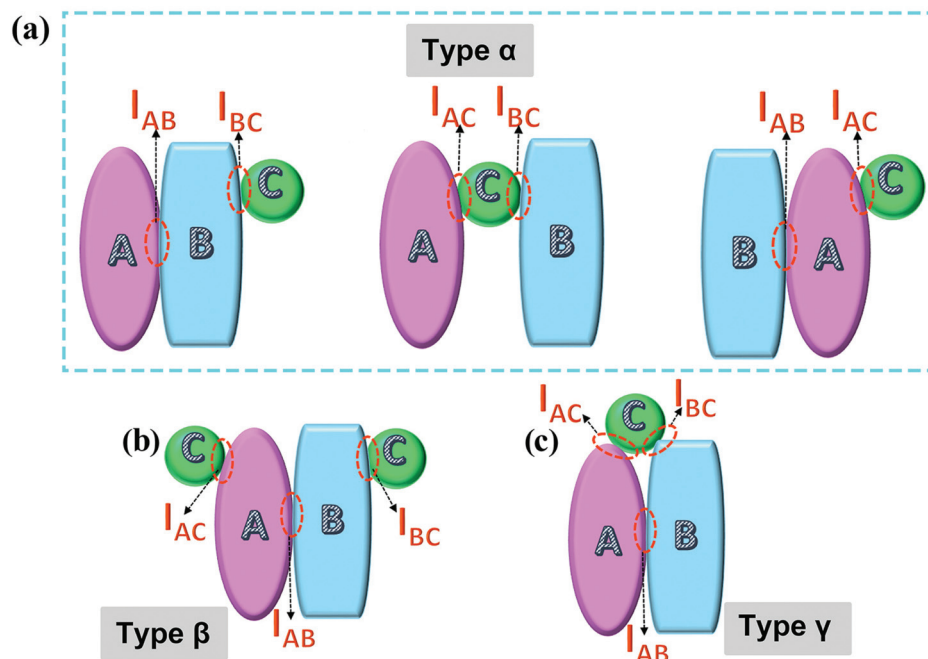

Fig. 21 Graphical illustration of possible interfacial combinations for three-phase g-C$_3$N$_4$-based composites. (a) A given phase as a bridge to interconnect two other components, here I_{AB} means the interface formed by A and B. (b) A representative picture where the two given phases of A and B are in contact, and the final phase C is attached to A and B, respectively. (c) A representative picture where the two given phases of A and B are in contact, and the final phase C is simultaneously attached to A and B.

Fig. 22 (a) SEM image of the Ag@g-C$_3$N$_4$@BiVO$_4$ ternary composite, and illustration photocatalytic mechanism of the charge-carrier transfer and separation over the Ag@g-C$_3$N$_4$@BiVO$_4$ ternary composite under visible light irradiation. Reproduced from ref. 217 with permission from Elsevier, Copyright 2016. (b) TEM image of the WO$_3$–g-C$_3$N$_4$–Bi$_2$O$_3$ nanocomposite and possible catalytic mechanisms for the WO$_3$–g-C$_3$N$_4$–Bi$_2$O$_3$ composite photocatalyst. Reproduced from ref. 65 with permission from Elsevier, Copyright 2018. (c) TEM image of the O–g-C$_3$N$_4$/graphene oxide/N–carbon nanotube (O–g-C$_3$N$_4$/GO/N–CNT) composite photocatalyst and electron transfer mechanism for the photo-degradation of organic pollutants over the O–g-C$_3$N$_4$/GO/N–CNT composite. Reproduced from ref. 218 with permission from the American Chemical Society, Copyright 2018. (d) TEM image of the Au–TiO$_2$–g-C$_3$N$_4$ composite and a scheme showing charge carrier pathways under vis/UV light irradiation. Reproduced from ref. 63 with permission from Wiley-VCH, Copyright 2018.

This journal is © the Partner Organisations 2020

Inorg. Chem. Front., 2020, **7**, 4754–4793 | **4777**

Table 3 Summary of interfacial types, functions, and photocatalytic performances of some typical g-C$_3$N$_4$-based photocatalysts

Interfacial classification	Specific composite name	Experimental conditions of hydrogen production	Hydrogen production rate	Interfacial atomic structure	The functions of interfaces	Associated with a demonstration by calculations (yes/no)	Ref.
Two-phase interfaces							
Noble-metallic species–g-C$_3$N$_4$	Au–g-C$_3$N$_4$	Sacrificial agent: triethanolamine (TEOA); Cocatalysts: Au; 150 W Hg-lamp; Solar light 21.1 mW cm^{-2}	324 µmol h^{-1} g^{-1}	Not clearly identified	Boosting charge separation; a plasmonic promoter	No	226
	Ag–g-C$_3$N$_4$	Sacrificial agent: TEOA; Cocatalysts: Ag; 300 W Xe-lamp; λ ≥ 420 nm	344.51 µmol h^{-1} g^{-1}	Not clearly identified	Boosting charge separation; SPR effect	No	125
	Pt–g-C$_3$N$_4$	Sacrificial agent: TEOA; Cocatalysts: Pt; 350 W Xe-lamp; λ ≥ 400 nm	588 µmol h^{-1} g^{-1}	Not clearly identified	Boosting charge separation; providing active sites	No	192
Oxides/chalcogenides–g-C$_3$N$_4$	WO$_3$–g-C$_3$N$_4$	Sacrificial agent: TEOA; Cocatalysts: Pt; 300 W Xe-lamp; Simulated solar light	3120 µmol h^{-1} g^{-1}	N–O–W bonding	Efficient charge transfer through the interface	Yes	103
	NiO–g-C$_3$N$_4$	Sacrificial agent: TEOA; Cocatalysts: NiO; 300 W Xe-lamp; λ ≥ 420 nm	68.8 µmol h^{-1} g^{-1}	C–O–Ni bonding	Efficient separation of hole–electron; improving charge transfer	No	98
	MoS$_2$–g-C$_3$N$_4$	Sacrificial agent: TEOA; Cocatalysts: MoS$_2$; 300 W Xe-lamp; λ ≥ 400 nm	1841.72 µmol h^{-1} g^{-1}	Not clearly identified	Boosting charge separation; providing active sites	No	4
Carbides/nitrides/borides/phosphides–g-C$_3$N$_4$	Ni$_3$C-g-C$_3$N$_4$	Sacrificial agent: TEOA; Cocatalysts: Ni$_3$C; 350 W Xe-lamp; λ ≥ 420 nm	303.6 µmol h^{-1} g^{-1}	Not clearly identified	Promoting charge-carrier separation	No	96
	Ni$_3$N-g-C$_3$N$_4$	Sacrificial agent: TEOA; Cocatalysts: Ni$_3$N; 300 W Xe-lamp; λ ≥ 420 nm	305.4 µmol h^{-1} g^{-1}	Not clearly identified	Facilitating electron–hole pairs separation	No	199
	NiB-g-C$_3$N$_4$	Sacrificial agent: TEOA; Cocatalysts: NiB; 300 W Xe-lamp; Optical filter AM1.5	464.4 µmol h^{-1} g^{-1}	B–Ni–N bonding	Boosting charge separation and transfer through interface bonding	No	201

4778 | *Inorg. Chem. Front.*, 2020, **7**, 4754–4793

This journal is © the Partner Organisations 2020

Table 3 (*Contd.*)

Interfacial classification	Specific composite name	Experimental conditions of hydrogen production	Hydrogen production rate	Interfacial atomic structure	The functions of interfaces	Associated with a demonstration by calculations (yes/no)	Ref.
	CoP–g-C$_3$N$_4$	Sacrificial agent: TEOA Cocatalysts: CoP 300 W Xe-lamp $\lambda \geq 420$ nm	1924 µmol h^{-1} g^{-1}	P–Co–N bonding	Boosting charge carriers separation; providing active sites	No	183
Perovskites/halides–g-C$_3$N$_4$	Ca$_2$Nb$_2$TaO$_{10}$–g-C$_3$N$_4$	Sacrificial agent: TEOA Cocatalysts: Pt 300 W Xe-lamp $\lambda \geq 400$ nm	870.8 µmol h^{-1} g^{-1}	Not clearly identified	Boosting charge carriers separation	No	69
	SrTiO$_3$–g-C$_3$N$_4$	Sacrificial agent: TEOA Cocatalysts: Pt 300 W Xe-lamp $\lambda \geq 420$ nm	966.8 µmol h^{-1} g^{-1}	Not clearly identified	Highly-efficient electron separation	Yes	38
	Bi$_4$NbO$_8$Cl–g-C$_3$N$_4$	Sacrificial agent: lactic acid Cocatalysts: Pt 300 W Xe-lamp $\lambda \geq 420$ nm	287.7 µmol h^{-1} g^{-1}	Not clearly identified	Improving charge carriers separation and transfer	No	66
Salt compounds–g-C$_3$N$_4$	Bi$_2$MoO$_6$–g-C$_3$N$_4$	Sacrificial agent: TEOA Cocatalysts: Pt 300 W Xe-lamp $\lambda \geq 420$ nm	563.4 µmol h^{-1} g^{-1}	Not clearly identified	Improving the separation efficiency of electron–holes pairs	No	157
Black phosphorus relatives/organics related species–g-C$_3$N$_4$	P–g-C$_3$N$_4$	Sacrificial agent: methanol Cocatalysts: P Xe-lamp $\lambda \geq 420$ nm	427 µmol h^{-1} g^{-1}	P–N bonding	Efficient charge transfer	No	118
	P–g-C$_3$N$_4$	Sacrificial agent: methanol Cocatalysts: Pt 300 W Xe-lamp $\lambda \geq 420$ nm	271 µmol h^{-1} g^{-1}	P–C bonding	Efficient charge separation at interfaces	No	120
	C–g-C$_3$N$_4$	Sacrificial agent: TEOA Cocatalysts: not mentioned 300 W Xe-lamp $\lambda \geq 420$ nm	16 885 µmol h^{-1} g^{-1}	C–N–C bonding	Boosting charge separation; facilitating electron transfer	No	99
Multi-phase interfaces	Ag/CQDs–g-C$_3$N$_4$	Sacrificial agent: TEOA Cocatalysts: not mentioned 300 W Xe-lamp	626.93 µmol h^{-1} g^{-1}	Not clearly identified	Boosting high-efficiency photoelectrons generation, transfer and separation	No	173

Table 3 (Contd.)

Interfacial classification	Specific composite name	Experimental conditions of hydrogen production	Hydrogen production rate	Interfacial atomic structure	The functions of interfaces	Associated with a demonstration by calculations (yes/no)	Ref.
	CdS–Cu$_7$S$_4$/g-C$_3$N$_4$	$\lambda \geq 420$ nm Sacrificial agent: Na$_2$S/Na$_2$SO$_3$ Cocatalysts: no 300 W Xe-lamp	1930 μmol g^{-1} h^{-1}	Not clearly identified	Promoting spatial separation of carriers	No	141
	C/NiS–g-C$_3$N$_4$	$\lambda \geq 420$ nm Sacrificial agent: TEOA Cocatalysts: not mentioned 300 W Xe-lamp	366.4 μmol g^{-1} h^{-1}	Not clearly identified	Boosting charge transfer and separation	No	227
	Au/SnO$_2$–g-C$_3$N$_4$	Sacrificial agent: methanol Cocatalysts: no 100 W LED-lamp $\lambda \geq 400$ nm	770 μmol g^{-1} h^{-1}	Not clearly identified	Promoting charge separation	No	72
	NiS/CdS–g-C$_3$N$_4$	Sacrificial agent: TEOA Cocatalysts: NiS 300 W Xe-lamp $\lambda \geq 420$ nm	2563 μmol g^{-1} h^{-1}	Not clearly identified	Improving electron–hole pairs separation	No	228

there are three kinds of interfaces. If any given two phases are bonded, the third phase attaches to the two phases respectively, generating another three types of interface combination. Fig. 21b is just one case of the three. However, if the third phase is connected with the two phases simultaneously, a new kind of interface is created. As we understand it, the photo-excited charge carriers would behave completely differently for the diverse interfacial combinations of the three-phase g-C$_3$N$_4$-based composites. This calls for us to exactly figure out the interfacial contact types, to give a convincing photocatalytic mechanism combined with structural characterizations and performance tests.

Qi Yang et al.[217] employed a photo-reduction method to fabricate a ternary Ag@g-C$_3$N$_4$@BiVO$_4$ composite. In a typical synthetic process, the prefabricated BiVO$_4$–g-C$_3$N$_4$ composite was mixed with AgNO$_3$ solution. Under visible light irradiation, the excited electrons of g-C$_3$N$_4$ would move to the conduction band of BiVO$_4$ so that the majority of Ag$^+$ ions are reduced as Ag nanoparticles on the surface of BiVO$_4$, as shown in Fig. 22a. The Ag$^+$ ions would have a chance to grow as a bridge for linking g-C$_3$N$_4$ and BiVO$_4$, but it is limited. This means an orthodox "Type α" interfacial combination may not be formed. On the other hand, the surface plasmon resonance (SPR) effects of Ag nanoparticles should also play a role in photocatalytic reactions, similar to the as-reported Ag–carbon quantum dots–g-C$_3$N$_4$ systems.[173,176] As displayed in Fig. 22b, a three-phase "Type α" interfacial combination was achieved as both WO$_3$ and Bi$_2$O$_3$ are distributed on g-C$_3$N$_4$.[65] As a result, the excited electrons of WO$_3$ and Bi$_2$O$_3$ migrated to the valence band of g-C$_3$N$_4$, giving rise to dual Z-scheme charge transfer and better catalytic performance for tetracycline hydrochloride degradation. Fig. 22c indicates a three-phase "Type γ" interfacial combination made up of oxygen-modified g-C$_3$N$_4$ (O–g-C$_3$N$_4$), graphene oxide (GO) and nitrogen-doped carbon nanotubes (N–CNT), which was designed and developed for facilitating the transfer and separation of photogenerated charge carriers and inhibiting the recombination of electron–hole pairs, so the pollutants could be effectively eliminated.[218] A ternary Au–TiO$_2$–g-C$_3$N$_4$ composite system (Fig. 22d) was fabricated by Valérie Keller et al.,[63] which corresponded to the "Type β" interfacial combination. It was found that Au nanoparticles were simultaneously deposited on g-C$_3$N$_4$ and TiO$_2$, while TiO$_2$ nanoparticles were fixed in g-C$_3$N$_4$ substances as well. The authors claimed that the deposited Au nanoparticles acted as co-catalysts and shuttles to collect electrons. Even the transferred electrons from g-C$_3$N$_4$ to TiO$_2$ by the photo-excitation of g-C$_3$N$_4$ enabled migration to Au nanoparticles, leading to a much improved effective charge utilization.

Fortunately and exhilaratingly, two-phase and multi-phase interface engineering have been used to create g-C$_3$N$_4$-based composites with much enhanced photocatalytic performances (Table 3). Borrowing from the advantages of other nanostructures or compensating for individual weaknesses, g-C$_3$N$_4$-based composites, in a broad sense, are capable of achieving a series of benefits, such as boosted light-harvesting ability, the improved migration and separation of photogenerated charge

4780 | *Inorg. Chem. Front.*, 2020, **7**, 4754–4793

This journal is © the Partner Organisations 2020

carriers and the depressed recombination of photo-excited electron–hole pairs.[219–221] We should be aware of that the interfaces are essentially the triggers to give these beneficial shots. In this regard, the establishment of the photogenerated charge mechanism over g-C$_3$N$_4$-based composites should be derived from a combined analysis of the structural and composite characterization, photoelectrochemical spectral characterization and catalytic performance measurements. Of these, we believe that the structural and composite characterizations are the most fundamental and significant issues. It is meaningless to illustrate the charge behaviors depending only on the corresponding photoelectrochemistry and catalytic perform-

ance measurements against the contained components' spatial distribution states and interfacial contact types. This should receive more attention in future research. Other problems include the fact that we still have no idea how the charges transfer from one catalyst to another through the interfaces, the transport medium needs to be determined, along with predictions of carrier migration based on some acknowledged rules. We herein appeal to researchers to concentrate on the microscopic determination of interfacial chemical interactions, such as specific chemical bonds and the types of electrostatic interactions, instead of just stating the indistinct interface contact, and believe it will help a lot in
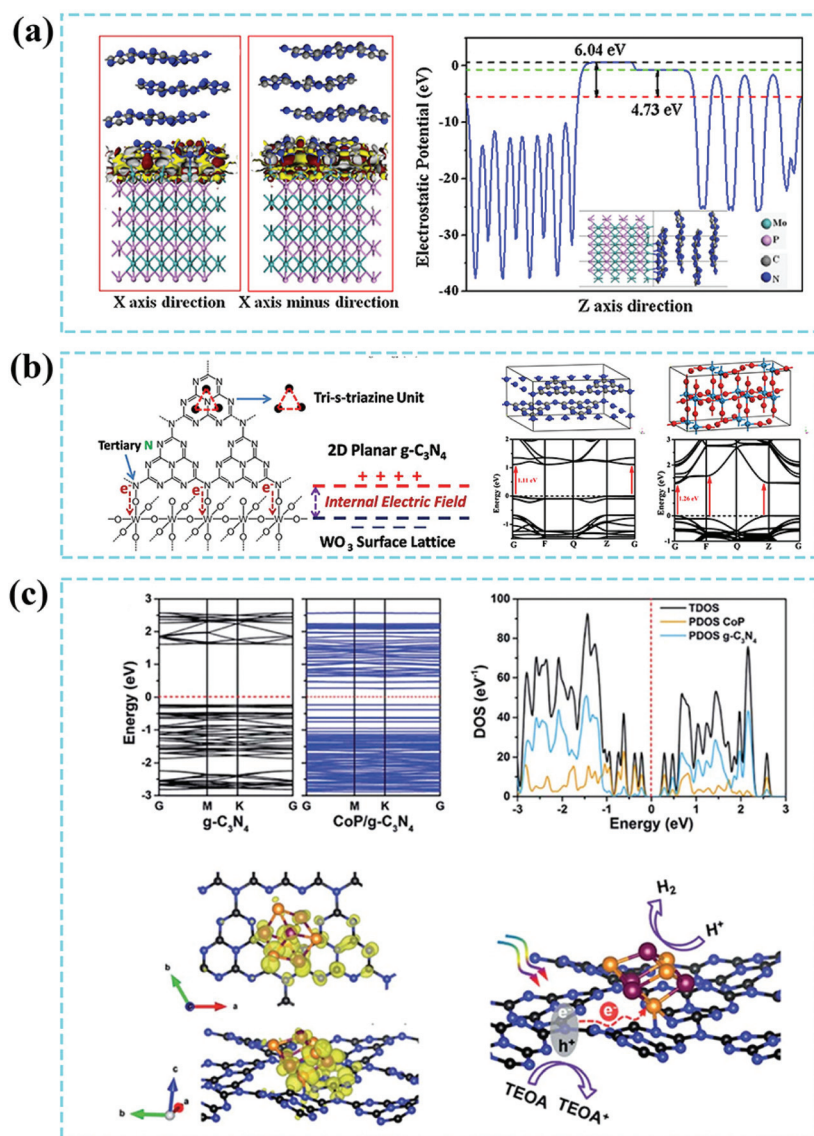

Fig. 23 (a) Three-dimensional charge density difference model and calculated electrostatic potentials of the as-developed MoP (0 0 1)−g-C$_3$N$_4$ (0 0 1) composite. Reproduced from ref. 111 with permission from Elsevier, Copyright 2018. (b) Interfacial atomic illustration of the as-synthesized WO$_3$−g-C$_3$N$_4$ composite, crystal structures and calculated electronic band structures of pure g-C$_3$N$_4$ and WO$_3$. Reproduced from ref. 103 with permission from Elsevier, Copyright 2017. (c) DFT-calculated band structures of pure g-C$_3$N$_4$ and the CoP−g-C$_3$N$_4$ composite, density of states (DoS) and constructed heterointerface model of the CoP−g-C$_3$N$_4$ composite. Reproduced from ref. 75 with permission from the American Chemical Society, Copyright 2019.

This journal is © the Partner Organisations 2020

Inorg. Chem. Front., 2020, **7**, 4754–4793 | **4781**

the development of high-performance g-C$_3$N$_4$-based composite catalysts.

4.3.   Theoretical analysis of the interfaces

The combination of theory with practice allows a better understanding of scientific issues. Herein, theoretical calculations related to the interfacial carrier behaviors of g-C$_3$N$_4$-based composite photocatalysts play a significant role in the design of material interfaces and the comprehension of photocatalytic mechanisms. This mainly focuses on the calculations by density functional theory (DFT) and not the band structure calculations by using as-measured UV–vis diffuse reflectance spectra.

After consulting many literature reports, we have found that there are only a small fraction of reports that contain theoretical calculations for g-C$_3$N$_4$-based composite photocatalysts as compared with the database, taking P–g-C$_3$N$_4$,[121] MoP–g-C$_3$N$_4$,[111] CoP–g-C$_3$N$_4$,[75] CoS$_x$–g-C$_3$N$_4$,[152] WS$_2$–g-C$_3$N$_4$,[222] InSe–g-C$_3$N$_4$,[223] WO$_3$–g-C$_3$N$_4$,[103] TiO$_2$–g-C$_3$N$_4$,[101] MnO$_2$–g-C$_3$N$_4$,[181] SrTiO$_3$–g-C$_3$N$_4$,[38] BiPO$_4$–g-C$_3$N$_4$,[224] Bi$_2$WO$_6$–g-C$_3$N$_4$,[225] Bi$_4$Ti$_3$O$_{12}$–g-C$_3$N$_4$,[87] and so on, as research objects. We divided the research into three levels. The first involves separately calculating the two involved components to reveal the Fermi level and charge/electron behaviors, without disclosing the interfacial space and chemical structures. For example, Zhou et al.[111] employed the MoP–g-C$_3$N$_4$ heterojunction as a research object (Fig. 23a). By supposing the interface region is MoP (001) and g-C$_3$N$_4$ (001), DFT calculation results showed that the Fermi levels of g-C$_3$N$_4$ and MoP were 4.73 eV and 6.04 eV, respectively. Hence, the electron will be transferred from g-C$_3$N$_4$ to MoP. The problem is the experimental evidence to prove that the contact between MoP (001) and g-C$_3$N$_4$ (001) is not sufficient, which may make the calculation not convincing. Still, we have no idea about the electron transfer details, on an atomic scale. The second level involves demonstrating the interfacial space and chemical structures of g-C$_3$N$_4$-based photocatalysts, still calculating the two components separately. Yu et al.[103] confirmed the N–O–W bonding at the interfaces of WO$_3$–g-C$_3$N$_4$ by means of multiple characterization techniques (Fig. 23b). The authors proposed that the interfacial electrons were transferred from WO$_3$ to g-C$_3$N$_4$, according to monophasic electronic band structure calculations. The third level involves implementing DFT calculations in terms of an exact model with experimental evidence, then analyzing carrier behaviors over the determined interfacial structure. As seen in Fig. 23c, it was determined that P–N bonding existed at the interfaces of CoP and g-C$_3$N$_4$.[75] Then, the authors established a hetero-interface model between CoP and g-C$_3$N$_4$. By using DFT calculations, they demonstrated that the charges would redistribute at the interface region, and the electrons would transfer from the N sites of g-C$_3$N$_4$ to the P sites of CoP through N–P bonding. We believe such results are more convincing; that is, theoretical calculations are much closer to experimental facts.

Theoretical calculations can make predictions to guide experimental directions but in most cases, they should be based on experimental details. From our perspective, the calculations based on wrong or unreasonable models are meaningless, which means the prerequisites for researchers to construct a calculating model include figuring out the phase combination, the special contact model, and the chemical structure pattern on the atomic scale at the interfaces, as mentioned in section 3: "Techniques to identify the interfaces". Only in this way can the interface engineering design of g-C$_3$N$_4$-based composite photocatalysts be boosted to a new and prosperous stage. Herein, we highlight the positive role of theoretical calculations in understanding interfacial charge/electron transfer. Also, we advocate that the calculation model should be precisely constructed in line with the as-demonstrated pinpointing phase components and interfacial chemical structures. In this regard, researchers should pay close attention to the physicochemical characterization, to illustrate the material interface as clearly as possible.

5.   Conclusions and perspectives

Over the past five years, the progress devoted to developing g-C$_3$N$_4$-based hybrid nanostructures has laid a solid base for knowledge on photocatalytic applications. To date, the consensus that interface engineering is one of the most promising strategies for synthesizing g-C$_3$N$_4$-based nanocomposites has been made, considering the designability and effectiveness. It has been demonstrated that interfaces can be naturally generated along with the process of coupling g-C$_3$N$_4$ with other phases, which equips the as-obtained nanocomposites with several significant advantages as follows: (1) boosted light-harvesting ability;[66,102,116] (2) accelerated charge carrier transfer and separation through interfaces;[83,119,151] (3) depressed recombination rate of photoinduced electron–hole pairs, as well as prolonged carrier lifetime;[87] (4) the satisfactory durability[129] induced by the intimate interface contact. It can be concluded, based on numerous published research results, that all the benefits are can be achieved depending on or keeping a close relationship with the formed interfaces. Considering previous works, we have to admit that the emphasis is always placed on the role of interfaces in enhancing the photocatalytic performances but at a macroscopic and unclear level. In general, integrating g-C$_3$N$_4$ with other bandgap matched phases would drive the movement of photogenerated carriers. To gain in-depth insight into the precise roles and functions of interfaces, more attempts need to be made.

Firstly, the current mainstream synthetic methods for g-C$_3$N$_4$-based nanocomposites with interface contact are composed of solid- and liquid-based strategies, on account of the differences in reactive media and conditions. Solid-state-synthesis methods are deficient in the designability and controllability of the interfaces, even though they generally guarantee the formation of interfaces and show better photocatalytic activities than the pure phase. In contrast, the synthesis of high-performance g-C$_3$N$_4$-based nanocomposites with devisable and controllable interfaces in liquids is more controllable,

4782 | *Inorg. Chem. Front.*, 2020, **7**, 4754–4793

This journal is © the Partner Organisations 2020

taking advantage of its strippability and surficial modifiability. Hence, different phases can be intimately attached to g-C$_3$N$_4$ through electrostatic interactions, possibly producing chemical bonds in the reaction processes. Given the fact that the interfaces are favorable in most cases, methods such as chemical vapor deposition, which can controllably engineer more interfaces with specific and detectable chemical structures, are much more promising and desirable and should receive intensive attention in the future.

Secondly, many reports talk about interfaces but the corresponding structural and composite characterizations are not specific enough to convince us and to support the photocatalytic mechanism. We already have some knowledge about the interfaces during the design period but far is required. We cannot be satisfied with just knowing the spatial distribution states at the hetero-interfaces of nanostructures and imagining the interfacial atomic arrangement patterns. The chemical structures and interactions at the interfaces should be expounded much more precisely. We should not be limited to traditional characterization techniques, such as SEM, TEM, XRD, FTIR, Raman and XPS; more advanced techniques related to the identification of interfacial interactions should be employed, such as spherical aberration-corrected TEM and synchrotron radiation-based X-ray absorption spectroscopy (XAS), to name a few.

Thirdly, a comprehensive understanding and significant achievements with respect to the roles of interfaces in g-C$_3$N$_4$-based composite photocatalysts have been acquired to date. By coupling other band structures and well-matched nanostructures with g-C$_3$N$_4$, effective carrier transfer and migration can be realized *via* the intimate interfacial contact, which can be further confirmed by the corresponding spectroscopy measurements, band position calculations and active species trapping experiments. However, all of these are understood on a macroscopic level. We are still blind to why and how the carriers could behave in that positive manner. To push research on g-C$_3$N$_4$-based composite photocatalysts into a completely new and higher stage, we appeal to researchers to put more focus on the roles and functions of interfaces on the atomic/molecular scale in the future. Based on the determined interfacial chemical structures and DFT theoretical calculations modeled by precise hetero-interface crystal structures, we can predict and understand the photo-induced electron transfer from the atomic sites of one phase to the atomic sites of another phase, instead just knowing it occurs from one component to another component.

Methods for fabricating interfaces and techniques for identifying interfaces are conducive to knowing what they actually are. The proposed photocatalytic mechanisms for the g-C$_3$N$_4$-based composites stem from the precise interfacial structure identification, performance testing and practical theoretical calculations. Only in this way can we cause the charge carrier behavior to coincide with the true condition. Unfortunately, the overwhelming majority of current reports on g-C$_3$N$_4$-based composite photocatalysts do not show us the atomic pattern and chemical structure at interfaces, let alone implement DFT calculations to reveal the roles and functions of interfaces. Benefiting from the rapid development of experimental science, researchers have accumulated more and more experience and understanding of material interface chemistry; however, there is currently little research on determining the roles and functions of interface structures on the atomic scale. Therefore, we propose that future research on the interface engineering of g-C$_3$N$_4$-based catalysts should address three sections, namely, methods for forming specific interfaces, advanced techniques for precisely characterizing the interface, and deep understanding of the roles and functions of the interface chemical structure, preferably combined with pinpointing theoretical calculations.

Conflicts of interest

There are no conflicts to declare.

Acknowledgements

References

1 X. Dong and F. Cheng, Recent development in exfoliated two-dimensional g-C$_3$N$_4$ nanosheets for photocatalytic applications, *J. Mater. Chem. A*, 2015, **3**, 23642–23652.

2 Y. Zheng, L. Lin, B. Wang and X. Wang, Graphitic Carbon Nitride Polymers toward Sustainable Photoredox Catalysis, *Angew. Chem., Int. Ed.*, 2015, **54**, 12868–12884.

3 S. Yin, J. Han, T. Zhou and R. Xu, Recent progress in g-C$_3$N$_4$ based low cost photocatalytic system: activity enhancement and emerging applications, *Catal. Sci. Technol.*, 2015, **5**, 5048–5061.

4 H. Xu, J. Yi, X. She, Q. Liu, L. Song, S. Chen, Y. Yang, Y. Song, R. Vajtai, J. Lou, H. Li, S. Yuan, J. Wu and P. M. Ajayan, 2D heterostructure comprised of metallic 1T-MoS$_2$/Monolayer O-g-C$_3$N$_4$ towards efficient photocatalytic hydrogen evolution, *Appl. Catal., B*, 2018, **220**, 379–385.

5 L. Yao, D. Wei, Y. Ni, D. Yan and C. Hu, Surface localization of CdZnS quantum dots onto 2D g-C$_3$N$_4$ ultrathin microribbons: Highly efficient visible light-induced H$_2$-generation, *Nano Energy*, 2016, **26**, 248–256.

6 P. Tan, A. Zhu, Y. Liu, Y. Ma, W. Liu, H. Cui and J. Pan, Insights into the efficient charge separation and transfer efficiency of La,Cr-codoped SrTiO$_3$ modified with CoP as a noble-metal-free co-catalyst for superior visible-light driven photocatalytic hydrogen generation, *Inorg. Chem. Front.*, 2018, **5**, 679–686.

7 M. Li, L. Zhang, M. Wu, Y. Du, X. Fan, M. Wang, L. Zhang, Q. Kong and J. Shi, Mesostructured CeO$_2$/g-C$_3$N$_4$ nanocomposites: Remarkably enhanced photocatalytic activity

This journal is © the Partner Organisations 2020

Inorg. Chem. Front., 2020, **7**, 4754–4793 | **4783**

for CO$_2$ reduction by mutual component activations, *Nano Energy*, 2016, **19**, 145–155.

8 T. Di, B. Zhu, B. Cheng, J. Yu and J. Xu, A direct Z-scheme g-C$_3$N$_4$/SnS$_2$ photocatalyst with superior visible-light CO$_2$ reduction performance, *J. Catal.*, 2017, **352**, 532–541.

9 F. Raziq, Y. Qu, M. Humayun, A. Zada, H. Yu and L. Jing, Synthesis of SnO$_2$/B-P codoped g-C$_3$N$_4$ nanocomposites as efficient cocatalyst-free visible-light photocatalysts for CO$_2$ conversion and pollutant degradation, *Appl. Catal., B*, 2017, **201**, 486–494.

10 P. Tan, X. Chen, L. Wu, Y. Y. Shang, W. Liu, J. Pan and X. Xiong, Hierarchical flower-like SnSe$_2$ supported Ag$_3$PO$_4$ nanoparticles: Towards visible light driven photocatalyst with enhanced performance, *Appl. Catal., B*, 2017, **202**, 326–334.

11 Y. Shang, X. Chen, W. Liu, P. Tan, H. Chen, L. Wu, C. Ma, X. Xiong and J. Pan, Photocorrosion inhibition and high-efficiency photoactivity of porous g-C$_3$N$_4$/Ag$_2$CrO$_4$ composites by simple microemulsion-assisted co-precipitation method, *Appl. Catal., B*, 2017, **204**, 78–88.

12 Y. Ma, Y. Bian, P. Tan, Y. Shang, Y. Liu, L. Wu, A. Zhu, W. Liu, X. Xiong and J. Pan, Simple and facile ultrasound-assisted fabrication of Bi$_2$O$_2$CO$_3$/g-C$_3$N$_4$ composites with excellent photoactivity, *J. Colloid Interface Sci.*, 2017, **497**, 144–154.

13 Y. Li, X. Liu, L. Tan, Z. Cui, D. Jing, X. Yang, Y. Liang, Z. Li, S. Zhu, Y. Zheng, K. W. K. Yeung, D. Zheng, X. Wang and S. Wu, Eradicating Multidrug–Resistant Bacteria Rapidly Using a Multi Functional g-C$_3$N$_4$@ Bi$_2$S$_3$ Nanorod Heterojunction with or without Antibiotics, *Adv. Funct. Mater.*, 2019, **29**, 1900946.

14 S. Vignesh, S. Suganthi, J. Kalyana Sundar and V. Raj, Construction of α-Fe$_2$O$_3$/CeO$_2$ decorated g-C$_3$N$_4$ nanosheets for magnetically separable efficient photocatalytic performance under visible light exposure and bacterial disinfection, *Appl. Surf. Sci.*, 2019, **488**, 763–777.

15 A. H. Fujishima and K. Honda, Electrochemical Photolysis of Water at a Semiconductor Electrode, *Nature*, 1972, **238**, 37–38.

16 J. Carey, J. Lawrence and H. Tosine, Photodechlorination of PCB's in the Presence of Titanium Dioxide in Aqueous Suspensions, *Bull. Environ. Contam. Toxicol.*, 1976, **16**, 697–701.

17 T. Inoue, A. Fujishima, S. Konishi and K. Honda, Photoelectrocatalytic Reduction of Carbon Dioxide in Aqueous Suspensions of Semiconductor Powders, *Nature*, 1979, **277**, 637–638.

18 L. Jiang, X. Yuan, Y. Pan, J. Liang, G. Zeng, Z. Wu and H. Wang, Doping of graphitic carbon nitride for photocatalysis: A reveiw, *Appl. Catal., B*, 2017, **217**, 388–406.

19 Y. Tachibana, L. Vayssieres and J. R. Durrant, Artificial photosynthesis for solar water-splitting, *Nat. Photonics*, 2012, **6**, 511–518.

20 S. Cao, J. Low, J. Yu and M. Jaroniec, Polymeric photocatalysts based on graphitic carbon nitride, *Adv. Mater.*, 2015, **27**, 2150–2176.

21 J. Wen, J. Xie, X. Chen and X. Li, A review on g-C$_3$N$_4$-based photocatalysts, *Appl. Surf. Sci.*, 2017, **391**, 72–123.

22 F. Ding, D. Yang, Z. Tong, Y. Nan, Y. Wang, X. Zou and Z. Jiang, Graphitic carbon nitride-based nanocomposites as visible-light driven photocatalysts for environmental purification, *Environ. Sci.: Nano*, 2017, **4**, 1455–1469.

23 G. Mamba and A. K. Mishra, Graphitic carbon nitride (g-C$_3$N$_4$) nanocomposites: A new and exciting generation of visible light driven photocatalysts for environmental pollution remediation, *Appl. Catal., B*, 2016, **198**, 347–377.

24 X. Wang, K. Maeda, A. Thomas, K. Takanabe, G. Xin, J. M. Carlsson, K. Domen and M. Antonietti, A metal-free polymeric photocatalyst for hydrogen production from water under visible light, *Nat. Mater.*, 2009, **8**, 76–80.

25 J. Zhu, P. Xiao, H. Li and S. A. Carabineiro, Graphitic carbon nitride: synthesis, properties, and applications in catalysis, *ACS Appl. Mater. Interfaces*, 2014, **6**, 16449–16465.

26 L. Zeng, X. Ding, Z. Sun, W. Hua, W. Song, S. Liu and L. Huang, Enhancement of photocatalytic hydrogen evolution activity of g-C$_3$N$_4$ induced by structural distortion via post-fluorination treatment, *Appl. Catal., B*, 2018, **227**, 276–284.

27 H. Feng, Q. Guo, Y. Xu, T. Chen, Y. Zhou, Y. Wang, M. Wang and D. Shen, Surface Nonpolarization of g-C$_3$N$_4$ by Decoration with Sensitized Quantum Dots for Improved CO$_2$ Photoreduction, *ChemSusChem*, 2018, **11**, 4256–4261.

28 Y. Gao, F. Hou, S. Hu, B. Wu and B. Jiang, Synchronization iodine surface modification and lattice doping porous carbon nitride for photocatalytic hydrogen production, *Appl. Surf. Sci.*, 2019, **481**, 1089–1095.

29 Y. Shang, Y. Ma, X. Chen, X. Xiong and J. Pan, Effect of sodium doping on the structure and enhanced photocatalytic hydrogen evolution performance of graphitic carbon nitride, *Mol. Catal.*, 2017, **433**, 128–135.

30 C. Hu, M.-S. Wang, C.-H. Chen, Y.-R. Chen, P.-H. Huang and K.-L. Tung, Phosphorus-doped g-C$_3$N$_4$ integrated photocatalytic membrane reactor for wastewater treatment, *J. Membr. Sci.*, 2019, **580**, 1–11.

31 J. Huang, D. Li, R. Li, Q. Zhang, T. Chen, H. Liu, Y. Liu, W. Lv and G. Liu, An efficient metal-free phosphorus and oxygen co-doped g-C$_3$N$_4$ photocatalyst with enhanced visible light photocatalytic activity for the degradation of fluoroquinolone antibiotics, *Chem. Eng. J.*, 2019, **374**, 242–253.

32 Y. Jiang, Z. Sun, C. Tang, Y. Zhou, L. Zeng and L. Huang, Enhancement of photocatalytic hydrogen evolution activity of porous oxygen doped g-C$_3$N$_4$ with nitrogen defects induced by changing electron transition, *Appl. Catal., B*, 2019, **240**, 30–38.

33 Y. Wang, Y. Li, J. Zhao, J. Wang and Z. Li, g-C$_3$N$_4$/B doped g-C$_3$N$_4$ quantum dots heterojunction photocatalysts for hydrogen evolution under visible light, *Int. J. Hydrogen Energy*, 2019, **44**, 618–628.

34 D. Ruan, S. Kim, M. Fujitsuka and T. Majima, Defects rich g-C_3N_4 with mesoporous structure for efficient photocatalytic H_2 production under visible light irradiation, *Appl. Catal., B*, 2018, **238**, 638–646.

35 W. Lin, K. Lu, S. Zhou, J. Wang, F. Mu, Y. Wang, Y. Wu and Y. Kong, Defects remodeling of g-C_3N_4 nanosheets by fluorine-containing solvothermal treatment to enhance their photocatalytic activities, *Appl. Surf. Sci.*, 2019, **474**, 194–202.

36 Y.-N. Li, Z.-Y. Chen, M.-Q. Wang, L.-Z. Zhang and S.-J. Bao, Interface engineered construction of porous g-C_3N_4/TiO_2 heterostructure for enhanced photocatalysis of organic pollutants, *Appl. Surf. Sci.*, 2018, **440**, 229–236.

37 Y. Wang, G. Tan, T. Liu, Y. Su, H. Ren, X. Zhang, A. Xia, L. Lv and Y. Liu, Photocatalytic properties of the g-C_3N_4/{010} facets $BiVO_4$ interface Z-Scheme photocatalysts induced by $BiVO_4$ surface heterojunction, *Appl. Catal., B*, 2018, **234**, 37–49.

38 Y. Luo, B. Deng, Y. Pu, A. Liu, J. Wang, K. Ma, F. Gao, B. Gao, W. Zou and L. Dong, Interfacial coupling effects in g-C_3N_4/$SrTiO_3$ nanocomposites with enhanced H_2 evolution under visible light irradiation, *Appl. Catal., B*, 2019, **247**, 1–9.

39 T. Su, Q. Shao, Z. Qin, Z. Guo and Z. Wu, Role of Interfaces in Two-Dimensional Photocatalyst for Water Splitting, *ACS Catal.*, 2018, **8**, 2253–2276.

40 T. Kwon, M. Jun, J. Joo and K. Lee, Nanoscale hetero-interfaces between metals and metal compounds for electrocatalytic applications, *J. Mater. Chem. A*, 2019, **7**, 5090–5110.

41 W. J. Ong, L. L. Tan, Y. H. Ng, S. T. Yong and S. P. Chai, Graphitic Carbon Nitride (g-C_3N_4)-Based Photocatalysts for Artificial Photosynthesis and Environmental Remediation: Are We a Step Closer To Achieving Sustainability?, *Chem. Rev.*, 2016, **116**, 7159–7329.

42 F. Deng, L. Zhao, X. Pei, X. Luo and S. Luo, Facile in situ hydrothermal synthesis of g-C_3N_4/SnS_2 composites with excellent visible-light photocatalytic activity, *Mater. Chem. Phys.*, 2017, **189**, 169–175.

43 H. Wang, Y. Liang, L. Liu, J. Hu and W. Cui, Highly ordered TiO_2 nanotube arrays wrapped with g-C_3N_4 nanoparticles for efficient charge separation and increased photoelectrocatalytic degradation of phenol, *J. Hazard. Mater.*, 2018, **344**, 369–380.

44 H. Zhao, S. Sun, P. Jiang and Z. J. Xu, Graphitic C_3N_4 modified by Ni_2P cocatalyst: An efficient, robust and low cost photocatalyst for visible-light-driven H_2 evolution from water, *Chem. Eng. J.*, 2017, **315**, 296–303.

45 Z. Sun, M. Zhu, M. Fujitsuka, A. Wang, C. Shi and T. Majima, Phase Effect of Ni_xP_y Hybridized with g-C_3N_4 for Photocatalytic Hydrogen Generation, *ACS Appl. Mater. Interfaces*, 2017, **9**, 30583–30590.

46 D. Zeng, T. Zhou, W. J. Ong, M. Wu, X. Duan, W. Xu, Y. Chen, Y. A. Zhu and D. L. Peng, Sub-5 nm Ultra-Fine FeP Nanodots as Efficient Co-Catalysts Modified Porous g-C_3N_4 for Precious-Metal-Free Photocatalytic Hydrogen Evolution under Visible Light, *ACS Appl. Mater. Interfaces*, 2019, **11**, 5651–5660.

47 R. Shen, J. Xie, H. Zhang, A. Zhang, X. Chen and X. Li, Enhanced Solar Fuel H_2 Generation over g-C_3N_4 Nanosheet Photocatalysts by the Synergetic Effect of Noble Metal-Free Co_2P Cocatalyst and the Environmental Phosphorylation Strategy, *ACS Sustainable Chem. Eng.*, 2017, **6**, 816–826.

48 Y. Xu, S. Wang, J. Yang, B. Han, R. Nie, J. Wang, Y. Dong, X. Yu, J. Wang and H. Jing, Highly efficient photoelectrocatalytic reduction of CO_2 on the Ti_3C_2/g-C_3N_4 heterojunction with rich Ti^{3+} and pyri-N species, *J. Mater. Chem. A*, 2018, **6**, 15213–15220.

49 P. Ye, X. Liu, J. Iocozzia, Y. Yuan, L. Gu, G. Xu and Z. Lin, A highly stable non-noble metal Ni_2P co-catalyst for increased H_2 generation by g-C_3N_4 under visible light irradiation, *J. Mater. Chem. A*, 2017, **5**, 8493–8498.

50 Z. Peng, L. Jianping, T. Yonghua, C. Yuguang, L. Fei and G. Shaojun, Amorphous $FeCoPO_x$ nanowires coupled to g-C_3N_4 nanosheets with enhanced interfacial electronic transfer for boosting photocatalytic hydrogen production, *Appl. Catal., B*, 2018, **238**, 161–167.

51 X. Yang, L. Tian, X. Zhao, H. Tang, Q. Liu and G. Li, Interfacial optimization of g-C_3N_4-based Z-scheme heterojunction toward synergistic enhancement of solar-driven photocatalytic oxygen evolution, *Appl. Catal., B*, 2019, **244**, 240–249.

52 Z. Zhang, J. Huang, Y. Fang, M. Zhang, K. Liu and B. Dong, A Nonmetal Plasmonic Z-Scheme Photocatalyst with UV- to NIR-Driven Photocatalytic Protons Reduction, *Adv. Mater.*, 2017, **29**, 1606688.

53 Z. Zhao, Y. Sun and F. Dong, Graphitic carbon nitride based nanocomposites: a review, *Nanoscale*, 2015, **7**, 15–37.

54 J. Fu, J. Yu, C. Jiang and B. Cheng, g-C_3N_4-Based Heterostructured Photocatalysts, *Adv. Energy Mater.*, 2018, **8**, 1701503.

55 I. F. Teixeira, E. C. M. Barbosa, S. C. E. Tsang and P. H. C. Camargo, Carbon nitrides and metal nanoparticles: from controlled synthesis to design principles for improved photocatalysis, *Chem. Soc. Rev.*, 2018, **47**, 7783–7817.

56 S. Patnaik, S. Martha, S. Acharya and K. M. Parida, An overview of the modification of g-C_3N_4 with high carbon containing materials for photocatalytic applications, *Inorg. Chem. Front.*, 2016, **3**, 336–347.

57 J. Zhang, Y. Chen and X. Wang, Two-dimensional covalent carbon nitride nanosheets: synthesis, functionalization, and applications, *Energy Environ. Sci.*, 2015, **8**, 3092–3108.

58 M. Z. Rahman, K. Davey and C. B. Mullins, Tuning the Intrinsic Properties of Carbon Nitride for High Quantum Yield Photocatalytic Hydrogen Production, *Adv. Sci.*, 2018, **5**, 1800820.

59 W. Jiang, H. Wang, X. Zhang, Y. Zhu and Y. Xie, Two-dimensional polymeric carbon nitride: structural engin-

This journal is © the Partner Organisations 2020

Inorg. Chem. Front., 2020, **7**, 4754–4793 | **4785**

eering for optimizing photocatalysis, *Sci. China: Chem.*, 2018, **61**, 1205–1213.

60 J. Safaei, N. A. Mohamed, M. F. M. Noh, M. F. Soh, N. A. Ludin, M. A. Ibrahim, W. N. Roslam, W. Isahakb and M. A. M. Teridi, Graphitic carbon nitride (g-C_3N_4) electrodes for energy conversion and storage: a review on photo-electrochemical water splitting, solar cells and supercapacitors, *J. Mater. Chem. A*, 2018, **6**, 22346–22380.

61 D. Huang, X. Yan, M. Yan, G. Zeng, C. Zhou, J. Wan, M. Cheng and W. Xue, Graphitic Carbon Nitride-Based Heterojunction Photoactive Nanocomposites: Applications and Mechanism Insight, *ACS Appl. Mater. Interfaces*, 2018, **10**, 21035–21055.

62 B. Zhu, L. Zhang, B. Cheng and J. Yu, First-principle calculation study of tri-s-triazine-based g-C_3N_4: A review, *Appl. Catal., B*, 2018, **224**, 983–999.

63 C. Marchal, T. Cottineau, M. G. Méndez-Medrano, C. Colbeau-Justin, V. Caps and V. Keller, Au/TiO2-g-C_3N_4 Nanocomposites for Enhanced Photocatalytic H2 Production from Water under Visible Light Irradiation with Very Low Quantities of Sacrificial Agents, *Adv. Energy Mater.*, 2018, **8**, 1702142.

64 S. Le, T. Jiang, Y. Li, Q. Zhao, Y. Li, W. Fang and M. Gong, Highly efficient visible-light-driven mesoporous graphitic carbon nitride/ZnO nanocomposite photocatalysts, *Appl. Catal., B*, 2017, **200**, 601–610.

65 L. Jiang, X. Yuan, G. Zeng, J. Liang, X. Chen, H. Yu, H. Wang, Z. Wu, J. Zhang and T. Xiong, *In situ* synthesis of direct solid-state dual Z-scheme WO_3/g-C_3N_4/Bi_2O_3 photocatalyst for the degradation of refractory pollutant, *Appl. Catal., B*, 2018, **227**, 376–385.

66 Y. You, S. Wang, K. Xiao, T. Ma, Y. Zhang and H. Huang, Z-Scheme, g-C_3N_4/Bi_4NbO_8Cl Heterojunction for Enhanced Photocatalytic Hydrogen Production, *ACS Sustainable Chem. Eng.*, 2018, **6**, 16219–16227.

67 C. Li, S. Wang, T. Wang, Y. Wei, P. Zhang and J. Gong, Monoclinic porous $BiVO_4$ networks decorated by discrete g-C_3N_4 nano-islands with tunable coverage for highly efficient photocatalysis, *Small*, 2014, **10**, 2783–2790.

68 M. Liang, T. Borjigin, Y. Zhang, B. Liu, H. Liu and H. Guo, Controlled assemble of hollow heterostructured g-C_3N_4@CeO_2 with rich oxygen vacancies for enhanced photocatalytic CO_2 reduction, *Appl. Catal., B*, 2019, **243**, 566–575.

69 S. Thaweesak, M. Lyu, P. Peerakiatkhajohn, T. Butburee, B. Luo, H. Chen and L. Wang, Two-dimensional g-C_3N_4/$Ca_2Nb_2TaO_{10}$ nanosheet composites for efficient visible light photocatalytic hydrogen evolution, *Appl. Catal., B*, 2017, **202**, 184–190.

70 W. Fu, H. He, Z. Zhang, C. Wu, X. Wang, H. Wang, Q. Zeng, L. Sun, X. Wang, J. Zhou, Q. Fu, P. Yu, Z. Shen, C. Jin, B. I. Yakobson and Z. Liu, Strong interfacial coupling of MoS_2/g-C_3N_4 van de Waals solids for highly active water reduction, *Nano Energy*, 2016, **27**, 44–50.

71 J. W. Shi, Y. Zou, D. Ma, Z. Fan, L. Cheng, D. Sun, Z. Wang, C. Niu and L. Wang, Stable 1T-phase MoS_2 as an effective electron mediator promoting photocatalytic hydrogen production, *Nanoscale*, 2018, **10**, 9292–9303.

72 A. Zada, M. Humayun, F. Raziq, X. Zhang, Y. Qu, L. Bai, C. Qin, L. Jing and H. Fu, Exceptional Visible-Light-Driven Cocatalyst-Free Photocatalytic Activity of g-C_3N_4 by Well Designed Nanocomposites with Plasmonic Au and SnO_2, *Adv. Energy Mater.*, 2016, **6**, 1601190.

73 A. Zhu, L. Qiao, P. Tan, W. Zeng, Y. Ma, R. Dong and J. Pan, Boosted electrocatalytic activity of nitrogen-doped porous carbon triggered by oxygen functional groups, *J. Colloid Interface Sci.*, 2019, **541**, 133–142.

74 H. Gao, H. Yang, J. Xu, S. Zhang and J. Li, Strongly Coupled g-C_3N_4 Nanosheets-Co_3O_4 Quantum Dots as 2D/0D Heterostructure Composite for Peroxymonosulfate Activation, *Small*, 2018, **14**, 1801353.

75 F. Zhang, J. Zhang, J. Li, X. Jin, Y. Li, M. Wu, X. Kang, T. Hu, X. Wang, W. Ren and G. Zhang, Modulating charge transfer dynamics for g-C_3N_4 through a dimension and interface engineered transition metal phosphide co-catalyst for efficient visible-light photocatalytic hydrogen generation, *J. Mater. Chem. A*, 2019, **7**, 6939–6945.

76 A. Zhu, L. Qiao, Z. Jia, P. Tan, Y. Liu, Y. Ma and J. Pan, C-S bond induced ultrafine SnS_2 dot/porous g-C_3N_4 sheet 0D/2D heterojunction: synthesis and photocatalytic mechanism investigation, *Dalton Trans.*, 2017, **46**, 17032–17040.

77 S. Patnaik, G. Swain and K. M. Parida, Highly efficient charge transfer through a double Z-scheme mechanism by a Cu-promoted MoO_3/g-C_3N_4 hybrid nanocomposite with superior electrochemical and photocatalytic performance, *Nanoscale*, 2018, **10**, 5950–5964.

78 W. Zeng, Y. Bian, S. Cao, A. Zhu, L. Qiao, Y. Ma, P. Tan, Q. Ma, R. Dong and J. Pan, Construction of two dimensional $Sr_2Ta_2O_7$/S-doped g-C_3N_4 nanocomposites with Pt cocatalyst for enhanced visible light photocatalytic performance, *Appl. Surf. Sci.*, 2019, **478**, 334–340.

79 T. S. Miller, A. B. Jorge, T. M. Suter, A. Sella, F. Cora and P. F. McMillan, Carbon nitrides: synthesis and characterization of a new class of functional materials, *Phys. Chem. Chem. Phys.*, 2017, **19**, 15613–15638.

80 J. Ran, W. Guo, H. Wang, B. Zhu, J. Yu and S. Z. Qiao, Metal-Free 2D/2D Phosphorene/g-C_3N_4 van der Waals Heterojunction for Highly Enhanced Visible-Light Photocatalytic H_2 Production, *Adv. Mater.*, 2018, **30**, 1800128.

81 D. Tan and F. Garcia, Main group mechanochemistry: from curiosity to established protocols, *Chem. Soc. Rev.*, 2019, **48**, 2274–2292.

82 G. Gorrasi and A. Sorrentino, Mechanical milling as a technology to produce structural and functional bio-nanocomposites, *Green Chem.*, 2015, **17**, 2610–2625.

83 M. Wen, J. Wang, R. Tong, D. Liu, H. Huang, Y. Yu, Z. K. Zhou, P. K. Chu and X. F. Yu, A Low-Cost Metal-Free Photocatalyst Based on Black Phosphorus, *Adv. Sci.*, 2019, **6**, 1801321.

84 X. Chen, H. Chen, J. Guan, J. Zhen, Z. Sun, P. Du, Y. Lu and S. Yang, A facile mechanochemical route to a co-

4786 | *Inorg. Chem. Front.*, 2020, **7**, 4754–4793

This journal is © the Partner Organisations 2020

valently bonded graphitic carbon nitride (g-C_3N_4) and fullerene hybrid toward enhanced visible light photocatalytic hydrogen production, *Nanoscale*, 2017, **9**, 5615–5623.

85 Y. Liang, R. Shang, J. Lu, W. An, J. Hu, L. Liu and W. Cui, 2D MOFs enriched g-C_3N_4 nanosheets for highly efficient charge separation and photocatalytic hydrogen evolution from water, *Int. J. Hydrogen Energy*, 2019, **44**, 2797–2810.

86 J. Zhang, Y. Hu, X. Jiang, S. Chen, S. Meng and X. Fu, Design of a direct Z-scheme photocatalyst: preparation and characterization of Bi_2O_3/g-C_3N_4 with high visible light activity, *J. Hazard. Mater.*, 2014, **280**, 713–722.

87 Y. Guo, J. Li, Z. Gao, X. Zhu, Y. Liu, Z. Wei, W. Zhao and C. Sun, A simple and effective method for fabricating novel p – n heterojunction photocatalyst g-C_3N_4/$Bi_4Ti_3O_{12}$ and its photocatalytic performances, *Appl. Catal., B*, 2016, **192**, 57–71.

88 Q. Zhang, B. Xu, S. Yuan, M. Zhang and T. Ohno, Improving g-C_3N_4 photocatalytic performance by hybridizing with $Bi_2O_2CO_3$ nanosheets, *Catal. Today*, 2017, **284**, 27–36.

89 M. Reli, I. Troppová, M. Šihor, J. Pavlovský, P. Praus and K. Kočí, Photocatalytic decomposition of N_2O over g-C_3N_4/$BiVO_4$ composite, *Appl. Surf. Sci.*, 2019, **469**, 181–191.

90 J. Zhou, M. Zhang and Y. Zhu, Preparation of visible light-driven g-C_3N_4@ZnO hybrid photocatalyst via mechanochemistry, *Phys. Chem. Chem. Phys.*, 2014, **16**, 17627–17633.

91 S. Chen, Y. Hu, X. Jiang, S. Meng and X. Fu, Fabrication and characterization of novel Z-scheme photocatalyst WO_3/g-C_3N_4 with high efficient visible light photocatalytic activity, *Mater. Chem. Phys.*, 2015, **149–150**, 512–521.

92 J. Zhou, M. Zhang and Y. Zhu, Photocatalytic enhancement of hybrid C_3N_4/TiO_2 prepared via ball milling method, *Phys. Chem. Chem. Phys.*, 2015, **17**, 3647–3652.

93 J. Wen, J. Xie, R. Shen, X. Li, X. Luo, H. Zhang, A. Zhang and G. Bi, Markedly enhanced visible-light photocatalytic H_2 generation over g-C_3N_4 nanosheets decorated by robust nickel phosphide ($Ni_{12}P_5$) cocatalysts, *Dalton Trans.*, 2017, **46**, 1794–1802.

94 Q. Chen, H. Hou, D. Zhang, S. Hu, T. Min, B. Liu, C. Yang, W. Pu, J. Hu and J. Yang, Enhanced visible-light driven photocatalytic activity of hybrid ZnO/g-C_3N_4 by high performance ball milling, *J. Photochem. Photobiol., A*, 2018, **350**, 1–9.

95 R. Shen, J. Xie, X. Lu, X. Chen and X. Li, Bifunctional Cu_3P Decorated g-C_3N_4 Nanosheets as a Highly Active and Robust Visible-Light Photocatalyst for H_2 Production, *ACS Sustainable Chem. Eng.*, 2018, **6**, 4026–4036.

96 K. He, J. Xie, Z.-Q. Liu, N. Li, X. Chen, J. Hu and X. Li, Multi-functional Ni_3C cocatalyst/g-C_3N_4 nanoheterojunctions for robust photocatalytic H_2 evolution under visible light, *J. Mater. Chem. A*, 2018, **6**, 13110–13122.

97 X. Chen, P. Tan, B. Zhou, H. Dong, J. Pan and X. Xiong, A green and facile strategy for preparation of novel and stable Cr-doped $SrTiO_3$/g-C_3N_4 hybrid nanocomposites with enhanced visible light photocatalytic activity, *J. Alloys Compd.*, 2015, **647**, 456–462.

98 J. Liu, Q. Jia, J. Long, X. Wang, Z. Gao and Q. Gu, Amorphous NiO as co-catalyst for enhanced visible-light-driven hydrogen generation over g-C_3N_4 photocatalyst, *Appl. Catal., B*, 2018, **222**, 35–43.

99 Q. Han, B. Wang, J. Gao and L. Qu, Graphitic Carbon Nitride/Nitrogen-Rich Carbon Nanofibers: Highly Efficient Photocatalytic Hydrogen Evolution without Cocatalysts, *Angew. Chem., Int. Ed.*, 2016, **55**, 10849–10853.

100 Y. Sun, D. Jin, Y. Sun, X. Meng, Y. Gao, Y. Dall'Agnese, G. Chen and X.-F. Wang, g-C_3N_4/$Ti_3C_2T_x$ (MXenes) composite with oxidized surface groups for efficient photocatalytic hydrogen evolution, *J. Mater. Chem. A*, 2018, **6**, 9124–9131.

101 C. Yang, J. Qin, Z. Xue, M. Ma, X. Zhang and R. Liu, Rational design of carbon-doped TiO_2 modified g-C_3N_4 via *in situ* heat treatment for drastically improved photocatalytic hydrogen with excellent photostability, *Nano Energy*, 2017, **41**, 1–9.

102 H. Shi, G. Chen, C. Zhang and Z. Zou, Polymeric g-C_3N_4 Coupled with $NaNbO_3$ Nanowires toward Enhanced Photocatalytic Reduction of CO_2 into Renewable Fuel, *ACS Catal.*, 2014, **4**, 3637–3643.

103 W. Yu, J. Chen, T. Shang, L. Chen, L. Gu and T. Peng, Direct Z-scheme g-C_3N_4/WO_3 photocatalyst with atomically defined junction for H_2 production, *Appl. Catal., B*, 2017, **219**, 693–704.

104 M. Han, H. Wang, S. Zhao, L. Hu, H. Huang and Y. Liu, One-step synthesis of CoO/g-C_3N_4 composites by thermal decomposition for overall water splitting without sacrificial reagents, *Inorg. Chem. Front.*, 2017, **4**, 1691–1696.

105 X. She, J. Wu, H. Xu, J. Zhong, Y. Wang, Y. Song, K. Nie, Y. Liu, Y. Yang, M.-T. F. Rodrigues, R. Vajtai, J. Lou, D. Du, H. Li and P. M. Ajayan, High Efficiency Photocatalytic Water Splitting Using 2D α-Fe_2O_3/g-C_3N_4 Z-Scheme Catalysts, *Adv. Energy Mater.*, 2017, **7**, 1700025.

106 M. Shao, Y. Shao, J. Chai, Y. Qu, M. Yang, Z. Wang, M. Yang, W. F. Ip, C. T. Kwok, X. Shi, Z. Lu, S. Wang, X. Wang and H. Pan, Synergistic effect of 2D Ti_2C and g-C_3N_4 for efficient photocatalytic hydrogen production, *J. Mater. Chem. A*, 2017, **5**, 16748–16756.

107 Y. Wang, X. Liu, J. Liu, B. Han, X. Hu, F. Yang, Z. Xu, Y. Li, S. Jia, Z. Li and Y. Zhao, Carbon Quantum Dot Implanted Graphite Carbon Nitride Nanotubes: Excellent Charge Separation and Enhanced Photocatalytic Hydrogen Evolution, *Angew. Chem., Int. Ed.*, 2018, **57**, 5765–5771.

108 G. Li, Z. Lian, W. Wang, D. Zhang and H. Li, Nanotube-confinement induced size-controllable g-C_3N_4 quantum dots modified single-crystalline TiO_2 nanotube arrays for stable synergetic photoelectrocatalysis, *Nano Energy*, 2016, **19**, 446–454.

109 W. Wu, X. Li, Z. Ruan, Y. Li, X. Xu, Y. Yuan and K. Lin, Fabrication of a TiO_2 trapped meso/macroporous g-C_3N_4 heterojunction photocatalyst and understanding its enhanced photocatalytic activity based on optical simulation analysis, *Inorg. Chem. Front.*, 2018, **5**, 481–489.

This journal is © the Partner Organisations 2020

Inorg. Chem. Front., 2020, **7**, 4754–4793 | **4787**

110 T. Zhao, Z. Xing, Z. Xiu, Z. Li, S. Yang and W. Zhou, Oxygen-Doped MoS_2 Nanospheres/CdS Quantum Dots/ g-C_3N_4 Nanosheets Super-Architectures for Prolonged Charge Lifetime and Enhanced Visible-Light-Driven Photocatalytic Performance, *ACS Appl. Mater. Interfaces*, 2019, **11**, 7104–7111.

111 J.-Y. Tang, D. Yang, W.-G. Zhou, R.-T. Guo, W.-G. Pan and C.-Y. Huang, Noble-metal-free molybdenum phosphide co-catalyst loaded graphitic carbon nitride for efficient photocatalysis under simulated irradiation, *J. Catal.*, 2019, **370**, 79–87.

112 Z. Mo, H. Xu, Z. Chen, X. She, Y. Song, J. Lian, X. Zhu, P. Yan, Y. Lei, S. Yuan and H. Li, Construction of MnO_2/ Monolayer g-C_3N_4 with Mn vacancies for Z-scheme overall water splitting, *Appl. Catal., B*, 2019, **241**, 452–460.

113 B. Zhu, P. Xia, W. Ho and J. Yu, Isoelectric point and adsorption activity of porous g-C3N4, *Appl. Surf. Sci.*, 2015, **344**, 188–195.

114 J. Hu, Y. Ji, Z. Mo, N. Li, Q. Xu, Y. Li, H. Xu, D. Chen and J. Lu, Engineering black phosphorus to porous g-C_3N_4- metal–organic framework membrane: a platform for highly boosting photocatalytic performance, *J. Mater. Chem. A*, 2019, **7**, 4408–4414.

115 T. Song, G. Zeng, P. Zhang, T. Wang, A. Ali, S. Huang and H. Zeng, 3D reticulated carbon nitride materials high-uni-formly capture 0D black phosphorus as 3D/0D composites for stable and efficient photocatalytic hydrogen evolution, *J. Mater. Chem. A*, 2019, **7**, 503–512.

116 W. Zhou, T. Jia, H. Shi, D. Yu, W. Hong and X. Chen, Conjugated polymer dots/graphitic carbon nitride nanosheet heterojunctions for metal-free hydrogen evolution photocatalysis, *J. Mater. Chem. A*, 2019, **7**, 303–311.

117 Y. Zheng, Z. Yu, H. Ou, A. M. Asiri, Y. Chen and X. Wang, Black Phosphorus and Polymeric Carbon Nitride Heterostructure for Photoinduced Molecular Oxygen Activation, *Adv. Funct. Mater.*, 2018, **28**, 1705407.

118 M. Zhu, S. Kim, L. Mao, M. Fujitsuka, J. Zhang, X. Wang and T. Majima, Metal-Free Photocatalyst for H2 Evolution in Visible to Near-Infrared Region: Black Phosphorus/ Graphitic Carbon Nitride, *J. Am. Chem. Soc.*, 2017, **139**, 13234–13242.

119 Q. Zhang, S. Huang, J. Deng, D. T. Gangadharan, F. Yang, Z. Xu, G. Giorgi, M. Palummo, M. Chaker and D. Ma, Ice-Assisted Synthesis of Black Phosphorus Nanosheets as a Metal-Free Photocatalyst: 2D/2D Heterostructure for Broadband H_2 Evolution, *Adv. Funct. Mater.*, 2019, **29**, 1902486.

120 W. Lei, Y. Mi, R. Feng, P. Liu, S. Hu, J. Yu, X. Liu, J. A. Rodriguez, J.-O. Wang, L. Zheng, K. Tang, S. Zhu, G. Liu and M. Liu, Hybrid 0D–2D black phosphorus quantum dots–graphitic carbon nitride nanosheets for efficient hydrogen evolution, *Nano Energy*, 2018, **50**, 552–561.

121 L. Kong, Y. Ji, Z. Dang, J. Yan, P. Li, Y. Li and S. F. Liu, g-C_3N_4 Loading Black Phosphorus Quantum Dot for Efficient and Stable Photocatalytic H_2 Generation under Visible Light, *Adv. Funct. Mater.*, 2018, **28**, 1800668.

122 Y. Fu, T. Huang, B. Jia, J. Zhu and X. Wang, Reduction of nitrophenols to aminophenols under concerted catalysis by Au/g-C_3N_4 contact system, *Appl. Catal., B*, 2017, **202**, 430–437.

123 W.-D. Oh, L.-W. Lok, A. Veksha, A. Giannis and T.-T. Lim, Enhanced photocatalytic degradation of bisphenol A with Ag-decorated S-doped g-C_3N_4 under solar irradiation: Performance and mechanistic studies, *Chem. Eng. J.*, 2018, **333**, 739–749.

124 O. Fontelles-Carceller, M. J. Munoz-Batista, M. Fernandez-Garcia and A. Kubacka, Interface Effects in Sunlight-Driven Ag/g-C_3N_4 Composite Catalysts: Study of the Toluene Photodegradation Quantum Efficiency, *ACS Appl. Mater. Interfaces*, 2016, **8**, 2617–2627.

125 J. Qin, J. Huo, P. Zhang, J. Zeng, T. Wang and H. Zeng, Improving the photocatalytic hydrogen production of Ag/ g-C_3N_4 nanocomposites by dye-sensitization under visible light irradiation, *Nanoscale*, 2016, **8**, 2249–2259.

126 Y. Song, J. Qi, J. Tian, S. Gao and F. Cui, Construction of Ag/g-C_3N_4 photocatalysts with visible-light photocatalytic activity for sulfamethoxazole degradation, *Chem. Eng. J.*, 2018, **341**, 547–555.

127 J. Zhang, M. Zhang, C. Yang and X. Wang, Nanospherical carbon nitride frameworks with sharp edges accelerating charge collection and separation at a soft photocatalytic interface, *Adv. Mater.*, 2014, **26**, 4121–4126.

128 B. Zhu, P. Xia, Y. Li, W. Ho and J. Yu, Fabrication and photocatalytic activity enhanced mechanism of direct Z-scheme g-C_3N_4/Ag_2WO_4 photocatalyst, *Appl. Surf. Sci.*, 2017, **391**, 175–183.

129 H. Li, S. Gan, H. Wang, D. Han and L. Niu, Intercorrelated Superhybrid of AgBr Supported on Graphitic-C_3N_4-Decorated Nitrogen-Doped Graphene: High Engineering Photocatalytic Activities for Water Purification and CO_2 Reduction, *Adv. Mater.*, 2015, **27**, 6906–6913.

130 Y. Li, L. Fang, R. Jin, Y. Yang, X. Fang, Y. Xing and S. Song, Preparation and enhanced visible light photo-catalytic activity of novel g-C_3N_4 nanosheets loaded with Ag_2CO_3 nanoparticles, *Nanoscale*, 2015, **7**, 758–764.

131 M.-Y. Ye, Z.-H. Zhao, Z.-F. Hu, L.-Q. Liu, H.-M. Ji, Z.-R. Shen and T.-Y. Ma, 0D/2D Heterojunctions of Vanadate Quantum Dots/Graphitic Carbon Nitride Nanosheets for Enhanced Visible-Light-Driven Photocatalysis, *Angew. Chem., Int. Ed.*, 2017, **56**, 8407–8411.

132 J. Cai, J. Huang, S. Wang, J. Iocozzia, Z. Sun, J. Sun, Y. Yang, Y. Lai and Z. Lin, Crafting Mussel-Inspired Metal Nanoparticle-Decorated Ultrathin Graphitic Carbon Nitride for the Degradation of Chemical Pollutants and Production of Chemical Resources, *Adv. Mater.*, 2019, **31**, 1806314.

133 L. Ma, G. Wang, C. Jiang, H. Bao and Q. Xu, Synthesis of core-shell TiO_2 @ g-C_3N_4 hollow microspheres for efficient photocatalytic degradation of rhodamine B under visible light, *Appl. Surf. Sci.*, 2018, **430**, 263–272.

4788 | *Inorg. Chem. Front.*, 2020, **7**, 4754–4793

This journal is © the Partner Organisations 2020

134 D. Zeng, W. Xu, W.-J. Ong, J. Xu, H. Ren, Y. Chen, H. Zheng and D.-L. Peng, Toward noble-metal-free visible-light-driven photocatalytic hydrogen evolution: Monodisperse sub–15 nm Ni_2P nanoparticles anchored on porous g-C_3N_4 nanosheets to engineer 0D–2D hetero-junction interfaces, *Appl. Catal., B*, 2018, **221**, 47–55.

135 G. Zhang, S. Zang and X. Wang, Layered $Co(OH)_2$ Deposited Polymeric Carbon Nitrides for Photocatalytic Water Oxidation, *ACS Catal.*, 2015, **5**, 941–947.

136 Y. Deng, L. Tang, G. Zeng, J. Wang, Y. Zhou, J. Wang, J. Tang, L. Wang and C. Feng, Facile fabrication of mediator-free Z-scheme photocatalyst of phosphorous-doped ultrathin graphitic carbon nitride nanosheets and bismuth vanadate composites with enhanced tetracycline degradation under visible light, *J. Colloid Interface Sci.*, 2018, **509**, 219–234.

137 Y. Gong, B. Yang, H. Zhang and X. Zhao, A g-C_3N_4/MIL-101(Fe) heterostructure composite for highly efficient BPA degradation with persulfate under visible light irradiation, *J. Mater. Chem. A*, 2018, **6**, 23703–23711.

138 N. Zhao, L. Kong, Y. Dong, G. Wang, X. Wu and P. Jiang, Insight into the Crucial Factors for Photochemical Deposition of Cobalt Cocatalysts on g-C_3N_4 Photocatalysts, *ACS Appl. Mater. Interfaces*, 2018, **10**, 9522–9531.

139 M.-H. Vu, M. Sakar, C.-C. Nguyen and T.-O. Do, Chemically Bonded Ni Cocatalyst onto the S Doped g-C_3N_4 Nanosheets and Their Synergistic Enhancement in H_2 Production under Sunlight Irradiation, *ACS Sustainable Chem. Eng.*, 2018, **6**, 4194–4203.

140 S. Yang, Y. Gong, J. Zhang, L. Zhan, L. Ma, Z. Fang, R. Vajtai, X. Wang and P. M. Ajayan, Exfoliated graphitic carbon nitride nanosheets as efficient catalysts for hydrogen evolution under visible light, *Adv. Mater.*, 2013, **25**, 2452–2456.

141 J. Chu, X. Han, Z. Yu, Y. Du, B. Song and P. Xu, Highly Efficient Visible-Light-Driven Photocatalytic Hydrogen Production on CdS/Cu_7S_4/g-C_3N_4 Ternary Heterostructures, *ACS Appl. Mater. Interfaces*, 2018, **10**, 20404–20411.

142 W.-J. Ong, L.-L. Tan, S.-P. Chai, S.-T. Yong and A. R. Mohamed, Surface charge modification via protona-tion of graphitic carbon nitride (g-C_3N_4) for electrostatic self-assembly construction of 2D/2D reduced graphene oxide (rGO)/g-C_3N_4 nanostructures toward enhanced photocatalytic reduction of carbon dioxide to methane, *Nano Energy*, 2015, **13**, 757–770.

143 M. Ou, W. Tu, S. Yin, W. Xing, S. Wu, H. Wang, S. Wan, Q. Zhong and R. Xu, Amino-Assisted Anchoring of $CsPbBr_3$ Perovskite Quantum Dots on Porous g-C_3N_4 for Enhanced Photocatalytic CO_2 Reduction, *Angew. Chem., Int. Ed.*, 2018, **57**, 13570–13574.

144 Z. Jiang, W. Wan, H. Li, S. Yuan, H. Zhao and P. K. Wong, A Hierarchical Z-Scheme alpha-Fe_2O_3/g-C_3N_4 Hybrid for Enhanced Photocatalytic CO_2 Reduction, *Adv. Mater.*, 2018, **30**, 1706108.

145 D. Lu, P. Fang, W. Wu, J. Ding, L. Jiang, X. Zhao, C. Li, M. Yang, Y. Li and D. Wang, Solvothermal-assisted syn-thesis of self-assembling TiO_2 nanorods on large graphitic carbon nitride sheets with their anti-recombination in the photocatalytic removal of Cr(vi) and rhodamine B under visible light irradiation, *Nanoscale*, 2017, **9**, 3231–3245.

146 Y. Fu, C. A. Liu, C. Zhu, H. Wang, Y. Dou, W. Shi, M. Shao, H. Huang, Y. Liu and Z. Kang, High-performance NiO/g-C_3N_4 composites for visible-light-driven photocatalytic overall water splitting, *Inorg. Chem. Front.*, 2018, **5**, 1646–1652.

147 Z. Zhu, P. Huo, Z. Lu, Y. Yan, Z. Liu, W. Shi, C. Li and H. Dong, Fabrication of magnetically recoverable photoca-talysts using g-C_3N_4 for effective separation of charge car-riers through like-Z-scheme mechanism with Fe_3O_4 mediator, *Chem. Eng. J.*, 2018, **331**, 615–625.

148 S. Tonda, S. Kumar, M. Bhardwaj, P. Yadav and S. Ogale, g-C_3N_4/NiAl-LDH 2D/2D Hybrid Heterojunction for High-Performance Photocatalytic Reduction of CO_2 into Renewable Fuels, *ACS Appl. Mater. Interfaces*, 2018, **10**, 2667–2678.

149 W.-K. Jo and N. C. S. Selvam, Z-scheme CdS/g-C_3N_4 com-posites with RGO as an electron mediator for efficient photocatalytic H_2 production and pollutant degradation, *Chem. Eng. J.*, 2017, **317**, 913–924.

150 M. Liang, T. Borjigin, Y. Zhang, H. Liu, B. Liu and H. Guo, Z-Scheme, Au@Void@ g-C_3N_4/SnS Yolk-Shell Heterostructures for Superior Photocatalytic CO_2 Reduction under Visible Light, *ACS Appl. Mater. Interfaces*, 2018, **10**, 34123–34131.

151 Y. Hou, Z. Wen, S. Cui, X. Guo and J. Chen, Constructing 2D porous graphitic C_3N_4 nanosheets/nitrogen-doped graphene/layered MoS_2 ternary nanojunction with enhanced photoelectrochemical activity, *Adv. Mater.*, 2013, **25**, 6291–6297.

152 J. Fu, C. Bie, B. Cheng, C. Jiang and J. Yu, Hollow CoS_x Polyhedrons Act as High-Efficiency Cocatalyst for Enhancing the Photocatalytic Hydrogen Generation of g-C_3N_4, *ACS Sustainable Chem. Eng.*, 2018, **6**, 2767–2779.

153 F.-Y. Tian, D. Hou, F. Tang, M. Deng, X.-Q. Qiao, Q. Zhang, T. Wu and D.-S. Li, Novel $Zn_{0.8}Cd_{0.2}S$@g-C_3N_4 core–shell heterojunctions with a twin structure for enhanced visible-light-driven photocatalytic hydrogen generation, *J. Mater. Chem. A*, 2018, **6**, 17086–17094.

154 B. Lin, H. Li, H. An, W. Hao, J. Wei, Y. Dai, C. Ma and G. Yang, Preparation of 2D/2D g-C_3N_4 nanosheet@$ZnIn_2S_4$ nanoleaf heterojunctions with well-designed high-speed charge transfer nanochannels towards high-efficiency photocatalytic hydrogen evolution, *Appl. Catal., B*, 2018, **220**, 542–552.

155 D. Jiang, T. Wang, Q. Xu, D. Li, S. Meng and M. Chen, Perovskite oxide ultrathin nanosheets/g-C_3N_4 2D–2D het-erojunction photocatalysts with significantly enhanced photocatalytic activity towards the photodegradation of tetracycline, *Appl. Catal., B*, 2017, **201**, 617–628.

156 Z. Wang, Y. Huang, L. Chen, M. Chen, J. Cao, W. Ho and S. C. Lee, In situ g-C_3N_4 self-sacrificial synthesis of a g-C_3N_4/$LaCO_3OH$ heterostructure with strong interfacial

This journal is © the Partner Organisations 2020

Inorg. Chem. Front., 2020, **7**, 4754–4793 | **4789**

charge transfer and separation for photocatalytic NO removal, *J. Mater. Chem. A*, 2018, **6**, 972–981.

157 J. Li, Y. Yin, E. Liu, Y. Ma, J. Wan, J. Fan and X. Hu, In situ growing Bi_2MoO_6 on $g-C_3N_4$ nanosheets with enhanced photocatalytic hydrogen evolution and disinfection of bacteria under visible light irradiation, *J. Hazard. Mater.*, 2017, **321**, 183–192.

158 Q. Wang, W. Wang, L. Zhong, D. Liu, X. Cao and F. Cui, Oxygen vacancy-rich 2D/2D $BiOCl-g-C_3N_4$ ultrathin heterostructure nanosheets for enhanced visible-light-driven photocatalytic activity in environmental remediation, *Appl. Catal., B*, 2018, **220**, 290–302.

159 A. Bafaqeer, M. Tahir and N. A. S. Amin, Well-designed $ZnV_2O_6/g-C_3N_4$ 2D/2D nanosheets heterojunction with faster charges separation via pCN as mediator towards enhanced photocatalytic reduction of CO_2 to fuels, *Appl. Catal., B*, 2019, **242**, 312–326.

160 H. Zhao, G. Li, F. Tian, Q. Jia, Y. Liu and R. Chen, $g-C_3N_4$ surface-decorated $Bi_2O_2CO_3$ for improved photocatalytic performance: Theoretical calculation and photodegradation of antibiotics in actual water matrix, *Chem. Eng. J.*, 2019, **366**, 468–479.

161 X. Guo, H. Dong, T. Xia, T. Wang, H. Jia and L. Zhu, Highly Efficient Degradation toward Tylosin in the Aqueous Solution by Carbon Spheres/$g-C_3N_4$ Composites under Simulated Sunlight Irradiation, *ACS Sustainable Chem. Eng.*, 2018, **6**, 12776–12786.

162 Y.-Y. Han, X.-L. Lu, S.-F. Tang, X.-P. Yin, Z.-W. Wei and T.-B. Lu, Metal-Free 2D/2D Heterojunction of Graphitic Carbon Nitride/Graphdiyne for Improving the Hole Mobility of Graphitic Carbon Nitride, *Adv. Energy Mater.*, 2018, **8**, 1702992.

163 A. Yuan, H. Lei, F. Xi, J. Liu, L. Qin, Z. Chen and X. Dong, Graphene quantum dots decorated graphitic carbon nitride nanorods for photocatalytic removal of antibiotics, *J. Colloid Interface Sci.*, 2019, **548**, 56–65.

164 H. Jia, D. Ma, S. Zhong, L. Li, L. Li, L. Xu and B. Li, Boosting photocatalytic activity under visible-light by creation of PCN-222/$g-C_3N_4$ heterojunctions, *Chem. Eng. J.*, 2019, **368**, 165–174.

165 Z. Zhang, J. Huang, M. Zhang, Q. Yuan and B. Dong, Ultrathin hexagonal SnS_2 nanosheets coupled with $g-C_3N_4$ nanosheets as 2D/2D heterojunction photocatalysts toward high photocatalytic activity, *Appl. Catal., B*, 2015, **163**, 298–305.

166 Y. Liu, P. Chen, Y. Chen, H. Lu, J. Wang, Z. Yang, Z. Lu, M. Li and L. Fang, In situ ion-exchange synthesis of $SnS_2/g-C_3N_4$ nanosheets heterojunction for enhancing photocatalytic activity, *RSC Adv.*, 2016, **6**, 10802–10809.

167 Y. Song, J. Gu, K. Xia, J. Yi, H. Chen, X. She, Z. Chen, C. Ding, H. Li and H. Xu, Construction of 2D $SnS_2/g-C_3N_4$ Z-scheme composite with superior visible-light photocatalytic performance, *Appl. Surf. Sci.*, 2019, **467–468**, 56–64.

168 M. Sun, Q. Yan, T. Yan, M. Li, D. Wei, Z. Wang, Q. Wei and B. Du, Facile fabrication of 3D flower-like heterostruc-

tured $g-C_3N_4/SnS_2$ composite with efficient photocatalytic activity under visible light, *RSC Adv.*, 2014, **4**, 31019–31027.

169 S. A. Ansari and M. H. Cho, Growth of three-dimensional flower-like SnS_2 on $g-C_3N_4$ sheets as an efficient visible-light photocatalyst, photoelectrode, and electrochemical supercapacitance material, *Sustainable Energy Fuels*, 2017, **1**, 510–519.

170 L. Jing, Y. Xu, Z. Chen, M. He, M. Xie, J. Liu, H. Xu, S. Huang and H. Li, Different Morphologies of SnS_2 Supported on 2D $g-C_3N_4$ for Excellent and Stable Visible Light Photocatalytic Hydrogen Generation, *ACS Sustainable Chem. Eng.*, 2018, **6**, 5132–5141.

171 R. Zhong, Z. Zhang, S. Luo, Z. C. Zhang, L. Huang and M. Gu, Comparison of TiO_2 and $g-C_3N_4$ 2D/2D nanocomposites from three synthesis protocols for visible-light induced hydrogen evolution, *Catal. Sci. Technol.*, 2019, **9**, 75–85.

172 W. Jiang, X. Zong, L. An, S. Hua, X. Miao, S. Luan, Y. Wen, F. F. Tao and Z. Sun, Consciously Constructing Heterojunction or Direct Z-Scheme Photocatalysts by Regulating Electron Flow Direction, *ACS Catal.*, 2018, **8**, 2209–2217.

173 J. Qin and H. Zeng, Photocatalysts fabricated by depositing plasmonic Ag nanoparticles on carbon quantum dots/graphitic carbon nitride for broad spectrum photocatalytic hydrogen generation, *Appl. Catal., B*, 2017, **209**, 161–173.

174 Y. Wang, X. Liu, C. Zheng, Y. Li, S. Jia, Z. Li and Y. Zhao, Tailoring TiO_2 Nanotube-Interlaced Graphite Carbon Nitride Nanosheets for Improving Visible-Light-Driven Photocatalytic Performance, *Adv. Sci.*, 2018, **5**, 1700844.

175 K. He, J. Xie, M. Li and X. Li, In situ one-pot fabrication of $g-C_3N_4$ nanosheets/NiS cocatalyst heterojunction with intimate interfaces for efficient visible light photocatalytic H_2 generation, *Appl. Surf. Sci.*, 2018, **430**, 208–217.

176 F. Wang, Y. Wang, Y. Feng, Y. Zeng, Z. Xie, Q. Zhang, Y. Su, P. Chen, Y. Liu, K. Yao, W. Lv and G. Liu, Novel ternary photocatalyst of single atom-dispersed silver and carbon quantum dots co-loaded with ultrathin $g-C_3N_4$ for broad spectrum photocatalytic degradation of naproxen, *Appl. Catal., B*, 2018, **221**, 510–520.

177 A. Kumar, A. Rana, G. Sharma, M. Naushad, A. H. Al-Muhtaseb, C. Guo, A. Iglesias-Juez and F. J. Stadler, High-Performance Photocatalytic Hydrogen Production and Degradation of Levofloxacin by Wide Spectrum-Responsive Ag/Fe_3O_4 Bridged $SrTiO_3/g-C_3N_4$ Plasmonic Nanojunctions: Joint Effect of Ag and Fe_3O_4, *ACS Appl. Mater. Interfaces*, 2018, **10**, 40474–40490.

178 Y. Xiao, X. Tao, G. Qiu, Z. Dai, P. Gao and B. Li, Optimal synthesis of a direct Z-scheme photocatalyst with ultrathin $W_{18}O_{49}$ nanowires on $g-C_3N_4$ nanosheets for solar-driven oxidation reactions, *J. Colloid Interface Sci.*, 2019, **550**, 99–109.

179 W. J. Ong, L. L. Tan, S. P. Chai and S. T. Yong, Graphene oxide as a structure-directing agent for the two-dimen-

sional interface engineering of sandwich-like graphene-g-C₃N₄ hybrid nanostructures with enhanced visible-light photoreduction of CO_2 to methane, *Chem. Commun.*, 2015, **51**, 858–861.

180 T. Song, G. Zeng, P. Zhang, T. Wang, S. Huang and H. Zeng, Ultrathin Carbon Nitride with Atomic-Level Intraplane Implantation of Graphited Carbon Ring Domain for Superior Photocatalytic Activity in the Visible/Near-Infrared Region, *ACS Sustainable Chem. Eng.*, 2018, **7**, 1239–1249.

181 P. Xia, B. Zhu, B. Cheng, J. Yu and J. Xu, 2D/2D g-C₃N₄/MnO₂ Nanocomposite as a Direct Z-Scheme Photocatalyst for Enhanced Photocatalytic Activity, *ACS Sustainable Chem. Eng.*, 2017, **6**, 965–973.

182 X. Shi, M. Fujitsuka, S. Kim and T. Majima, Faster Electron Injection and More Active Sites for Efficient Photocatalytic H_2 Evolution in g-C₃N₄/MoS₂ Hybrid, *Small*, 2018, **14**, 1703277.

183 C. Li, Y. Du, D. Wang, S. Yin, W. Tu, Z. Chen, M. Kraft, G. Chen and R. Xu, Unique P-Co-N Surface Bonding States Constructed on g-C₃N₄ Nanosheets for Drastically Enhanced Photocatalytic Activity of H_2 Evolution, *Adv. Funct. Mater.*, 2017, **27**, 1604328.

184 L. Yang, J. Huang, L. Shi, L. Cao, H. Liu, Y. Liu, Y. Li, H. Song, Y. Jie and J. Ye, Sb doped SnO₂-decorated porous g-C₃N₄ nanosheet heterostructures with enhanced photocatalytic activities under visible light irradiation, *Appl. Catal., B*, 2018, **221**, 670–680.

185 H. Li, Y. Gao, Z. Xiong, C. Liao and K. Shih, Enhanced selective photocatalytic reduction of CO_2 to CH_4 over plasmonic Au modified g-C₃N₄ photocatalyst under UV–vis light irradiation, *Appl. Surf. Sci.*, 2018, **439**, 552–559.

186 T. B. Nguyen, C. P. Huang and R.-A. Doong, Enhanced catalytic reduction of nitrophenols by sodium borohydride over highly recyclable Au@graphitic carbon nitride nanocomposites, *Appl. Catal., B*, 2019, **240**, 337–347.

187 F. Fina, H. Ménard and J. T. S. Irvine, The effect of Pt NPs crystallinity and distribution on the photocatalytic activity of Pt–g-C₃N₄, *Phys. Chem. Chem. Phys.*, 2015, **17**, 13929–13936.

188 M. Caux, F. Fina, J. T. S. Irvine, H. Idriss and R. Howe, Impact of the annealing temperature on Pt/g-C₃N₄ structure, activity and selectivity between photodegradation and water splitting, *Catal. Today*, 2017, **287**, 182–188.

189 K. Gu, X. Pan, W. Wang, J. Ma, Y. Sun, H. Yang, H. Shen, Z. Huang and H. Liu, In Situ Growth of Pd Nanosheets on g-C₃N₄ Nanosheets with Well-Contacted Interface and Enhanced Catalytic Performance for 4-Nitrophenol Reduction, *Small*, 2018, **14**, 1801812.

190 J. Ding, G. Long, Y. Luo, R. Sun, M. Chen, Y. Li, Y. Zhou, X. Xu and W. Zhao, Photocatalytic reductive dechlorination of 2-chlorodibenzo-p-dioxin by Pd modified g-C₃N₄ photocatalysts under UV–vis irradiation: Efficacy, kinetics and mechanism, *J. Hazard. Mater.*, 2018, **355**, 74–81.

191 Y. Guo, H. Jia, J. Yang, H. Yin, Z. Yang, J. Wang and B. Yang, Understanding the roles of plasmonic Au nanocrystal size, shape, aspect ratio and loading amount in Au/g-C₃N₄ hybrid nanostructures for photocatalytic hydrogen generation, *Phys. Chem. Chem. Phys.*, 2018, **20**, 22296–22307.

192 S. Cao, J. Jiang, B. Zhu and J. Yu, Shape-dependent photocatalytic hydrogen evolution activity over a Pt nanoparticle coupled g-C₃N₄ photocatalyst, *Phys. Chem. Chem. Phys.*, 2016, **18**, 19457–19463.

193 S. Samanta, S. Martha and K. Parida, Facile Synthesis of Au/g-C₃N₄ Nanocomposites: An Inorganic/Organic Hybrid Plasmonic Photocatalyst with Enhanced Hydrogen Gas Evolution Under Visible-Light Irradiation, *ChemCatChem*, 2014, **6**, 1453–1462.

194 Y. Zou, J.-W. Shi, D. Ma, Z. Fan, L. Lu and C. Niu, In situ synthesis of C-doped TiO₂@g-C₃N₄ core-shell hollow nanospheres with enhanced visible-light photocatalytic activity for H2 evolution, *Chem. Eng. J.*, 2017, **322**, 435–444.

195 R. He, J. Zhou, H. Fu, S. Zhang and C. Jiang, Room-temperature in situ fabrication of Bi₂O₃/g-C₃N₄ direct Z-scheme photocatalyst with enhanced photocatalytic activity, *Appl. Surf. Sci.*, 2018, **430**, 273–282.

196 F. Guo, W. Shi, H. Wang, H. Huang, Y. Liu and Z. Kang, Fabrication of a CuBi₂O₄/g-C₃N₄ p–n heterojunction with enhanced visible light photocatalytic efficiency toward tetracycline degradation, *Inorg. Chem. Front.*, 2017, **4**, 1714–1720.

197 H. Che, G. Che, P. Zhou, C. Liu and H. Dong, Yeast-derived carbon sphere as a bridge of charge carriers towards to enhanced photocatalytic activity of 2D/2D Cu₂WS₄/g-C₃N₄ heterojunction, *J. Colloid Interface Sci.*, 2019, **546**, 262–275.

198 T. Su, Z. D. Hood, M. Naguib, L. Bai, S. Luo, C. M. Rouleau, I. N. Ivanov, H. Ji, Z. Qin and Z. Wu, 2D/2D heterojunction of Ti₃C₂/g-C₃N₄ nanosheets for enhanced photocatalytic hydrogen evolution, *Nanoscale*, 2019, **11**, 8138–8149.

199 J. Ge, Y. Liu, D. Jiang, L. Zhang and P. Du, Integrating non-precious-metal cocatalyst Ni₃N with g-C₃N₄ for enhanced photocatalytic H_2 production in water under visible-light irradiation, *Chin. J. Catal.*, 2019, **40**, 160–167.

200 L. Chen, H. Huang, Y. Zheng, W. Sun, Y. Zhao, P. S. Francis and X. Wang, Noble-metal-free Ni₃N/g-C₃N₄ photocatalysts with enhanced hydrogen production under visible light irradiation, *Dalton Trans.*, 2018, **47**, 12188–12196.

201 Q. Zhu, B. Qiu, M. Du, M. Xing and J. Zhang, Nickel Boride Cocatalyst Boosting Efficient Photocatalytic Hydrogen Evolution Reaction, *Ind. Eng. Chem. Res.*, 2018, **57**, 8125–8130.

202 D. Zeng, W.-J. Ong, H. Zheng, M. Wu, Y. Chen, D.-L. Peng and M.-Y. Han, Ni₁₂P₅ nanoparticles embedded into porous g-C₃N₄ nanosheets as a noble-metal-free hetero-

This journal is © the Partner Organisations 2020

Inorg. Chem. Front., 2020, **7**, 4754–4793 | **4791**

structure photocatalyst for efficient H_2 production under visible light, *J. Mater. Chem. A*, 2017, **5**, 16171–16178.

203 X. J. Wang, X. Tian, Y. J. Sun, J. Y. Zhu, F. T. Li, H. Y. Mu and J. Zhao, Enhanced Schottky effect of a 2D–2D CoP/g-C_3N_4 interface for boosting photocatalytic H_2 evolution, *Nanoscale*, 2018, **10**, 12315–12321.

204 L. Bi, X. Gao, L. Zhang, D. Wang, X. Zou and T. Xie, Enhanced Photocatalytic Hydrogen Evolution of NiCoP/g-C_3N_4 with Improved Separation Efficiency and Charge Transfer Efficiency, *ChemSusChem*, 2018, **11**, 276–284.

205 S. P. Adhikari, Z. D. Hood, V. W. Chen, K. L. More, K. Senevirathne and A. Lachgar, Visible-light-active g-C_3N_4/N-doped $Sr_2Nb_2O_7$ heterojunctions as photocatalysts for the hydrogen evolution reaction, *Sustainable Energy Fuels*, 2018, **2**, 2507–2515.

206 X. Xu, G. Liu, C. Randorn and J. T. S. Irvine, g-C_3N_4 coated $SrTiO_3$ as an efficient photocatalyst for H_2 production in aqueous solution under visible light irradiation, *Int. J. Hydrogen Energy*, 2011, **36**, 13501–13507.

207 H. W. Kang, S. N. Lim, D. Song and S. B. Park, Organic-inorganic composite of g-C_3N_4–$SrTiO_3$:Rh photocatalyst for improved H_2 evolution under visible light irradiation, *Int. J. Hydrogen Energy*, 2012, **37**, 11602–11610.

208 W.-J. Ong, L. K. Putri, L.-L. Tan, S.-P. Chai and S.-T. Yong, Heterostructured AgX/g-C_3N_4 (X = Cl and Br) nanocomposites via a sonication-assisted deposition-precipitation approach: Emerging role of halide ions in the synergistic photocatalytic reduction of carbon dioxide, *Appl. Catal., B*, 2016, **180**, 530–543.

209 H. Xu, J. Yan, Y. Xu, Y. Song, H. Li, J. Xia, C. Huang and H. Wan, Novel visible-light-driven AgX/graphite-like C_3N_4 (X = Br, I) hybrid materials with synergistic photocatalytic activity, *Appl. Catal., B*, 2013, **129**, 182–193.

210 Z. Yang, J. Li, F. Cheng, Z. Chen and X. Dong, BiOBr/protonated graphitic C_3N_4 heterojunctions: Intimate interfaces by electrostatic interaction and enhanced photocatalytic activity, *J. Alloys Compd.*, 2015, **634**, 215–222.

211 P. Qiu, C. Xu, N. Zhou, H. Chen and F. Jiang, Metal-free black phosphorus nanosheets-decorated graphitic carbon nitride nanosheets with C-P bonds for excellent photocatalytic nitrogen fixation, *Appl. Catal., B*, 2018, **221**, 27–35.

212 X. Tian, Y.-J. Sun, J.-Y. He, X.-J. Wang, J. Zhao, S.-Z. Qiao and F.-T. Li, Surface P atom grafting of g-C_3N_4 for improved local spatial charge separation and enhanced photocatalytic H_2 production, *J. Mater. Chem. A*, 2019, **7**, 7628–7635.

213 K. C. Christoforidis, Z. Syrgiannis, V. La Parola, T. Montini, C. Petit, E. Stathatos, R. Godin, J. R. Durrant, M. Prato and P. Fornasiero, Metal-free dual-phase full organic carbon nanotubes/g-C_3N_4 heteroarchitectures for photocatalytic hydrogen production, *Nano Energy*, 2018, **50**, 468–478.

214 W. Liu, Y. Li, F. Liu, W. Jiang, D. Zhang and J. Liang, Visible-light-driven photocatalytic degradation of diclofenac by carbon quantum dots modified porous g-C_3N_4:

Mechanisms, degradation pathway and DFT calculation, *Water Res.*, 2019, **151**, 8–19.

215 L. Lin, C. Hou, X. Zhang, Y. Wang, Y. Chen and T. He, Highly efficient visible-light driven photocatalytic reduction of CO_2 over g-C_3N_4 nanosheets/tetra(4-carboxyphenyl)porphyrin iron(III) chloride heterogeneous catalysts, *Appl. Catal., B*, 2018, **221**, 312–319.

216 Y. Li, Y. Fang, Z. Cao, N. Li, D. Chen, Q. Xu and J. Lu, Construction of g-C_3N_4/PDI@MOF heterojunctions for the highly efficient visible light-driven degradation of pharmaceutical and phenolic micropollutants, *Appl. Catal., B*, 2019, **250**, 150–162.

217 F. Chen, Q. Yang, Y. Wang, J. Zhao, D. Wang, X. Li, Z. Guo, H. Wang, Y. Deng, C. Niu and G. Zeng, Novel ternary heterojunction photococatalyst of Ag nanoparticles and g-C_3N_4 nanosheets co-modified $BiVO_4$ for wider spectrum visible-light photocatalytic degradation of refractory pollutant, *Appl. Catal., B*, 2017, **205**, 133–147.

218 L. Qu, G. Zhu, J. Ji, T. P. Yadav, Y. Chen, G. Yang, H. Xu and H. Li, Recyclable Visible Light-Driven O-g-C_3N_4/Graphene Oxide/N-Carbon Nanotube Membrane for Efficient Removal of Organic Pollutants, *ACS Appl. Mater. Interfaces*, 2018, **10**, 42427–42435.

219 S. Nayak and K. M. Parida, Dynamics of Charge-Transfer behavior in a Plasmon-Induced quasi-type-II p-n/n-n dual Heterojunctions in Ag@Ag_3PO_4/g-C_3N_4/NiFe-LDH Nanocomposites for Photocatalytic Cr(VI) reduction and Phenol oxidation, *ACS Omega*, 2018, **3**, 7324–7343.

220 S. Acharya, S. Mansingh and K. M. Parida, The enhanced photocatalytic activity of g-C_3N_4-$LaFeO_3$ for the water reduction reaction through a mediator free Z-scheme mechanism, *Inorg. Chem. Front.*, 2017, **4**, 1022–1032.

221 R. Acharya and K. Parida, A review on TiO_2/g-C_3N_4 visible-light-responsive photocatalysts for sustainable energy generation and environmental remediation, *J. Environ. Chem. Eng.*, 2020, **8**, 103896.

222 X. Ma, C. Chen, J. Hu, M. Zheng, H. Wang, S. Dong, C. Huang and X. Chen, Evidence of direct Z-scheme g-C_3N_4/WS_2 nanocomposite under interfacial coupling: First-principles study, *J. Alloys Compd.*, 2019, **788**, 1–9.

223 Y. Liang, C. Long, J. Li, H. Jin, B. Huang and Y. Dai, InSe Monolayer: Promising Cocatalyst of g-C_3N_4 for Water Splitting under Visible Light, *ACS Appl. Energy Mater.*, 2018, **1**, 5394–5401.

224 X. Ma, J. Hu, H. He, S. Dong, C. Huang and X. Chen, New Understanding on Enhanced Photocatalytic Activity of g-C_3N_4/$BiPO_4$ Heterojunctions by Effective Interfacial Coupling, *ACS Appl. Nano Mater.*, 2018, **1**, 5507–5515.

225 J. Wang, L. Tang, G. Zeng, Y. Deng, Y. Liu, L. Wang, Y. Zhou, Z. Guo, J. Wang and C. Zhang, Atomic scale g-C_3N_4/Bi_2WO_6 2D/2D heterojunction with enhanced photocatalytic degradation of ibuprofen under visible light irradiation, *Appl. Catal., B*, 2017, **209**, 285–294.

226 P. Jimenez-Calvo, C. Marchal, T. Cottineau, V. Caps and V. Keller, Influence of the gas atmosphere during the synthesis of g-C_3N_4 for enhanced photocatalytic H_2 pro-

4792 | *Inorg. Chem. Front.*, 2020, **7**, 4754–4793

This journal is © the Partner Organisations 2020

duction from water on Au/g-C$_3$N$_4$ composites, *J. Mater. Chem. A*, 2019, **7**, 14849–14863.

227 J. Wen, J. Xie, Z. Yang, R. Shen, H. Li, X. Y. Luo, X. Chen and X. Li, Fabricating the Robust g-C$_3$N$_4$ Nanosheets/Carbons/NiS Multiple Heterojunctions for Enhanced Photocatalytic H$_2$ Generation: An Insight into the

Trifunctional Roles of Nanocarbons, *ACS Sustainable Chem. Eng.*, 2017, **5**, 2224–2236.

228 J. Yuan, J. Wen, Y. Zhong, X. Li, Y. Fang, S. Zhang and W. Liu, Enhanced photocatalytic H$_2$ evolution over noble-metal-free NiS cocatalyst modified CdS nanorods/g-C$_3$N$_4$ heterojunctions, *J. Mater. Chem. A*, 2015, **3**, 18244–18255.